DIPARTIMENTO DI FISICA E ASTRONOMIA "G. GALILEI"

Corso di laurea in Astronomia

Tesi di laurea Quadriennale

POTENZA DEI JET NEI NUCLEI GALATTICI ATTIVI RADIO-BRILLANTI:
UN'INDAGINE APPLICATA ALLA NATURA DEI CANDIDATI BLAZAR

Relatore: Ch.mo Prof. Piero Rafanelli
Correlatore: Dott. Giovanni La Mura

Laureando: Umberto Baldini
Matricola: 459552

Anno Accademico 2014/2015

"È stata una lunga attesa. Lunga ed estenuante."
(Morpheus, The Matrix)

SOMMARIO

I Nuclei Galattici Attivi costituiscono una eterogenea famiglia di oggetti, alimentati da processi non riconducibili a sorgenti stellari, che popolano l'Universo sia vicino che lontano. A causa della loro elevata luminosità che, a dispetto delle dimensioni inferiori al parsec, li pone tra le sorgenti più brillanti a noi note, si ritiene che la loro energia venga prodotta dall'accrescimento di materiale catturato nel campo gravitazionale di un buco nero super-massiccio. I meccanismi che si innescano in questo processo portano alla conversione dell'energia potenziale gravitazionale della materia in energia radiante, con una efficienza pari a circa il 10% dell'energia a riposo associata alla massa coinvolta. Lo spettro della radiazione emessa copre un ampio intervallo di frequenze elettromagnetiche, estendendosi talvolta dalle lunghezze d'onda radio fino ai più energetici raggi γ. In questo lavoro si descrive lo studio delle proprietà fisiche di una popolazione di nuclei galattici attivi, selezionati sulla base della loro emissione nelle frequenze X e radio, per i quali è stato possibile reperire gli spettri ottici. L'emissione di una sostanziale frazione di energia nell'intervallo delle onde radio viene generalmente interpretata come indizio della presenza di un getto di materiale relativistico, che viene collimato da intensi campi magnetici ed accelerato fino a frazioni significative della velocità della luce. Nel caso in cui la direzione di propagazione del getto sia prossima alla linea di vista verso la sorgente, la radiazione emessa dal getto stesso domina lo spettro elettromagnetico, producendo fenomeni di varibilità, polarizzazione e luminosità radio che caratterizzano la famiglia di oggetti denominati BLAZAR. A seconda delle caratteristiche del loro spettro ottico, i BLAZAR vengono a loro volta suddivisi nelle sotto-classi di BL Lac, il cui spettro mostra prevalentemente un continuo a legge di potenza, quasi del tutto privo di righe in emissione o assorbimento, o in Flat Spectrum Radio Quasars, che al contrario mostrano evidenti righe di emissione. Entrambe queste famiglie sono state comunemente identificate come sorgenti di raggi γ ad altissima energia ($E \geq 100$MeV). Nel nostro studio andiamo

a confrontare le proprietà misurabili circa la massa, il tasso di accrescimento, la luminosità radio e la potenza del getto, in un campione di oggetti costituito da BLAZAR noti e da nuclei galattici attivi radio brillanti. Lo scopo dell'indagine è quello di determinare le proprietà dei getti di materiale relativistico rilevati in queste sorgenti al fine di valutare la possibilità che esse siano candidati blazar non ancora bene identificati Il lavoro è stato iniziato incrociando le coordinate di oggetti rilevati dalle surveys ROSAT, NVSS e FIRST, in modo da selezionare delle sorgenti X che avessero una controparte radio. In un secondo momento è stato eseguito un cross-match di questi punti con quelli di oggetti rilevati dalla survey SDSS-III in modo tale da avere a disposizione degli spettri ottici. Grazie a questi sono state stimate le principali proprietà fisiche delle sorgenti, quali le luminosità monocromatiche e bolometriche, le masse dei buchi neri contenuti in esse ed i loro tassi di accrescimento. Successivamente, sfruttando i dati di FIRST, sono stati stimati i valori del radio-loudness e della potenza dei jet. Tutti i parametri ottenuti sono stati analizzati e raffrontati con quelli dei blazar noti presenti all'interno del campione col fine di verificare se e quali fossero le relazioni tra essi, coinvolgendo infine anche il più recente catalogo della missione Fermi (3FGL). Grazie a quest'ultimo è stato possibile individuare quali tra i vari candidati ci si aspetta possa venire rilevato anche da Fermi-LAT, avendo posto un limite inferiore alla potenza del jet necessaria affinché ciò possa avvenire, prendendo quindi in esame l'emissione di radiazione ad alta energia da parte di questi oggetti e la possibilità di rilevarne il segnale grazie alla strumentazione attuale.

CONTENTS

1 Introduction **1**

1.1 AGNs' Historical Background 3

1.2 The Structure of AGNs 6

1.2.1 The Supermassive Black Hole 7

1.2.2 The Broad Line Region 9

1.2.3 The Narrow Line Region 10

1.2.4 The Corona 10

1.2.5 The Torus 12

1.3 The Unified Model 13

1.4 Modern data distribution services 15

2 Physics of jets **17**

2.1 Accretion and Magnetic Fields 18

2.1.1 Basics: Bondi Accretion and Eddington Limit 19

2.1.2 Thin Disks 20

2.1.3 Thick Disks 23

2.1.4 Advection Dominated Accretion Flow (ADAF) Models . . . 23

2.1.5 The Jet-Disk Connection 24

2.2 Synchrotron Radiation 25

2.2.1 Synchrotron Emission of a Single Particle 25

2.2.2 Synchrotron Emission of a Particle Plasma 29

2.2.3 Synchrotron Self-Absorption 30

2.2.4 Polarization 30

2.3 Inverse Compton and γ-ray Emission 31

2.3.1 Compton Effect 32

2.3.2 Inverse Compton Scattering (IC) 32

2.3.3 Synchrotron Self-Compton (SSC) . . . 34
2.4 BLAZAR model . . . 36

3 Data Selection and Analysis 39
3.1 Description of the Surveys . . . 39
3.1.1 SDSS . . . 39
3.1.2 ROSAT . . . 41
3.1.3 NVSS and FIRST . . . 42
3.1.4 Fermi . . . 44
3.2 Survey Combination Procedures . . . 46
3.2.1 The *Roma-BZCAT* catalog . . . 46
3.2.2 Other Catalogs . . . 47
3.2.3 Sky area and cross-matches . . . 48
3.3 Selection of Optical Spectra . . . 49
3.4 Reduction of Optical Spectra . . . 50
3.4.1 Image Conversion . . . 50
3.4.2 Reddening Correction . . . 52
3.4.3 Redshift Correction . . . 53
3.5 Multiple frequency data . . . 54

4 Results 57
4.1 Redshift Subdivision . . . 57
4.2 Luminosities . . . 58
4.2.1 Bolometric Luminosities . . . 60
4.3 Masses . . . 62
4.4 Accretion Rates . . . 71
4.5 Radio Loudness . . . 74
4.6 Jet Powers . . . 76
4.7 Redshift Distribution . . . 80

5 Conclusions 85

Acronyms 87

Appendix 93

References 115

LIST OF FIGURES

1.1 Average Radio-quiet AGN Spectrum 2
1.2 Basic overview of the AGN phenomenon 3
1.3 Cygnus A tricotomy 5
1.4 3C 273 7
1.5 Typical AGN spectrum 10
1.6 Dusty Torus Model 12
1.7 Unified Model scheme 14

2.1 Centaurus A 18
2.2 Thin disk spectral energy distributions 22
2.3 Dynamics of a charged particle in a uniform magnetic field 25
2.4 Relativistic beaming: electron's and laboratory rest frames 27
2.5 Synchrotron critical frequency 28
2.6 Synchrotron spectrum as sum of multiple single spectra 29
2.7 Synchrotron self-absorbtion 31
2.8 Physical processes in the Unified Scheme 35
2.9 Blazar sequence 37

3.1 Sources present in the *Roma-BZCAT* catalog 46

4.1 Linear fit of the bolometric luminosities evaluated from L_{5100},L_{3000}, and L_{1450} 61
4.2 Hβ narrow component subtraction 63
4.3 Hβ×MgII BCES bisector fitting results (normal) 67
4.4 Hβ×MgII BCES bisector fitting results (Trakhtenbrot's prescription) 68
4.5 MgII×CIV BCES bisector fitting results 69
4.6 Hβ×MgII and MgII×CIV BLR sizes comparison 71
4.7 Eddington ratios versus black hole masses 72

4.8 BCES bisector fitting results on $\log_{10} \mathrm{M}_\bullet \times \log_{10} \lambda_{\mathrm{Edd}}$ 73
4.9 λ_{Edd} and $\mathrm{M}_\bullet$ versus R, $\log_{10} L_R/L_{\mathrm{Edd}}$ versus $\log_{10} L_{4400}/L_{\mathrm{Edd}}$ 76
4.10 Distribution of the sources along the λ_{Edd}–$\log_{10} P_{\mathrm{JET}}$ and $\log_{10} L_{\mathrm{BOL}}$–$\log_{10} P_{\mathrm{JET}}$ planes 77
4.11 BCES bisector linear fitting for the $\log_{10} P_{\mathrm{JET}}$–$\log_{10} \lambda_{\mathrm{Edd}}$ relation . . 78
4.12 BCES bisector linear fits for P_{JET} against $\log_{10} \mathrm{M}_\bullet$ and $\log_{10} R$ . . . 78
4.13 $\log_{10} L_{\mathrm{BOL}}$ and λ_{Edd} versus z 80
4.14 Distribution of the SMBH masses as a function of z 81

5.1 Blazars detected by Fermi 86

LIST OF TABLES

1.1 Some of the typical emission lines observed in AGNs 3
1.2 A Simplyfied Scheme of the AGN Taxonomy 15

3.1 SEGUE and BOSS Spectrographs' characteristics 41
3.2 FIRST's bandpasses 43
3.3 SDSS-II's HDUs contents 51
3.4 SDSS-III's first two HDUs contents 51
3.5 Initial sample 55

4.1 Bolometric correction factors 60
4.2 BCES bisector values for $L_{bol,5100}$ and $L_{bol,1450}$ versus $L_{bol,3000}$ 61
4.3 Values of the FWHM measured 65
4.4 Results of the BCES bisector linear regressions done on the FWHM belonging to the Hβ×MgII group 66
4.5 MgII×CIV BCES bisector fitting results 70
4.6 Results of the BCES bisector fitting on the BLR sizes 70
4.7 Values of the BCES fitting on $\log_{10} \mathrm{M}_\bullet$ versus $\log_{10} \lambda_{\mathrm{Edd}}$ 73
4.8 Values of the BCES bisector linear fitting on $\log_{10} \lambda_{\mathrm{Edd}}$ and $\log_{10} \mathrm{M}\bullet$ versus R 75
4.9 $\log_{10} \lambda_{\mathrm{Edd}}$, $\log_{10} \mathrm{M}_\bullet$, R, and $\log_{10} L_{\mathrm{BOL}}$ versus $\log_{10} P_{\mathrm{JET}}$ BCES bisector fitting results 79
4.10 Hβ×MgII physical parameters 82
4.11 MgII physical parameters 83
4.12 MgII×CIV physical parameters 84

5.1 Identifiers of the blazar candidates 86

This research has made use of the VizieR catalogue access tool, CDS, Strasbourg, France. The original description of the VizieR service was published in Ochsenbein, Bauer & Marcaut (2000, A&AS, 143, 23).
Funding for SDSS-III has been provided by the Alfred P. Sloan Foundation, the Participating Institutions, the National Science Foundation, and the U.S. Department of Energy Office of Science. The SDSS-III web site is `http://www.sdss3.org/`.

CHAPTER 1

INTRODUCTION

The mystery of Active Galactic Nuclei (AGNs) is that they produce very high luminosities (in the range between 10^{42} and 10^{46} erg s^{-1}) in extremely compact sources ($r \sim 10^{16}$cm), probably through physical processes that likely differ from the nuclear fusion that powers stars. Thus, they are special laboratories for extreme physics and our principal probes of the Universe on large scales so that understanding them is essential to study its formation and evolution.

The first notably distinct observational characteristic of AGNs is the presence of emission lines with widths upwards of 1000 km s^{-1} and far in excess of any other known class of objects. Another distinguishing observational feature is the presence of narrow, nonvariable forbidden emission lines. These lines, when discovered, required a broad-band ionizing continuum extending far bluewards of the stellar radiation fields responsible for photoionizing the galactic nebulae where they came from.

AGNs are thought to host at their centers a massive compact object with mass $M \sim 10^6$–$10^9 M_\odot$, where $M_\odot = 1.9891 \cdot 10^{33}$g corresponds to the unit solar mass.

Another feature of an AGN's optical-UV (Ultra Violet) spectrum is that the continuum spectral distribution is very different from an integrated stellar one – characteristic of normal galaxies – with the former being very blue compared to the latter. This "anomaly", called Big Blue Bump (BBB), is a flux excess relative to an underlying powerlaw continuum, exhibiting a curvature suggesting a thermal origin (Fig.1.1).

At present the approximate structure of AGNs is known but much of their detailed physics is hidden from view because of their strongly anisotropic radiation patterns: the most broadly accepted (though still debated) picture of the physical structure of an AGN is illustrated in Fig.1.2.

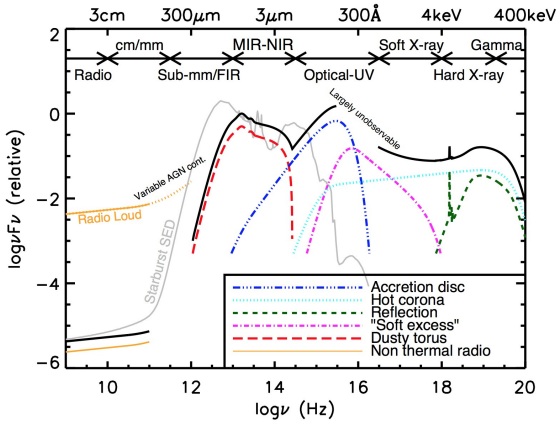

Figure 1.1: A schematic representation of an AGN's Spectral Energy Distribution (SED), loosely based on the observed SEDs of radio-quiet quasars. The black solid curve represents the total SED and the various coloured curves (with an arbitrary offset) represent the individual components. The SED of an AGN in the millimeter-FIR (Far Infrared) regime is uncertain; however, it is widely believed to have a minimal contribution (to an overall galaxy SED) compared to star formation, except in the most intrinsically luminous quasars and powerful radio-loud AGNs. The primary emission from the AGN's accretion disk peaks in the UV region. Radio-loud AGNs have radio emission that can be several orders of magnitude higher than radio-quiet ones (shown with the labelled orange line). Also shown is an example radio–UV SED of a starburst galaxy (grey curve; the SED is of M82 taken from the GRASIL library; (Silva et al., 1998).

At the center there is a Super Massive Black Hole (SMBH) whose gravitational field, attracting the nearby material, extracts its gravitation potential energy leading to the AGN powerful luminosity. The matter pulled toward the Black Hole (BH) looses angular momentum through viscous or turbulent processes in an accretion disk which glows brightly at UV and perhaps soft X-ray wavelengths. Hard X-ray emission is also produced very close to the BH, perhaps in connection with a pervasive sea of hot electrons above the disk. If the BH is spinning, energy may be extracted electromagnetically from the BH itself (Blandford and Znajek, 1977).

Strong optical and UV emission lines (Tab.1.1) are produced in clouds of gas moving rapidly in the potential of the BH, the so-called "broad-line clouds" (blue blobs in Fig.1.2a). This radiation is obscured along some lines of sight by a torus or warped disk of gas and dust well outside the accretion disk and the so called Broad Line Region (BLR).

Beyond the torus[1], slower moving clouds of gas produce emission lines with narrower widths (green blobs in Fig.1.2a) which are attributed to the effect of light crossing the Narrow Line Region (NLR).

Outflows of energetic particles occur along the poles of the disk or torus, es-

[1]For convenience, there is a tendence to refer to the obscuring matter as a torus but to date there is little to indicate whether it is actually a torus, a warped disk, or some other distribution.

Line	Relative flux*	Equivalent width (Å)
Lyα λ1216 + NV λ1240	100	75
CIV λ1549	40	35
CIII] λ1909	20	20
MgII λ2798	20	30
Hγ λ4340	4	30
Hβ λ4861	8	60

* Normalized in such a way that Lyα + NV=100

Table 1.1: Some of the typical emission lines observed in AGNs: this table is adapted from the results obtained by Peterson (1997).

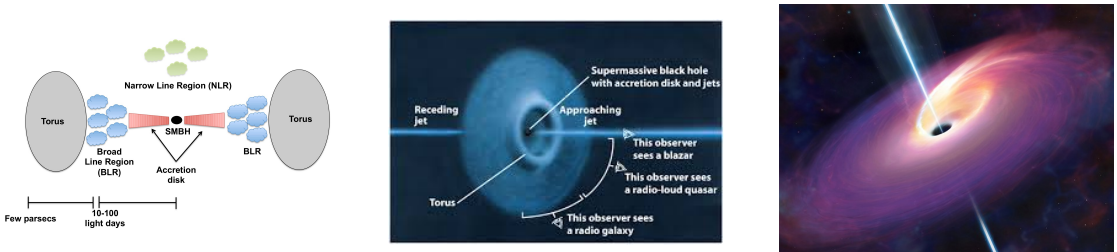

(a) (b) (c)

Figure 1.2: Basic description of an AGN's structure seen edge on (a) with insights on the jet and some of the basic properties observed in function of the inclination of the source (b). The last image (c) is an artist impression.

caping and forming collimated radio-emitting jets usually becoming powerful radio sources when the host galaxy is an elliptical (Stawarz et al., 2008).

The plasma in the jets, at least on the smallest scales, streams outward at very high velocities, being able to beam radiation relativistically in the forward direction.

This inherently axisymmetric model of AGNs implies a radically different appearance of them at different viewing angles as marginally indicated in Fig.1.2b: in practice, AGNs of different orientations are assigned to different classes as described by the Unification Scheme (Sec.1.3).

1.1 AGNs' Historical Background

The history of AGNs starts at the beginning of the last century when in 1909 Fath undertook a series of observations aimed at understanding the nature of "spiral nebulae", some of the most enigmatic sources at the time when scientists were struggling to understand whether these objects were nearby gaseous objects similar to the Orion nebula or very distant collections of unresolved stars. For

most of them Fath found continuous spectra with stellar absorption lines, which indicated emission from unresolved solar-type stars.

However, for one object, NGC 1068, he found a peculiar spectrum, showing both bright emission and absorption lines, similar to what had been observed in gaseous nebulae. This result was later confirmed by Slipher (1917) and by Hubble (1926), who found evidence of this behavior also in the spectra of NGC 4051 and NGC 4151.

The first systematic study of galaxies showing nuclear emission lines was performed by Seyfert in 1943, who studied the spectra of NGC 1068, NGC 1275, NGC 3516, NGC 4051, NGC 4151 and NGC 7469. He found that while objects like NGC 1068 had forbidden and permitted lines with roughly similar profiles and widths of ~ 400 km s^{-1}, other ones like NGC 7469 showed narrow forbidden lines and very broad (~ 8500 km s^{-1}) hydrogen (H) ones.

In the following years the study of AGNs developed mostly in the radio, an energy band that had started to be explored by astronomers thanks to the pioneeristic work of Jansky and to the technological development of radio instruments.

Jansky, working at the Bell Telephone Laboratories, conducted a study of the sources of disturbances affecting trans-Atlantic radio communications using a orientable antenna and a short-wave receiver operating at a wavelength of 14.6 m. He systematically measured the intensity of the signal arriving from all directions throughout the day, indentifying three types of disturbances, assigning them to (1) local or (2) distant thunderstorms and (3) "a type of unknown origin", the last one seeming to be somehow associated with the sun. Continuing his measurements throughout the year he observed that the source of noise moved around in azimuth every 24 hours, and the time and direction of maximum changed gradually throughout the year in a manner consistent with the earth's orbital motion around the sun. With subsequent measurements he inferred that the radiation was coming from the center of the Milky Way (MW) galaxy (Jansky, 1933). After further study of the data, Jansky concluded that the radiation came from the entire disk of the MW, being strongest in the direction of the Galactic center .

Few professional astronomers took serious note of Jansky's work, and it fell to an engineer, working at home in his spare time, to advance the subject of radio astronomy. His name was Reber and he built a 31 feet reflector in his backyard near Chicago, publishing afterwards a map of the radio sky at 160 MHz showing several local maxima, including one in the constellation Cygnus that would prove important for AGN studies (Reber, 1944). He also noted that the ratio of radio radiation to optical light was vastly larger for the MW than for the sun.

As often happens for military reasons, the technology was boosted and that's why in the early 1940's and also at the end of the World War II, several groups of

radio engineers turned their efforts to radio astronomy leading to the discovery of emission from a discrete source in Cygnus, which was then called Cygnus A (Hey et al., 1946). Afterwards it was identified by Baade and Minkowski in 1954 after some other prior studies (Bolton and Stanley, 1948).

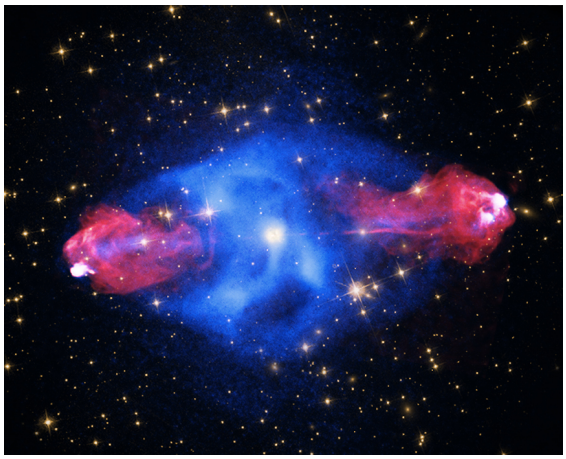

Figure 1.3: Celebrating astronomy in the International Year of Light, the detailed image reveals spectacular active galaxy Cygnus A in light across the Electromagnetic (EM) spectrum. Incorporating X-ray data (blue) from the orbiting Chandra Observatory, Cygnus A is seen to be a prodigious source of high energy X-rays. But it is actually more famous at the low energy end of the EM spectrum. One of the brightest celestial sources visible to radio telescopes, at 600 million light-years of distance Cygnus A is the closest powerful radio galaxy. Radio emission (red) extends to either side along the same axis for nearly 300 000 light-years powered by jets of relativistic particles emanating from the galaxy's central SMBH. Hot spots likely mark the ends of the jets impacting surrounding cool, dense material. Confined to yellow hues, optical wavelength data of the galaxy from Hubble and the surrounding field in the Digital Sky Survey complete a remarkable multiwavelength view.

Credit: National Aeronautics and Space Administration (NASA)/CSX/SAO (X-Ray), NASA/STScI (Optical), NSF/NRAO/AUI/VLA (Radio).

In the following years many more radio sources were discovered and their positions accurately estimated, thanks to surveys like the Third Cambridge Survey (3C) at 159 MHz (Edge et al., 1959).

The breakthrough came a few years later from observations of the very bright quasar 3C 273 thanks to radio observations performed during a lunar occultation by Hazard et al. (1963). He was able to define the position of the source with an accuracy of about 1 arcsec.

In the same year, based on optical observations, Schmidt discovered the presence of redshifted emission lines, which were almost immediately attributed as being due to Hubble expansion (Greenstein and Schmidt, 1964). The luminosity obtained and the cosmological distance excluded the possibility that these peculiar objects were very variable stars.

Few years later Sandage et al. (1965) reported the discovery of a large number of radio quiet objects that resembled quasars. These objects had been found as a characteristic population examining color to color (U-B, B-V) diagrams of stars showing a strong "ultraviolet excess" which is now well known to be one of the most important characteristics of AGNs, the BBB. Since then a large number of those objects was discovered and classified according to their main optical properties.

In the following years, thanks to the advent of space telescopes – as the pioneeristic UHURU launched in 1970 – opening the X-ray and γ-ray windows to astronomy, many sources were detected and the study of AGNs grew up in their insights leading to a better knowledge of their physical properties. Some of the most important X-ray space missions are:

- ROSAT
- XMM-Newton
- INTEGRAL
- SWIFT
- CHANDRA
- BeppoSAX

Today we know that several other galaxies harbor hints of nuclear activity, like the special cases studied by Carl Seyfert (and named *Seyfert* galaxies after him). In general, AGNs can be hosted both in spiral galaxies, where they tend to be mostly radio-quiet sources, as well as in elliptical ones, where radio-loud objects are more frequently observed (Fig.1.4). We note that their appearance changes dramatically from one case to the other, probalby depending on the orientation of the source with respect to the observer's line of sight.

The model briefly presented in Sec.1.2 and more accurately for some topics in chapter 2 is the most widely accepted one on the basis of the observations and data analysis done during the period between the discovery of the first extragalactic source and the present time.

1.2 The Structure of AGNs

AGNs are thought to be constituted by several components, all of them very likely intrinsically related to the SMBH lying at their center driving their growth and evolution.

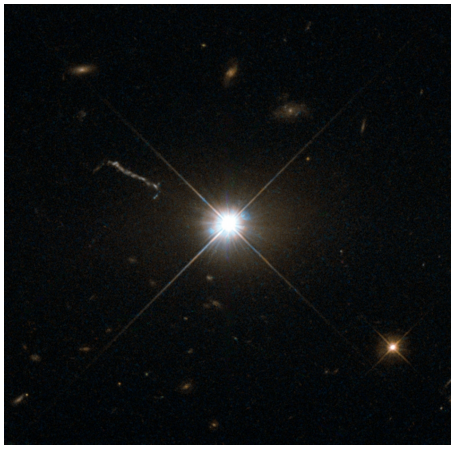

Figure 1.4: This image from Hubble's Wide Field and Planetary Camera 2 (WFPC2) is likely the best of the most well-known bright quasar 3C 273, which resides in a giant elliptical galaxy in the constellation of Virgo (The Virgin). As material from the disc falls inwards, some quasars — including 3C 273 — have been observed to fire off super-fast jets into the surrounding space. In this picture, one of these jets appears as a cloudy streak, measuring some 200 000 light-years in length.

Credit: ESA/Hubble & NASA

In the following most of the important components normally found in AGNs will be briefly described: the SMBH (1.2.1), the broad line region (1.2.2), the narrow line region (1.2.3), the corona (1.2.4) and the dusty torus (1.2.5).

1.2.1 The Supermassive Black Hole

The existence of BHs was predicted by Einstein in his formulation of General Relativity in 1916. Already a century before first Mitchell and then Laplace considered the idea of objects so dense that light cannot escape them. Although much theoretical work was done in the years following Eintstein's one, it was not until 1972 that observational support for the existence of black holes was found through observations of Cyg X-1 (Bolton, 1972; Webster and Murdin, 1972).

The presence of SMBHs ($\sim 10^6 - 10^9 M_\odot$, where $M_\odot$ corresponds to a solar unit mass) in the center of AGNs was first predicted by Lynden-Bell (1969) and later largely confirmed by several observational evidences. From the short time scales variations ($\lesssim 1$ hour) observed in AGNs it is possible to obtain an upper limit on the size of the central source, which together with mass estimates point towards very high densities, of the order of magnitude of those expected in BHs.

Rapidly rotating disks of ionized gas have been detected by Hubble Space Telescope (HST) observations (Ford et al., 1996) and the velocities measured are in agreement with a Keplerian disk rotating around a BH; moreover, the luminosities observed in AGNs can be easily explained by accretion onto a SMBH (see 2.1) and

no serious alternative explanation to this mechanism exists.

Rotating And Non-rotating Black Holes

The role of the surface for a BH of mass M is played by the sphere with a radius corresponding to the *Schwarzschild radius*:

$$\boxed{r_s = \frac{2GM}{c^2}} \tag{1.1}$$

which corresponds to the distance from the singularity at which a body cannot escape anymore from the gravitational attraction and is bound to fall inside the BH.

The metric of space-time around a non-rotating BH is given by the Schwarzschild solution (1916) to Einstein's general relativity:

$$\begin{aligned} \mathrm{d}s^2 = &\left(1 - \frac{2GM}{c^2 r}\right) c\mathrm{d}t^2 - \left(1 - \frac{2GM}{c^2 r}\right)^{-1} \mathrm{d}r^2 + \\ &- r^2 \left(\mathrm{d}\theta^2 + \sin^2\theta \mathrm{d}\phi^2\right) \end{aligned} \tag{1.2}$$

From the metric one can deduce that the last stable circular orbit around a non-rotating BH corresponds to a radial distance of $r = 3r_g$ where $r_g \equiv r_s$: it does mean that for $r < 3r_g$ no stable orbit exists, and for $r < r_g$ particles rapidly fall into the singularity.

The general solution for a rotating BH was discovered about 50 years later (Kerr, 1963) and it corresponds, for a BH with an angular momentum J, to a space-time metric described by:

$$\begin{aligned} \mathrm{d}s^2 = &\left(1 - \frac{2GMr}{\rho c^2}\right) \mathrm{d}t^2 + \\ &- \frac{1}{c^2}\left[\frac{4GMra\sin^2\theta}{\rho c}\mathrm{d}t\mathrm{d}\phi + \frac{\rho}{\Delta}\mathrm{d}r^2 + \rho\mathrm{d}\theta^2 + \right. \\ &\left. + \left(r^2 + a^2 + \frac{2GMra^2\sin^2\theta}{\rho c^2}\right)\sin^2\theta\mathrm{d}\phi^2\right] \end{aligned} \tag{1.3}$$

In this formalism $a = J/Mc$ is the angular momentum of the BH per unit mass — having the dimensions of a distance — while $\Delta = r^2 - (2GMr/c^2) + a^2$ and $\rho^2 = r^2 + a^2\cos^2\theta$. If the BH is non-rotating, $J = a = 0$, and the Kerr metric reduces to the standard Schwarzschild's one. The radius of the horizon for a rotating BH is:

$$r_+ = \frac{GM}{c^2} + \left[\left(\frac{GM}{c^2}\right)^2 - \left(\frac{J}{Mc}\right)^2\right]^{\frac{1}{2}} \tag{1.4}$$

The maximum value of the angular momentum a BH can reach is $J = GM^2/c$, and the radius of the innermost circular orbit depends on whether the particle is co-rotating or counter-rotating with respect to it. For maximally rotating BHs this value is $r \equiv r_+ = GM/c^2$ for co-rotating particles while $r \equiv 9r_+ = 9GM/c^2$ for counter-rotating ones.

The shrinking of the horizon for rotating black holes is an important result because it suggests that, in the case of a maximally rotating BH, matter can move in stable circular orbits about the BH with much smaller radii as compared with the Schwarzschild's case. Consequently, it is expected that more of the rest-mass energy of the infalling matter can be extracted as compared with the non-rotating case.

The effect of Kerr's BHs rotation is that they drag inertial frames. Before the horizon equivalent to the Schwarzschild radius is reached, the dragging of the inertial frames becomes so strong that there is a limiting radius, known as the *static limit*, within which no observer can remain at rest relative to the background stars. All observers within this limit must rotate in the same direction as the BH.

1.2.2 The Broad Line Region

The Broad Line Region (BLR) is characterized by a speedy bulk motion of clouds in the vicinity of the BH and by high gas densities ($n_e \gtrsim 10^9 \mathrm{cm}^{-3}$) in the range of $r \sim 0.05$ – 0.25 parsec (pc).

The Doppler broadening arising from the extreme velocity fields is assumed to explain the broad emission lines that dominate the so called type 1 AGN spectra. These lines are an useful probe of the central engine because the bulk motions in the BLR are regulated by gravity (due to the BH gravitational potential) and radiation pressure (caused by the emission of the accretion disk), although the influence of outflows should probably also be taken into account. The widths of AGN broad lines span over two orders of magnitude ranging from a minimum of $\Delta v_{\mathrm{FWHM}} \simeq$ 1000 km s^{-1} (not so much larger than the narrow ones) to $\Delta v_{\mathrm{FWHM}} \simeq 10^4$ km s^{-1}, with typical values of $\Delta v_{\mathrm{FWHM}} \simeq$ 5000 km s^{-1} .

The strongest lines observed in a typical AGN spectrum are the hydrogen Balmer-series ones (Hα, Hβ, Hδ), the hydrogen Lyα and those belonging to abundant ions (such as MgII, CIII] and CIV): an example is shown in Fig.1.5. The broadening of the emission lines is not due to thermal motion. In fact from their relative intensities it is possible to calculate that the gas temperature is $T \sim 10^4$K: the velocity dispersion for a gas with such a temperature would be in the order of ~ 10 km s^{-1} which is much less than the typical width observed in AGNs. If the broadening were purely thermal then from the typical widths of broad emission lines one would infer an unrealistic temperature of T $\sim 10^9$K: this is the

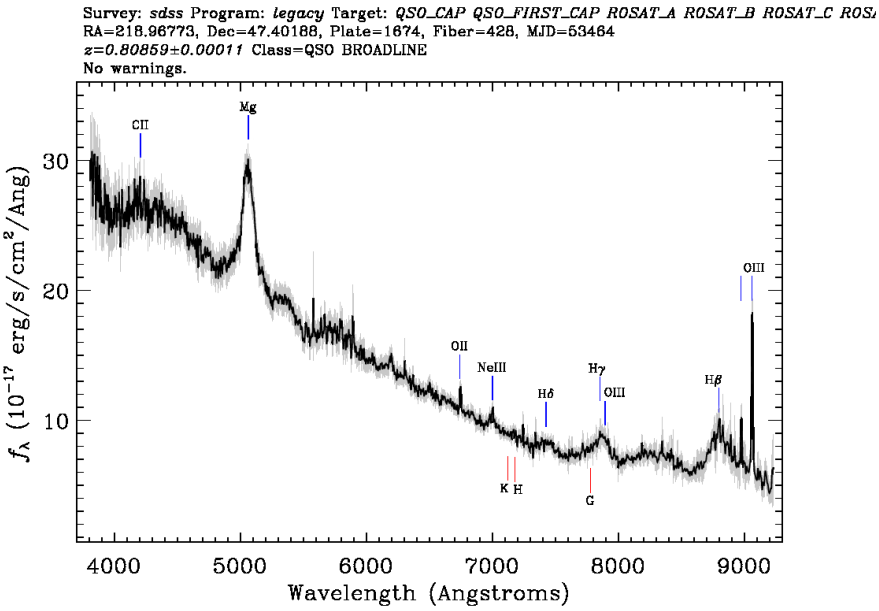

Figure 1.5: Example of a typical AGN spectrum with the broad Balmer lines of Hβ, Hγ, Hδ and Mg, together with the narrow forbidden lines of [OIII] and [OII].

Credits: SDSS (Sloan Digital Sky Survey)

reason why most of the broadening is attributed to bulk motions of individual line-emitting clouds.

1.2.3 The Narrow Line Region

The Narrow Line Region (NLR) is the largest gas structure that is under the direct influence of the AGN's ionizing radiation. Its size is large enough that it can be resolved by optical observations in nearby objects. Similarly to the BLR, the distance of the NLR to the central engine scales with luminosity ($R_{\rm NLR} \propto L^{0.5}$) and it can reach sizes up to 50 – 100 pc.

In the NLR, unlike the inner region populated by rapidly moving clouds, the electron density is low enough ($n_e \sim 10^2$ – 10^4 cm^{-3}) that many forbidden transitions are not collisionally suppressed, leading to the emission of narrow lines like Seyferts' Lyα λ1216, CIV λ1549, CIII] λ1909, [OIII] λ4959, [OIII] λ5007, [NII] λλ6548,6584 and [SII] λλ6716,6731. The Full Width Half Maximum (FWHM) for narrow emission lines lies in the range 200 km s^{-1} $\lesssim \Delta v_{\rm FWHM} \lesssim$ 900 km s^{-1} with most of them having values found in the range of 300 – 500 km s^{-1}.

1.2.4 The Corona

X-ray variability time scales indicate that the X-rays in AGNs are produced in a small region located close to the BH. The possibility that the disk should be the

only responsible for the X-ray emission can be discarded on the basis that even very warm ones are not supposed to exceed few hundreds elettronvolt (eV).

It is now widely accepted that AGNs' X-ray emission is produced by Comptonization of optical-UV photons produced in the accretion disk by a corona of hot electrons: the Inverse Compton (IC) effect upscatters photons to higher energies when their mean one ($< E >$) is smaller than the thermal energy of the electrons of temperature T_e:

$$\frac{< E >}{mc^2} < \frac{4k_{\rm B}T_e}{mc^2}$$

where $k_{\rm B} \simeq 1.381 \cdot 10^{-23}{\rm JK}^{-1}$ is the Boltzmann constant. For $h\nu \ll m_e c^2$ the gain rate of the photon is given by:

$$\frac{{\rm d}E}{{\rm d}t} = \frac{4}{3}\sigma_T c U_{RAD} \left(\frac{v}{c}\right)^2 \gamma^2 \tag{1.5}$$

where $\sigma_{\rm T} \simeq 6.652 \cdot 10^{25}{\rm cm}^2$ is the Thomson cross-section. $U_{\rm RAD}$ is the energy density of the photon field, while γ is the Lorentz factor which is equal to:

$$\gamma = \frac{1}{\sqrt{1 - \frac{v^2}{c^2}}}$$

The origin and the geometry of the hot corona is still debated and several models on the processes that upscatter the photons have been elaborated, such as:

Magnetic flares A popular explanation for the heating of the electrons in the corona is related to the presence of flares above the accretion disc, similarly to what is observed in the solar corona. Although the physical details are rather unclear, magnetic flares are a reasonably working hypothesis to model X-ray spectra and variability of AGNs. The possible evidence for hot spots corotating with the disk may support this scenario in which the magnetic flares heat the electrons, which then Comptonize the UV photons from the disk, upscattering them into the X-rays.

Clumpy disks The hypothesis that the accretion flow breaks up in two phases due to disk instabilities was originally proposed by Guilbert and Rees (1988). In this model one part of the disk is hot and optically thin, while the other is cold and optically thick. The hot phase is responsible for the primary X-ray emission, while the cold one provides the seed photons for the Comptonization and it reprocesses the primary continuum.

Aborted jets The idea that the primary X-ray emission of AGN comes from an aborted jet (stopping in the proximity of the SMBH) was introduced by Henri and Petrucci (1997) and afterwards by Ghisellini et al. (2004), who proposed

a lack of momentum to explain the jet failure: if the matter is launched – at the expense of the angular momentum of the BH – on the BH axis in form of blobs, and if their velocity is lower than the escape's one, then they could come back and collide with the other ones which were just being ejected. Kinetic energy is then converted into internal energy, providing the hot electrons necessary to Comptonize the UV photons from the disk.

1.2.5 The Torus

As shown in Fig.1.2a an obscuring torus composed of gas and dust is thought to be surrounding AGNs' central engines (Antonucci, 1993). Tori provide the material for accretion onto the SMBH and are held responsible for the orientation-dependent obscuration of the central engine. Thus, they are related to what is called the *Unification Scheme* or *Unified Model* (Sec.1.3).

This material is most likely distributed in clumps, instead of homogeneously filling the torus volume. The numerous efforts to model the torus as a homogeneous dust distribution do not explain some puzzling features of the observed dust continuum emission. The AGN-heated dust distributions turn out to be very compact with sizes on scales of about 1 pc in the mid-infrared (MIR). Only infrared (IR) interferometry currently provides the necessary angular resolution to directly study the physical properties of this dust. Size estimates for the dust distributions derived from interferometric observations can be used to construct a size-luminosity relation for the dust distributions. The large scatter about this relation suggests significant differences between the dust tori in the individual galaxies, even for nuclei of the same class of objects and with similar luminosities. This questions the simple picture of the same dusty doughnut in all AGNs.

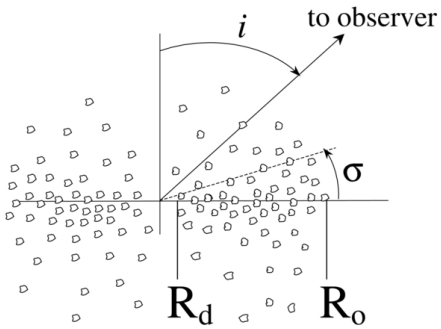

Figure 1.6: Schema of a clumpy torus model: R_d and R_o correspond to the inner and outer radii, i to the inclination in respect with the line of sight of the observer and σ is the width parameter.

In the model of Fig.1.6 the clumpy distribution has a radial extent given by $r = R_o/R_d$, the ratio of the outer to inner radii. The inner radius R_d is defined by dust sublimation temperature.

The radial density profile is a power law $\propto r^{-\alpha}$. Various angular distributions, characterized by a width parameter σ, are considered. For smooth boundaries, the parameter m determines the smoothness. For example, $m = 2$ is a Gaussian (which is proportional to $\exp[-|\beta/\sigma|^m]$) with a width σ, where the angle β is measured from the equatorial plane. The total number of clouds, on average, along any radial equatorial ray, are parametrized by N_0, and the variation of the total number of clouds along rays at angle β from the equator is $N_T(\beta) = N_0 F(\beta)$. F is a step function at $\beta = \sigma$ for a sharp-edged torus, and $\exp(-|\beta/\sigma|^m)$ for soft-edged tori.

Each clump is specified by its optical depth τ, and all clumps are assumed to have the same τ_ν, the depth at 0.55 μm. The dust extinction profile is taken as for standard Median Ratio Normalization (MRN) Galactic dust.

The clumps, of a given dust composition, are heated by an AGN with given spectral shape and luminosity L. For such a configuration, the inner radius R_d is uniquely determined by the luminosity and the chosen dust sublimation temperature:

$$R_d = 0.4(1500\text{K}/T_{sub})^{2.6}\ (L/10^{45}\text{erg s}^{-1})^{1/2}$$

The emission of directly and indirectly heated clumps at various positions around the AGN is calculated using calculations of both slabs and spherical shells modeled by radiative transfer code *DUSTY* (Nenkova et al., 2008). These two components of the source function are used to calculate the overall emission from the distribution of clumps by the separate code *CLUMPY*[2].

1.3 The Unified Model

As long as the torus exists the viewing angle on which sources are detected becomes important because it leads to the observation of different phenomena. This happens because it scatters, reflects or absorbs photons generated inside it, changing what can be inferred about the physics hidden behind. The aim of the Unified Model is to explain the different behaviours detected in the various sources as an effect of the orientation of the torus in respect to the observer's line of sight.

Fig.1.7 refers to one of the common representations of the unified model which is schematically reported in Tab.1.2. The first great dividing line is the one which separates radio-loud from radio-quiet objects. At the bottom there are the Seyfert galaxies while at the top there is the group of strongly radio-emitting ones which includes the BLAZAR family and both the Faranoff-Riley types. While Seyferts – briefly described in Sec.1.1 earlier – are weak radio emitters, Narrow Line Radio Galaxys (NLRGs) and Broad Line Radio Galaxys (BLRGs) strongly emit in the

[2] `https://www.clumpy.org/~clumpyweb/html/clumpygroup.html`

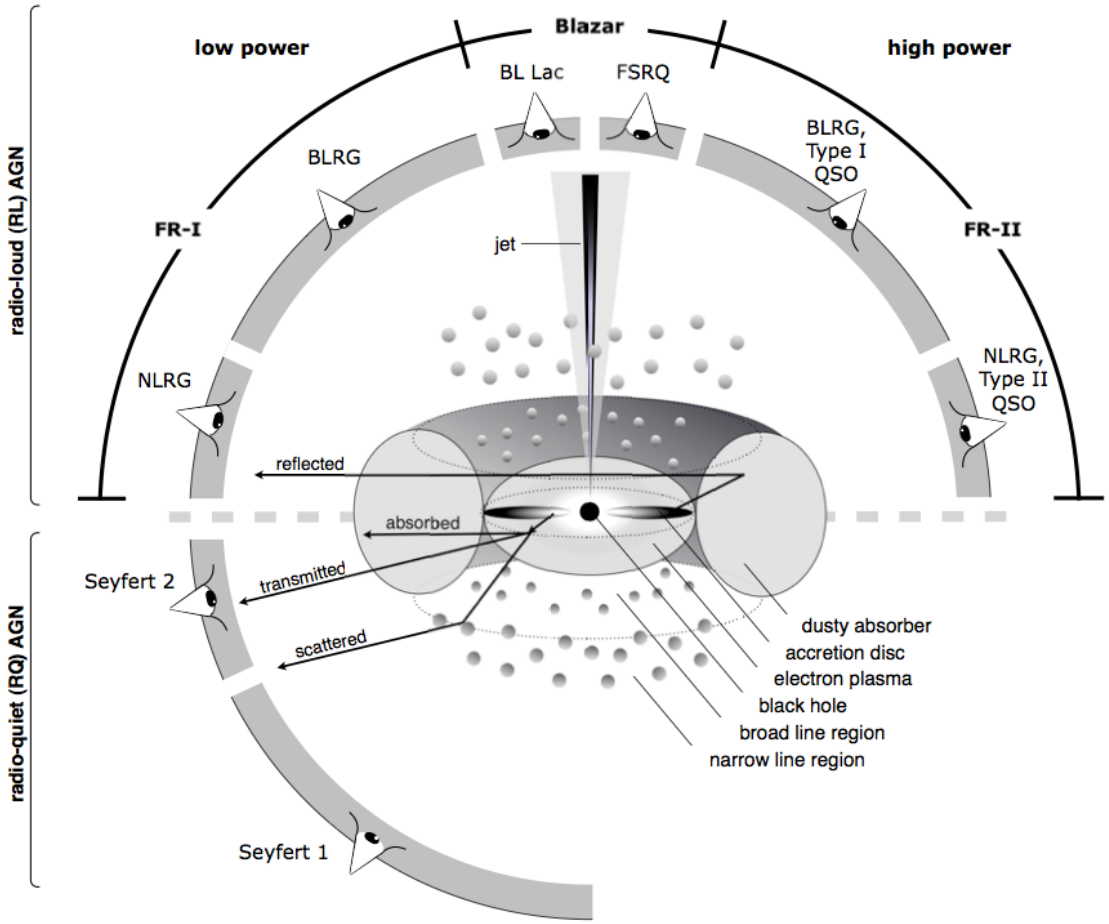

Figure 1.7: As can be seen in this basilar schema AGNs are divided on the viewing angle on which they are observed and on the radio-loudness of the source. For radio-loud objets, which are in the upper part, there is another subdivision in classes FR-I and FR-II, whose dividing line is populated by the BLAZAR's family composed by BL Lacs and Flat Spectrum Radio Quasars (FSRQs).

Credit: "Active Galactic Nuclei", Beckmann and Shrader (2012)

radio band. The Faranoff-Riley family, whose distinction was originally based on the morphology of the large-scale radio emission, has two classes: FR-I sources are brighter towards the centre, while FR-IIs at the edges. BLAZARS, which are often γ-ray emitters, are the class of AGNs thought to be viewed face-on: they emit strongly in the radio band ($L_{\mathrm{R}} = 10^{44}$–10^{48} erg s^{-1}) with relativistic jets oriented close to the line of sight with the observer. The special jet orientation explains their general peculiar characteristics: high observed luminosity, very rapid variability, high polarization (when compared with non-blazar quasars), and the apparent superluminal motions detected along the first few parsecs of the jets in most blazars (Sec.2.4).

Radio-Loudness	**Optical Emission Line Properties**		
	Type 2 (Narrow Line)	**Type 1** (Broad Line)	**Type 0** (Unusual)
Radio-quiet	Seyfert 2	Seyfert 1 QSO	
Radio-loud	NLRG { FR-I FR-II	BLRG SSRQ FSRQ	BLAZARS { BL Lacs (FSRQ)
	decreasing angle to line of sight $\longrightarrow$		

Table 1.2: AGN classification based on both the radio-loudness and the optical properties of the sources. Notice that NLRG and BLRG stand for Narrow Line Radio Galaxy and Broad Line Radio Galaxy, both belonging to the radio-loud group.

1.4 Modern data distribution services

Our understanding of AGNs experienced a major improvement thanks to the increasing availability of data observed at various frequencies.

Astronomical archives are essential components of all astronomical observatories: their holdings are in most cases unique, and they allow the re-use of the data for many different scientific purposes. They are excellent tools for the study of variable phenomena and provide reference information for the planning and calibration of new missions.

The first database to be made accessible on-line was the International Ultraviolet Explorer (IUE), back in 1985, when the World Wide Web (WWW) did not even exist, storing an amount of $\sim$ 23Gb of data nowadays hosted at the Space Telescope Science Institute (STSCI). As long as the WWW has grown up many webservices were developed. They let end users have access to lots of astronomical data such as spectra or catalogs. The network expansion made researchers able to find images of interest and to reduce them by themselves. In the same period, computing power and avaiable space for storage have grown up exponentially leading to the possibility of real time data transactions between servers and clients.

This behaviour let the scientific community to develop a world wide network in which researchers (and not only) are able to access resources from their Personal Computers (PCs) and upload their research results to databases which in most all cases are consultable by everyone owning a PC and an active internet connection. Web sites owning a database of data collected by surveys or prepared catalogs

often offer to users the opportunity to ask for them using Grafical User Interfaces (GUIs).

A more powerful way which lets researchers to be able to interface themselves with databases in order to let them query for data is the SQL language, which permits access to the information stored on servers through a Command Line Interface (CLI). Implementing good SQL queries leads to effectively discard all the information that has no specific interest for a particular research.

The Virtual Observatory (VO) offers a collection of many different services, designed to run on PCs over the web. An example of the powerful VO capabilities is the possibility – using only a web browser – to query through the SQL language for data in order to plot the result, editing and saving the graph on the local machine afterwards.

CHAPTER 2

PHYSICS OF JETS

Jets have been associated with accretion disks, both theoretically and observationally.

Relativistic jets are highly collimated plasma outflows present in extragalactic radio sources, associated with AGNs. The radio emission from the jets is synchrotron radiation produced by relativistic electrons and positrons gyrating around magnetic field lines. The particles interact with their own synchrotron photons by IC process, which leads to a boosting of the self-generated synchrotron photons to higher energies like X-rays and γ-rays. Therefore, jets can be observed over a wide range of the EM spectrum. Moreover, the observed radio emission from the jets proves the presence of magnetic fields and particles accelerated to the relativistic regime. Most AGNs produce weak or undetectable jets while it is only a minority – specifically radio galaxies and quasars – that are associated with powerful ones.

AGNs' jets are best resolved at radio wavelengths using Very Long Baseline Interferometry (VLBI). One of the most impressive examples is the observation of NGC 1275 (Venturi et al., 1993): the large scale linear outflow has been probed on scales $\lesssim 0.1$ pc and exhibits a complex structure perpendicular to the jet axis.

There is a significant type of connection between jets and disks, where the former are generically responsible for extracting both angular momentum and energy released by gas as it flows radially inward through the latter. Magnetic fields provide a plausible link between disks and jets playing a large role in their collimation. In powerful AGNs jets and Young Stellar Objects (YSOs) outflows, neither gas pressure nor radiation pressure appears to be adequate to the task of collimating large momentum flux, leaving magnetic field as the prime candidate. The question that immediately arises is what does confine the magnetic field.

The magnetic fields that are being invoked to account for jet collimation may be

Figure 2.1: A Chandra image of the nearby galaxy Centaurus A provides one of the best views of the effects of a SMBH. Opposing jets of High Energy (HE) particles can be seen extending to the outer reaches of the galaxy. HE electrons spiraling around magnetic field lines produce the X-ray emission from the jet and counterjet which quickly saps the energy from the electrons, so they must be continually reaccelerated or the X-rays will fade out. Knot-like features in the jets show where the acceleration of particles to HE is currently occurring. In this image, low-energy X-rays are colored red, intermediate-energy X-rays are green, and the highest-energy X-rays are blue. The dark green and blue bands running almost perpendicular to the jet are dust lanes that absorb X-rays.

Credit: NASA/CXC/CfA/R.Kraft et al

anchored to the accreting gas orbiting the central compact object. Poloidal magnetic flux may be dragged radially inward by the accreting gas until its dissipative escape, driven by the gradient in magnetic pressure, limits its growth (Blandford, 1989). Provided that the magnetic field makes an angle of less than 60° with the radius vector at the disk – assumed to be in Keplerian motion – it will be energetically favorable for gas to leave the disk in a centrifugally driven wind.

Presumably, the detailed magnetic field geometry at the disk can adjust so that the flow is self-limiting. The rotation of the disk will also create a toroidal magnetic field so that the stress acting on its surface can exert a torque and extract angular momentum. Detailed models have been developed to exhibit this picture and to show that it can be internally consistent and related more usefully to the observations.

2.1 Accretion and Magnetic Fields

Dynamical arguments suggest that matter orbiting a central massive object will settle into a flattened structure – for example as the rings of Saturn – which will be referred to as a disk or, if the matter spirals inwards onto the massive object, an *accretion disk*.

In the case of protostellar objects, there is accumulating evidence that YSOs are surrounded by disks with masses $\sim$ 0.01 – 1 $M_\odot$ on scales of $\sim$ 10^2 – 10^3

Astronomical Units (AUs). In the case of AGN the central object is the SMBH with its gravitational field drawing the material inwards, leading to viscous heating and thus in principle to an observable signature in the emitted radiation.

In the 90's the general notion of an accretion disk in an AGN was called into question (Holt et al., 1992). The most direct evidence came from the identification of Seyfert 2 galaxies with obscured Seyfert 1 galaxies (Lawrence and Elvis, 1982) and the interpretation of X-ray spectra with reflection by a planar surface (George and Fabian, 1991).

Early models of disk accretion faced the basic problem that the orbiting material must, through some unknown microphysics, loose angular momentum.

The total angular momentum of the system must be conserved, thus, the angular momentum lost due to matter falling onto the center has to be offset by an angular momentum gain of matter far from the center. This process is referred to as angular momentum *transport*.

2.1.1 Basics: Bondi Accretion and Eddington Limit

As pointed out previously, the basic mechanism underlying AGNs' central engines is accretion: matter falls onto the BH leading to the conversion of gravitational potential energy to EM radiation.

The simplest configuration one might consider is an approximately spherically symmetric accretion flow onto the BH accreting matter at an approximate rate of $\dot{M} = \pi r^2 \rho v$ where ρ and v are, respectively, the wind density and velocity. This type of "spherical accretion" is often referred to as Bondi accretion (also called Bondi–Hoyle accretion), as the first detailed calculations were worked out by the physicist Herman Bondi in the early 1950s (Bondi, 1952).

The effective capture radius for accretion can be roughly estimated by equating the escape velocity for a particle at distance R to the wind velocity:

$$V = \sqrt{\frac{2GM_\bullet}{R}}$$

which becomes

$$R = \frac{2GM_\bullet}{V^2}$$

The accretion rate is then:

$$\dot{M} = \frac{4\pi\rho G^2 M_\bullet^2}{V^3} \tag{2.1}$$

This is an approximate relation for Bondi's more detailed formulation, but it is sufficient to provide physical insight.

Ultimately, accretion onto a compact object is limited by the effects of the radiation pressure experienced by the in-falling plasma. This limit, first pointed out

by Arthur Eddington in the 1920s, depends on the mass of the compact object and the mean opacity of the in-falling material. Often in astrophysical environments it suffices to use the opacity of ionized H. The observable quantity corresponding to the critical mass-accretion rate for a source at a known distance is its luminosity, commonly referred to as the *Eddington luminosity*. This quantity is obtained by equating the pressure gradient of the in-falling matter

$$\frac{\mathrm{d}P}{\mathrm{d}r} = \frac{-GM\rho}{r^2}$$

to the radiation pressure

$$\frac{\mathrm{d}P}{\mathrm{d}r} = \frac{-\sigma_{\mathrm{T}}\rho}{m_p c}\frac{L}{4\pi r^2}$$

where M is the central object mass, $\sigma_{\mathrm{T}} \simeq 6.65 \cdot 10^{-25}$ cm^2 is the electron Thomson cross-section and m_p is the proton mass (assuming that the in-falling plasma is predominantly ionized H). This leads to the following equation:

$$\boxed{L_{\mathrm{Edd}} = \frac{4\pi G M m_p c}{\sigma_{\mathrm{T}}} \simeq 1.26 \cdot 10^{38}\frac{M}{M_\odot} \ \left[\mathrm{erg\ s^{-1}}\right]} \tag{2.2}$$

The Eddington ratio or Eddington rate λ is defined in terms of the bolometric (Sec.4.2.1) and Eddington's luminosities:

$$\boxed{\lambda = \frac{L_{\mathrm{BOL}}}{L_{\mathrm{Edd}}}} \tag{2.3}$$

The Eddington limit is reached when $\lambda = 1$ after which the radiation pressure drives outflows.

The Bondi accretion process is unlikely to be significant in powering AGNs. The main reason for this is that the efficiency with which gravitational potential energy can be converted into emergent radiative energy is low. Radiation in an accretion flow is thermal in nature and is produced by the viscous heating of the plasma. The basic problem is that in the absence of angular momentum, that is, for pure Bondi accretion, the plasma falls onto the central compact object before it has time to radiate the bulk of its thermal energy. If the plasma is collapsed into a disk-shaped structure, as is expected to occur from basic dynamical arguments as long as it has some angular momentum, it can radiate far more efficiently and the Bondi prescription has to be developed.

2.1.2 Thin Disks

The thin-accretion disk model assumes that the disk is quasi-Keplerian and that it extends to the innermost stable circular orbit. The disk is driven by inter-

nal viscous torque, which transports the angular momentum of the disk outwards, allowing the disk matter to be accreted onto the BH. It is assumed that the torque vanishes at the innermost stable orbit, so that the disk matter plunges into the BH carrying the specific energy and angular momentum that it had before leaving it. In the general relativistic regime, accretion onto the BH implies the conversion of the rest mass-energy of the infalling matter in the BH potential well into kinetic and thermal energy of the accreting mass flow. If the thermal energy is efficiently radiated away, the orbiting gas becomes much cooler than the local virial temperature, and the disk remains geometrically thin.

A remarkably useful approximate solution to the problem, applicable to geometrically thin but optically thick accretion disks within a constant rate of accretion, was proposed in the early 1970s (Shakura and Sunyaev, 1973). The resulting class of models, in the literature, are often referred to as "α-disk" models. A basic assumption in the α-disk scenarios is that the energy from accreted material is dissipated within a small region at its radius r. Furthermore, since the disk medium is optically thick, the emergent spectrum is that of a Black Body (BB) with a temperature $T = T(r)$.

Starting with the simplistic assumption of a region of the disk releasing gravitational energy at a rate $GM\dot{M}/r$, it is possible to apply the Virial Theorem (VT) to relate this energy to the local temperature, where one half of it should go into the kinetic (thermal) energy of the gas. For a local equilibrium to be maintained the other half must be radiated away, thus

$$L = \frac{GM\dot{M}}{2r} = 2\pi r^2 \sigma T^4$$

where σT^4 is the BB radiation formula for the energy per unit area, $2\pi r^2$ is the disk (ring) area and $\sigma \simeq 5.67 \cdot 10^{-8} \mathrm{Wm}^{-2}\mathrm{K}^{-4}$ corresponds to the Stefan-Boltzmann constant. This leads to a temperature $T(M, \dot{M}, r)$ satisfying

$$T \propto (M\dot{M})^{\frac{1}{4}} r^{-\frac{3}{4}}$$

As previously mentioned, the early models of disk accretion faced a basic problem: the orbiting material must, through some process, lose angular momentum. The total angular momentum of the system must be conserved, thus, the quantity lost due to matter falling onto the center has to be offset by an angular momentum gain of matter far from the center (thus angular momentum "transport" must occur). Shakura and Sunyaev (1973) proposed turbulence in the gaseous material of the disk as the source of increased viscosity enabling this process. Assuming subsonic turbulence and the disk height as an upper limit for the linear scale of the putative turbulent structures, the disk viscosity ν can be approximated as

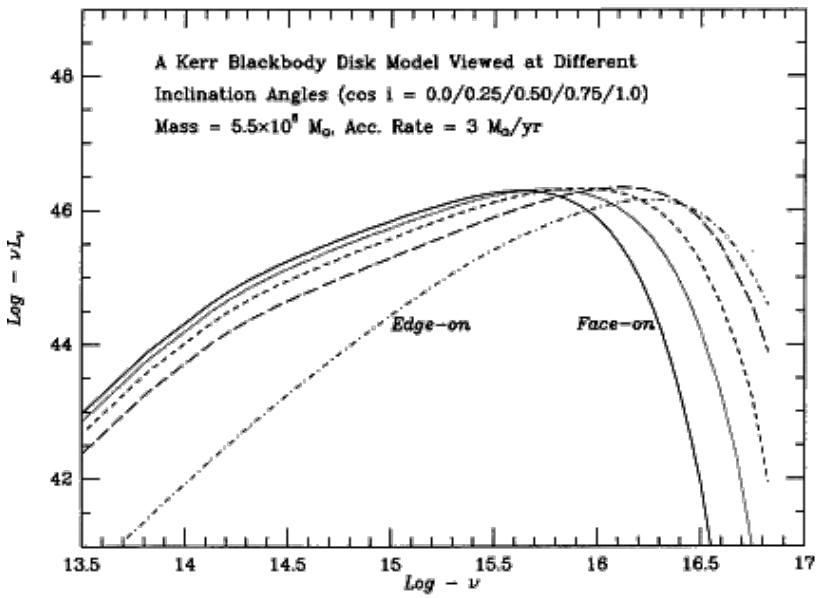

Figure 2.2: These calculations from Sun and Malkan (1989) illustrate possible optical-UV spectral energy distributions assuming that the BBB component is due to an α-disk. Effects of viewing angle are indicated, and in this case, a Kerr BH (1.2.1) with a dimensionless momentum-to-mass ratio of $a/M = 0.998$ is assumed.

$\nu = \alpha c_s h$, where c_s is the speed of sound within the medium and h is the scale height of the disk. In this simplified prescription the parameter α is a dimensionless quantity between 0 and 1, corresponding respectively to the zero and maximum accretion rates. The introduction of this free parameter allows for the disk structure to be calculated by using the equation of hydrostatic equilibrium, combined with conservation of angular momentum with the assumption that the disk is thin.

The emergent spectrum can be calculated as well. Each annular segment of the disk has a temperature and emits as a BB with a luminosity $2\pi r \mathrm{d}r \sigma T^4$, with a spectral energy distribution described by the Planck function,

$$B(\nu, T) = \frac{2h\nu^3}{c^2} \frac{1}{e^{\frac{h\nu}{k_\mathrm{B}T}} - 1} \tag{2.4}$$

The flux at a given frequency is then given by the integral:

$$S_\nu \propto \int_{R_\mathrm{in}}^{R_\mathrm{out}} B(\nu, T)\, 2\pi r \,\mathrm{d}r \tag{2.5}$$

For typical AGN physical parameters, for example for a few times $10^8 \mathrm{M}_\odot$ BH accreting at about 10% of its Eddington rate, the peak temperature of the disk should correspond to photon energies of ~ 50 eV, which is in the extreme UV (or very soft X-ray) portion of the spectrum at zero redshift.

2.1.3 Thick Disks

In AGN accretion disks there may be parameter-space regimes where the thin-disk scenarios break down. If for example, the accretion rate significantly exceeds the Eddington value, or the cooling of the disk becomes highly inefficient (corresponding to high values of the viscosity parameter α), the flow cannot be vertically confined and the standard α-disk model is not sustainable. Toroidal or "thick-disk" geometries may then be required to model the accretion flow, depending on whether the pressure is dominated by radiation or by hot gas.

The emergent radiation from a thick-disk photosphere has a characteristic BB spectrum with a peak temperature and frequency that scales with $M^{1/4}\dot{M}^{1/4}$ in a manner similar to geometrically thin disks, reaching maxima at radii of about $R \simeq 5r_s$.

2.1.4 Advection Dominated Accretion Flow (ADAF) Models

Another issue is that AGNs are broadly separated into the radio-loud and radio-quiet categories (Sec.1.3), with the former exhibiting collimated jets. Other astrophysical objects believed to be driven by disk accretion, like galactic X-ray binaries, are characterized by distinct observational spectral states and intermittent jet activity.

All of this suggests that accretion disks undergo transitions from one type of configuration – for example one reasonably well-approximated by the α-disk prescription – to another which is radiatively inefficient and perhaps favorable to outflows. The Advection Dominated Accretion Flow (ADAF) scenarios (e.g., Narayan and Yi, 1995) may address this in a natural manner.

Basically, accreting gas is heated viscously and cooled radiatively. Any heat excess is stored in the gas and then transported in the flow. This process represents an "advection" mechanism for the transport of thermal energy. The conditions for an ADAF to form are a low (sub-Eddington) accretion rate and a gas opacity which is very low. An element of the gas is unable to radiate its thermal energy in less time than it takes it to be transported through the disk onto the BH. The observed radiation is a combination of emission from the ADAF and the jet, with the radiation from thermal electrons likely to be from the ADAF rather than from nonthermal electrons that comprise the jet. The thin disk to ADAF boundary apparently occurs at luminosities $L \sim 0.01$–$0.1L_{Edd}$.

2.1.5 The Jet-Disk Connection

Models of jet formation from an accretion disk invoke magnetic field structures, as the synchrotron radio emission observed in jets is possible only with their presence. A possible condition for centrifugal launching of jets from a thin accretion disk is that the coronal particles, which are found just above the disk, should go into unstable orbits around the BH (Lyutikov, 2009).

It is now widely accepted that the main ingredients in the formation and collimation of astrophysical jets are accretion disks and magnetic fields: a poloidal field anchored in the rotating disk centrifugally accelerates the jet gas; toroidal field components, generated by the winding up of the poloidal field lines, are responsible for the collimation of the flow.

Energy and angular momentum of a BH can be electromagnetically extracted in the presence of a strong magnetic field threading the BH and supported by external currents flowing in the accretion disk as shown by Blandford and Znajek (1977). In this case, the energy flux of the jets is provided by conversion of the BH rotational energy. Summarizing the results of their work:

$$P_{\mathrm{BZ}} \simeq \frac{1}{128} B_0^2 r_g^2 a^2 c \tag{2.6}$$

where r_g is the gravitational radius and $a = J/J_{\max}$ is the adimensional angular momentum of the BH ranging from $a = 1$ for maximally rotating BHs to $a = 0$ for non-rotating ones (as in the Schwarzschild's case). In this formalism BHs' spins play an important role, the higher values leading to higher accretion rates and jet powers.

Another way of powering the jets comes from Magnetohydrodynamic (MHD) winds arising from the inner regions of accretion disks (Blandford and Payne, 1982). In this scenario jets would be powered solely from the accretion process through the action of the magnetic field.

The current understanding of jet formation is that outflows are launched by MHD processes in the close vicinity of the central object. It is clear that accretion and ejection are related to each other: jets may be a consequence of accretion, but accretion may, in turn, be a consequence of a jet.

ADAF models do not automatically lead to jet emission. Typical MHD simulations do not produce large scale magnetic fields but small scale turbulent magnetic ones: this means that they are good for angular momentum transfer but not for relativistic jet launching. One idea for producing them is the magnetic field line dragging.

2.2 Synchrotron Radiation

Magnetic fields are present everywhere in astrophysical environments, strongly influencing with their presence charged particles' moving paths, leading to EM emission.

The synchrotron radiation of ultra-relativistic electrons dominates much of high energy astrophysics. This radiation is the emission of high energy electrons gyrating in a magnetic field. This process is responsible for the radio emission of our Galaxy, of supernova remnants and extragalactic radio sources.

Other evidence for the importance of magnetic fields comes from our Galactic center, where many long "threads" and "filaments" have been mapped (Yusef-Zadeh and Morris, 1988). Morphologically most of these resemble magnetic flux tubes that have been activated, somewhat similar to the Hα and X-ray images of solar prominences. However, these features appear unusually straight and smooth which indicates that the region in which they are found is magnetically dominated.

2.2.1 Synchrotron Emission of a Single Particle

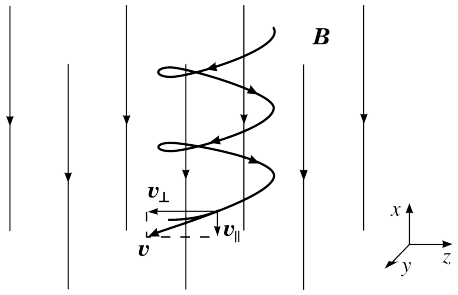

Figure 2.3: Dynamics of a charged particle in an uniform magnetic field.

As shown in Fig.2.3 the electron changes direction because the magnetic filed exerts a force perpendicular to its original direction of motion. The energy of the emitted photons is a function of the electron energy, of the magnetic field strength $\vec{B}$, and of the angle between the electron's path and the magnetic field lines. The more general assumption is that of a particle with charge $q = Ze$, rest mass m and Lorentz factor

$$\gamma \equiv \frac{1}{\sqrt{1 - \frac{v^2}{c^2}}} \tag{2.7}$$

travelling through a magnetic field which is uniform and static. This will lead to a force

$$\frac{\mathrm{d}}{\mathrm{d}t}\left(\gamma m \vec{v}\right) = \frac{Ze}{c}\left(\vec{v} \times \vec{B}\right) \tag{2.8}$$

The acceleration is perpendicular to the direction in which the charged particle travels, thus its velocity v and Lorentz factor γ are constant. In addition, the force

is perpendicular to the direction of the magnetic field, and thus also the velocity of the particle in direction of the B field $v_\parallel$ will be constant. Thus, as the total velocity v, and $v_\parallel$ are constant, the velocity perpendicular to the magnetic field will also be constant: $v_\perp = \sqrt{v^2 - v_\parallel^2}$. Therefore, the particle will travel with constant velocity in the direction of the magnetic field and will perform a circular motion with constant radius r_g and constant pitch angle β with respect to the magnetic field. The radius r_g is called *gyroradius*:

$$r_g = \frac{\gamma m c v_\perp}{ZeB} \tag{2.9}$$

This also gives the frequency of the circular motion, the so-called *gyrofrequency* or Larmor frequency:

$$\nu_g = \frac{ZeB}{2\pi\gamma mc} \tag{2.10}$$

The angular gyrofrequency is then $\omega_g = 2\pi\nu_g$.

The total luminosity (power) of the acceleration process is (Rybicki and Lightman, 1986):

$$L = \frac{2Z^2e^2}{3c^3}\gamma^4 \left[\left(\frac{\mathrm{d}\vec{v}_\perp}{\mathrm{d}t} \right)^2 + \gamma^2 \left(\frac{\mathrm{d}\vec{v}_\parallel}{\mathrm{d}t} \right)^2 \right] \tag{2.11}$$

The acceleration is perpendicular to the velocity, thus $\mathrm{d}v_\parallel/\mathrm{d}t = 0$. Because the charged particle follows a circular motion, the perpendicular acceleration is $\mathrm{d}v_\perp/\mathrm{d}t = \omega_g v_\perp$. The perpendicular velocity can be expressed as a function of the costant particle velocity v and the pitch angle β between the direction of the particle and the magnetic field: $v_\perp = v \sin\beta$. Rearranging:

$$L = \frac{2Z^4e^4B^2\gamma^2}{3c^5m^2} v_\perp^2 = \frac{2Z^4e^4B^2\gamma^2 v^2 \sin^2\beta}{3c^5m^2} \tag{2.12}$$

Assuming an isotropic distribution of particle velocities it is possible to average the power over all possible pitch angles β resulting in different values for the perpendicular velocity:

$$\langle v_\perp^2 \rangle = \frac{v^2}{4\pi} \int \sin^2\beta \mathrm{d}\Omega = \frac{2v^2}{3}$$

Keeping in mind that the second term in the square brackets (Eq. 2.11) has value zero and rearranging the first one, the synchrotron luminosity finally becomes

$$L = \frac{4Z^4e^4B^2\gamma^2v^2}{9c^5m^2} = -\frac{\mathrm{d}E}{\mathrm{d}t} = \frac{4Z^4e^4B^2E^2}{9m^4c^7} \tag{2.13}$$

having multiplied for m^2 in order to obtain the energy of the particle E through $(\gamma mv)^2 = (E/c)^2$.

Because $L \propto m^{-2}$ this is most efficient for light particles like electrons or

positrons. Recalling that the proton-to-electron mass ratio is $m_p/m_e \simeq 1836$ the radiative power of a proton travelling at speed v in the magnetic filed will be lower of a factor $\sim 10^{-7}$ compared to an electron under the same conditions. It means that for a given synchrotron luminosity a proton jet would have to be significantly faster than an electron or positron one.

For light particles like electrons or positrons, Eq.2.13 can be rearranged substituting for the Thomson cross section $\sigma_{\rm T}$ and the magnetic energy density, which is equal to $U = B^2/8\pi$:

$$L_{\rm e^-} = \frac{4}{3}\sigma_{\rm T}\frac{v^2}{c}\gamma^2 U_B \tag{2.14a}$$

$$L_{\rm e^-,rel} = \frac{4}{3}\sigma_{\rm T} c\gamma^2 U_B \tag{2.14b}$$

where the second equation refers to a highly relativistic electron for which $v/c \simeq 1$. Thus, the synchrotron luminosity becomes a function only of the Lorentz factor (Eq.2.7) and the energy density in the magnetic field.

Relativistic Beaming

One of the general features of the radiation of relativistic electrons is that the radiation is beamed in their direction of motion. This is primarily associated with the effects of relativistic aberration between the instantaneous rest frame of the electron and the observer's frame of reference as shown in Fig.2.4. In this case the

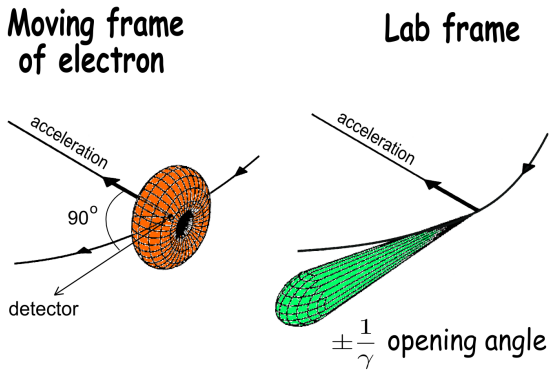

Figure 2.4: In this graphical schema the highly relativistic accelerating particle emits dipole radiation in its own rest frame while in the laboratory's one the radiation will be concentrated in a cone.

radiation will not be emitted isotropically, but because of beaming effects it will be concentrated in a narrow cone symmetric about the particle's velocity vector, having opening angle $\Phi \simeq \gamma^{-1}$.

The observer will receive a pulsed emission with the widths of pulses being

much smaller than the gyration period ω_g. The observed frequency is:

$$\nu \sim \Delta t^{-1} \sim \gamma^2 \nu_g = \gamma^3 \nu_r = \frac{\gamma^3 v}{2\pi r_0} \tag{2.15}$$

where ν_r being the non-relativistic gyrofrequency and r_0 the radius of curvature of the particle's orbit (gyroradius) in the non-relativistic case.

The spectrum emitted by a single particle averaged over the orbit has a maximum at $\nu = 0.29\nu_c$, where ν_c is the *critical frequency*:

$$\nu_c = \frac{3}{2}\gamma^3 \nu_g \sin\beta \tag{2.16}$$

Noticing that $\nu_g \propto \gamma^{-1}$ (Eq.2.10) the maximum synchrotron frequency is proportional to:

$$\boxed{\nu_c \propto E^2 \propto \gamma^2}$$

The power per unit frequency of the synchrotron emission (Fig.2.5) has the form (Ginzburg, 1989):

$$L(E,\nu) = \frac{\sqrt{3} Z^3 e^3 B \sin\beta}{mc^2} F(x) \tag{2.17}$$

with $x = \nu/\nu_c$ and

$$F(x) = \nu/\nu_c \int_{\nu/\nu_c}^{\infty} K_{5/3}(\zeta)\, \mathrm{d}\zeta \tag{2.18}$$

where $K_{5/3}$ is the modified Bessel function of order $5/3$.

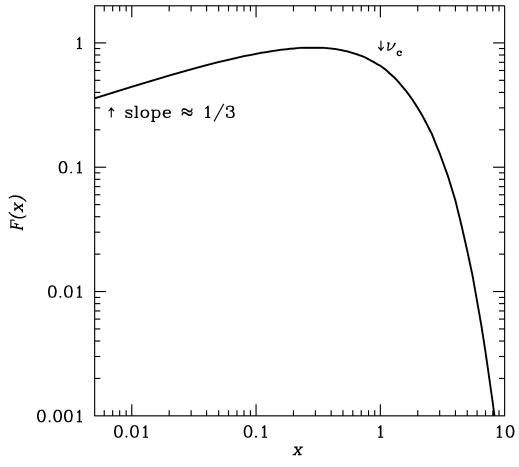

Figure 2.5: This plot illustrates the synchrotron radiation emitted by a single particle where $x = \nu/\nu_c$ and $F(x)$ are referred to Eq.2.18.

2.2.2 Synchrotron Emission of a Particle Plasma

In astrophysical sources the emissions observed usually come from large numbers of charged particles. Under the assumption that no emission will be absorbed before leaving the plasma – which is unrealistic, as discussed in Sec.2.2.3 – it is possbile to sum up every single particle's contribution as shown in Fig. 2.6.

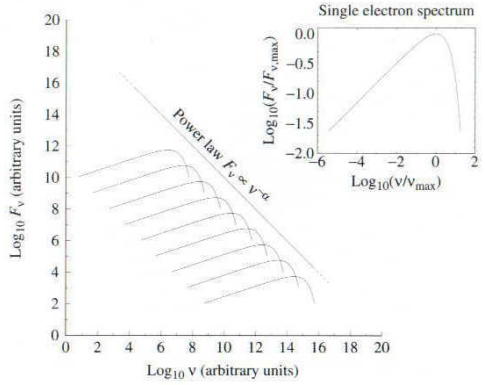

Figure 2.6: In ideal conditions, where there is no absorption along the path from the source of radiation to the observer, synchrotron spectra from single particles can be added forming perfectly a single powerlaw spectrum.

Considering an ensemble of electrons, one can thus proceed with the approximation that the single particle emits all its synchrotron power at the critical frequency:

$$\nu \simeq \nu_c \simeq \gamma^2 \nu_g = \left(\frac{E}{mc^2}\right)^2 \nu_g$$

The energy distribution of the synchrotron emission will depend directly on the energy distribution of the electrons. Assuming that they have energies in the interval $E_1 - E_2$, the total synchrotron emissivity will be:

$$\epsilon(\nu) = \int_{E_1}^{E_2} L(E,\nu)\, n(E)\, \mathrm{d}E$$

where $L(E,\nu)$ corresponds to the expression of Eq.2.17 and $n(E)\mathrm{d}E$ is the number density of electrons in the energy interval between E and $E + \mathrm{d}E$. The energy distribution of charged particles in astrophysical environments usually has the form:

$$\boxed{n(E)\,\mathrm{d}E = kE^{-p}\mathrm{d}E} \tag{2.19}$$

where k is the normalization of the power law while p is the power-law index. Both k and p are constant. The number of electrons falls toward higher energies with a powerlaw of index $-p$. Integrating Eq.2.17 the total emissivity has the form:

$$\boxed{\epsilon(\nu) \propto \nu^{-\alpha_R}} \tag{2.20}$$

having defined the *spectral index* as

$$\boxed{\alpha_{\rm R} = \frac{p-1}{2}} \tag{2.21}$$

In the case of FSRQs where the radio continuum has a slope of $\alpha_{\rm R} \simeq 0.5$, this means that the spectrum is of the form $f(\nu) \propto \nu^{-0.5}$ and the electron energy distribution satisfies $n(e) \propto E^{-2}$. The high-energy cutoff of the synchrotron spectrum is then defined by the maximum critical frequency of the most energetic electrons, $\nu_{c,max}$.

2.2.3 Synchrotron Self-Absorption

Under the conditions of an optically thin plasma and that the emitted radiation will travel unabsorbed all the way to the observer, one would expect a continuously rising spectrum as one moves to lower and lower frequencies. In reality this is not observed and the spectrum breaks at a certain frequency, known as *break frequency*.

Allowing self-absorption, the synchrotron light produced in the plasma can be then absorbed by the same population of electrons. This will be most efficient when the frequency of the synchrotron radiation is close to the critical frequency ν_c of the absorbing electron, as described in Eq.2.16. The frequency ν_c is proportional to the square of the electron's energy $\nu_c \propto E^2$. Toward higher energies, the density of electrons falls off with a power law with slope p, thus, the chance for a photon to escape is larger the higher its energy, and the larger the emissivity $\epsilon(\nu)$ of the synchrotron radiation. For low frequencies on the other hand, the emitting plasma will be optically thick. This effect of self-absorption being higher for lower frequencies is competing with the intrinsic increase of the emissivity toward higher wavelengths. There is a characteristic frequency where the emitting region changes from being optically thick to optically thin, with a proportionality of (Marscher, 1987):

$$\nu_{sa} \propto B^{1/5} f^{2/5}(\nu_{sa}) \Phi^{-4/5} \tag{2.22}$$

where $f(\nu_{sa})$ is the observed flux at the transition frequency, B the strength of the magnetic filed, and Φ the observed angular size of the emitting region. The practical effect of Synchrotron self-absorbtion is illustrated in Fig.2.7.

2.2.4 Polarization

Synchrotron emission of a single charged particle is polarized. This means that the electromagnetic wave's electric field has a specific orientation. There are two types of polarization: the electric field can be oriented in a single direction (linear polarization), or the polarization vector can rotate (circular or elliptical polarization). In the latter case the electric field vector describes an ellipse in a plane

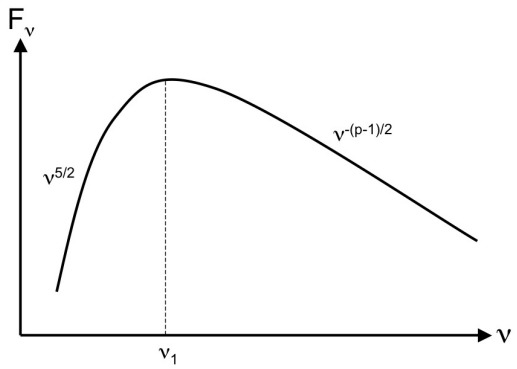

Figure 2.7: Synchrotron self-absorption leads to two emitting regimes where the first (optically thick) has a slope of $5/2$ whereas the second (optically thin) starts at $\nu_1 \equiv (\nu/\nu_{sa}) \cdot (1-p)/2$ and proceeds with slope of $(1-p)/2$.

perpendicular to the propagation direction of the wave. The synchrotron radiation of the single charged particle is thus elliptically polarized. The sense of polarization will depend on whether the line of sight lies inside the circle described by the cone, or outside of it. If one's line of sight lies within the cone of the synchrotron radiation, one will observe linearly polarized emission. In most astrophysical scenarios it is possible to assume that the observed plasma is composed by particles with different pitch angles. Thus, the elliptical polarization contributions of the single particles will cancel out and an ensemble of electrons as the one described before (Sec.2.2.3), will not produce elliptically polarized light. Instead it will result in partially linearly polarized radiation. The degree of polarization then depends on the ratio between the power per unit frequency emitted in parallel and perpendicular directions with respect to the projection of the magnetic field on the plane of the sky. Assuming an energy distribution as the one in Eq.2.19, the degree of linear polarization is

$$\Pi = \frac{p+1}{p+7/3} \tag{2.23}$$

giving a second method for determining the power-law index of the electron energy distribution.

2.3 Inverse Compton and γ-ray Emission

Compton scattering is the inelastic scattering of a photon by a charged particle, usually an electron because of its larger cross-section in respect to the one of protons. The result of this process is a decrease of the photon's energy (which, at the beginning, may be an X-ray or γ-ray photon), which leads to an increase of its wavelength. This is known as the *Compton effect*.

2.3.1 Compton Effect

A condition for Thomson scattering is the low energy of the photon in comparison with the charged particle. If this requirement is dropped and the photon can have an energy comparable to the rest mass of the charged particle, it is necessary to consider quantum mechanical effects. This will reduce the effective cross-section relative to the Thomson case. Including both effects, the energy transfer to the charged particle and the possibility of high photon energies, leads to the case of Compton scattering. The energy loss of the photon is $\Delta E/E = h\Delta\nu/\nu = hc\lambda/\Delta\lambda$ with

$$\Delta\lambda = \lambda' - \lambda = \frac{h}{mc}(1 - \cos\theta) \tag{2.24}$$

where $h \simeq 6.63 \cdot 10^{-34}$ J $\cdot$ s is the Planck constant and θ the angle between the photon and the particle. In the case of electrons the formula reduces to:

$$\Delta\lambda = \lambda' - \lambda = \frac{h}{m_e c}(1 - \cos\theta) \tag{2.25}$$

where $\lambda_c = h/m_e c \simeq 2.43 \cdot 10^{-10}$ cm is the Compton wavelength of an electron.

The resulting energy $E \equiv E_2$ of the photon after the Compton scattering is

$$E_2 = \frac{E_1}{1 + \frac{E_1}{mc^2}(1 - \cos\theta)} \tag{2.26}$$

with E_1 being the energy of the photon before the scattering. Thus, in the limit of $E_1 << mc^2$, $E_2 = E_1$, and the scattering is elastic as in the case described by Thomson, where no energy is transferred to the electron.

2.3.2 Inverse Compton Scattering (IC)

When the electron is moving at relativistic speeds, the Compton process can lead to the opposite effect: the low-frequency photon can gain in energy through the so-called inverse Compton effect. In the case of Compton scattering the photon loses energy which is transferred to the electron, while in the IC the roles are inverted. Because in this case the condition $h\nu << m_e c^2/\gamma$ is fullfilled, it is possible to use the Thomson cross-section.

The starting point of the treatment assumes that the laboratory frame in which the observed scattering event is L, while the frame of the relativistic electron with Lorentz factor γ is L', which is at rest before the event. In the electron's frame L' the energy of the photon is much smaller than the rest energy of the electron, so $h\nu' << m_e c^2/\gamma$. Thus, the center of momentum is close to that of the relativistic electron. Following the relativistic Doppler shift formula the energy of the photon

in L' is:

$$h\nu' = \gamma h\nu \left(1 + \frac{v_e}{c}\cos\theta\right)$$

where θ is the angle between the direction of the photon and of the incoming electron, traveling at speed v_e in the laboratory frame L. In the electron's frame this angle appears smaller:

$$\sin\theta' = \frac{\sin\theta}{\gamma\left(1 + \frac{v_e}{c}\cos\theta\right)}$$

Because in L' the photon energy is small compared to the electron rest energy, the event can be treated as Thomson scattering. As this is an elastic scattering process, the energy of the photon in the electron's frame does not change, meaning that $E'_2 \simeq E'_1$. Transforming this expression back into the laboratory frame L the result is:

$$E_2 \simeq \gamma^2 E_1$$

The photon gains energy in proportion to the square of the Lorentz factor γ of the electron. For relativistic electrons this means that a photon in the radio domain can be up-scattered to the optical or even X-ray range in the IC process. The maximum energy gain of the photon is determined by the energy conservation of the process as seen in the laboratory frame L:

$$E_2 \leq E_1 + \gamma m_e c^2$$

The total power (in other words, the luminosity) of the IC process will naturally depend on the density of photons $n_{\rm ph}$ available for the scattering. Thus, the luminosity $L_{\rm IC}$ of the IC component will be:

$$L_{\rm IC} \propto n_{\rm ph}\gamma^2 E_1$$

It means that the luminosity is proportional to the energy density of the photon field:

$$L_{\rm IC} \propto \gamma^2 U_{\rm ph}$$

The resulting $L_{\rm IC}$ will depend on the cross-section for the IC process. Recalling that this scattering can be treated as elastic, the Thomson cross-section $\sigma_{\rm T}$ applies. The single electron will "see" per unit time an incoming energy from the photons, which is the product of the speed of the incoming photons c, the cross-section of the process $\sigma_{\rm T}$, and the energy density of the photon field $U_{\rm ph}$:

$$\frac{{\rm d}E}{{\rm d}t} = c\sigma_{\rm T} U_{\rm ph} \tag{2.27}$$

Considering the relativistic Doppler shift too, the resulting luminosity is:

$$\begin{aligned} L_{\rm IC} &= \frac{4}{3}\frac{v_e^2}{c^2} c\sigma_{\rm T}\gamma^2 U_{\rm ph} \\ \Rightarrow L_{\rm IC} &= \frac{4}{3}\frac{v_e^2}{c}\sigma_{\rm T}\gamma^2 U_{\rm ph} \end{aligned} \tag{2.28}$$

In astrophysical sources, one has to deal with not only a single electron but with electron distributions, as in the case of synchrotron radiation (Sec.2.2.2). In order to determine the luminosity of the IC process $L_{\rm IC}$, one has to integrate over the single scatterings applying an energy distribution for the electron energies, assuming that it is a simple power law of the form

$$N(E)\mathrm{d}E = k_E E^{-p}\mathrm{d}E = k_\gamma \gamma^{-p}\mathrm{d}\gamma$$

with $N(E)$ being the number of electrons at a given energy E, p the slope of the power law, and k_γ the normalization constant. Assuming that the electrons are highly relativistic, $v_e/c \simeq 1$, and that they have a minimum Lorentz factor γ_{min} and a maximum γ_{max}, the final result is:

$$L_{\rm IC} = \frac{4}{3} c\sigma_{\rm T} U_{\rm ph} k_\gamma \frac{\gamma_{\rm max}^{3-p} - \gamma_{\rm min}^{3-p}}{3-p} \tag{2.29}$$

2.3.3 Synchrotron Self-Compton (SSC)

The synchrotron self-Compton (SSC) process describes the case in which the seed photons of the IC scattering are provided by the synchrotron emission itself. These photons are then up-scattered by the same electron population responsible for the synchrotron emission. In order for the photons to interact with the electron population, the plasma has to be optically thick. While the luminosity of IC scattering is proportional to the energy density of the photon field (Eq.2.28), the luminosity of the synchrotron radiation (i.e., the photon field for the IC process) is proportional to the magnetic field density (Eq.2.14a,2.14b):

$$\boxed{\frac{L_{\rm SSC}}{L_{\rm sync}} = \frac{U_{\rm rad}}{U_B}} \tag{2.30}$$

The ratio between the inverse Compton versus synchrotron radiation flux for a spherical source with radius R, following Ghisellini et al. (1993), is:

$$\frac{f_\nu^{\rm IC}}{f_\nu^{\rm sync}} \simeq k\left(\alpha\right) R n_0 \ln\left(\frac{\nu_{\rm max}}{\nu_{\rm sa}}\right)\left(\frac{\nu_{\rm sync}}{\nu_{\rm IC}}\right)^{\alpha} \tag{2.31}$$

Here α is the spectral index in the radio band, $k(\alpha) \simeq 0.08\alpha + 0.14$, $\nu_{\rm max}$ is the max-

imum frequency reached by the synchrotron radiation as defined by the maximum Lorentz factor $\gamma_{\rm max}$ (Eq.2.29), $\nu_{\rm sa}$ is the frequency where the synchrotron emission reaches its maximum (Eq.2.22), $\nu_{\rm sync}$ is the frequency where the synchrotron (radio) flux is measured and $\nu_{\rm IC}$ is the frequency at which the IC component in the X-ray or γ-ray bands are measured. The normalization n_0 refers to an electron energy distribution of the form:

$$n = \int_{\gamma_{\rm min}}^{\gamma_{\rm max}} n_0 \gamma^{-p} {\rm d}\gamma$$

Also the up-scattered photons of the IC process can contribute again to the photon field's energy density $U_{\rm rad}$, leading to multiple SSC scattering. This effect is very sensitive to the source brightness, and above a certain brightness temperature the IC losses become so significant that they cool the electrons efficiently.

The localization of where the physical processes described in Sec.2.2 and 2.3 occour in AGNs is illustrated in Fig.2.8, where in addition there is a briefly description of some others.

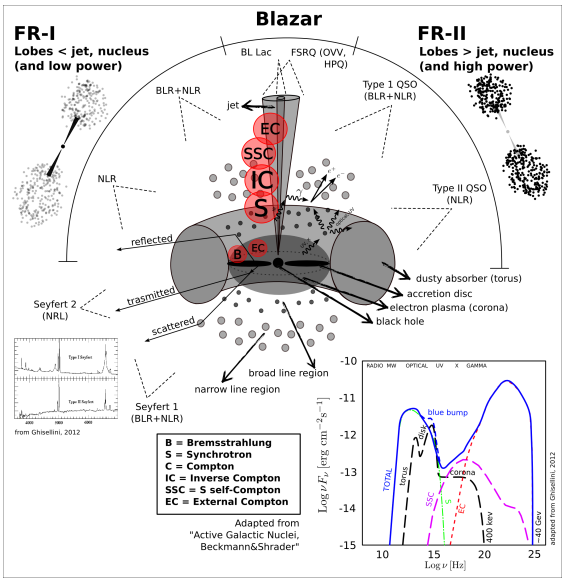

Figure 2.8: This is a review of Fig.1.7, representing again the Unified Scheme but focusing on the physical processes occurring in AGNs. There are two radiation processes not mentioned in 2.2: brehmsstrahlung and External Compton (EC). The former is caused by the deceleration of a charged particle when it is deflected by another's one electric field, leading to the EM emission of the kinetic energy lost during the interaction; typically it is an electron that is decelerated by an atomic nucleus. This process is also known as *free-free* emission because the quantum mechanical states of the particles involved are not bound. The latter is an IC process where the seed photons come from "external regions" (the BLR or the disk) instead of being generated by the electrons gyrating around the magnetic field lines and which are responsible for SSC.

2.4 BLAZAR model

Blazars are the most extreme class of AGNs known. They have been observed at all wavelengths, from radio through Very High Energy (VHE) γ-rays. The broadband continuum SEDs of blazars are dominated by non-thermal emission and consist of two distinct, broad components: a low-energy component from radio through UV or X-rays, and a high-energy component from X-rays to γ-rays up to above 1 TeV.

They are subdivided into BL Lac objects and FSRQs (Sec.1.7), which are again divided into Optically Violent Variables (OVVs) and Highly Polarized Quasars (HPQs).

The emission from blazars is known to be variable at all wavelengths, in particular for FSRQs. This is the reason why they are also referred to as OVVs. Variations in blazars are reported on time scales from years down to less than a day, the so-called intraday variability (IDV).

The criterion used to distinguish between FSRQs and BL Lacs is the Equivalent Width (EW) of the emission lines, and a dividing line of EW=5Å is applied, with the BL Lac objects having only lines below that value. This dividing line is somewhat arbitrary, because the continuum emission of blazars is variable and so is the EW of the lines.

Blazars, defined by the location of the peak of the low-energy (synchrotron) SED component, are sub-divided into several types:

- Low Synhrotron Peaked (LSP), consisting of FSRQs and Low Frequeny Peaked BL Lac Objects (LBLs), having synchrotron peak in the IR regime, at $\nu_s \leq 10^{14}$Hz;
- Intermediate Synchrotron Peaked (ISP), where Intermediate BL Lac Objects (IBLs) are found, have their synchrotron peak at optical-UV frequencies in the range $10^{14}\text{Hz} < \nu_s < 10^{15}\text{Hz}$;
- High-Synhrotron-Peaked (HSP), almost all known to be High Frequeny Peaked BL Lac Object (HBL), are synchrotron peaked at X-ray energies with frequncies $\nu_s > 10^{15}$Hz.

This subdivision leads to what is referred to as *blazar sequence*.

As shown in Fig.2.9 two peaks are present in all the SEDs. The first one – due to synchrotron emission – is anticorrelated with the source luminosity, and it is moving from $\sim 10^{16}$–10^{17}Hz for less luminous sources to $\sim 10^{13}$–10^{14}Hz for the most luminous ones. The X-ray spectrum becomes harder while the γ-ray one softens with increasing luminosity, indicating that the second (Compton) peak of the SEDs also moves to lower frequencies from $\sim 10^{24}$–10^{25}Hz for less luminous

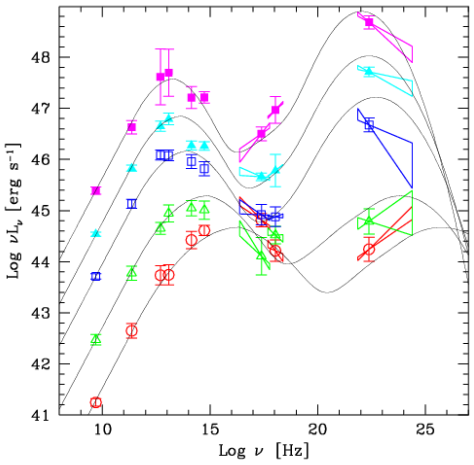

Figure 2.9: Average SEDs for the "total blazar sample" from Fossati et al. (1998). *Left*: Synchrotron peaks, starting from LSPs objects located on top down to HSPs at the bottom as the frequency ν increases. *Right*: High energy Inverse Compton peaks, visibly correlated to the other ones.

sources to $\sim 10^{21}$–10^{22}Hz for the most luminous ones. Therefore, the frequencies of the two peaks are correlated: the smaller the $\nu_{\rm peak,sync}$, the smaller the peak frequency of the high energy component. Increasing $L_{\rm 5GHz}$ increases the γ-ray dominance, which is the ratio of the power emitted in the IC and synchrotron components, estimated with the ratio of their respective peak luminosities.

Basically, blazars are AGNs observed face-on , with the jet pointing toward the observer. The special jet orientation explains the general peculiar characteristics: high observed luminosity, very rapid variability, high polarization (when compared with non-blazar quasars), and the apparent superluminal motions detected along the first few parsecs of the jets in most blazars.

The peculiar features of blazars are commonly interpreted as being the consequence of a relativistic AGN jet pointing directly along the line of sight. This situation can occur if the AGN structure illustrated in the Unified Model (Sec.1.3) is seen in a face-on orientation. Due to effects of relativistic beaming (Sec.2.2.1), variability and polarization (Sec.2.2.4) of the jet radiation, it will dominate the resulting spectrum. Blazars will then fall into the BL Lac and FSRQ families, depending on the relative power of their jets with respect to the underlying central engines. If the accretion process is radiatively inefficient, or the jet dominates, the source will show a simple power law spectrum and appear as a BL Lac. If, on the contrary, the central engine and BLR give an appreciable contribution, the object will be classified as a FSRQ.

CHAPTER 3

DATA SELECTION AND ANALYSIS

As stated earlier, AGNs emit EM radiaton over a large range of frequencies, from radio up to γ-rays. As a consequence, finding sources that have been detected in many EM windows is a good way to find these objects.

Keeping this in mind, we will cross-match the coordinates of the sources detected by the following surveys:

- SDSS (Alam et al., 2015) (UV/optical)
- ROSAT (Truemper, 1982) (X)
- NVSS (Condon et al., 1998a), FIRST[1] (Becker et al., 1995) (radio)
- Fermi (Atwood et al., 2009) (γ)

3.1 Description of the Surveys

3.1.1 SDSS

The Sloan Digital Sky Survey (SDSS) has created the most detailed three-dimensional maps of the Universe ever made, with deep multi-color images of one third of the sky, and spectra for more than three million astronomical objects.

After nearly a decade of design and construction, the SDSS saw first light on its giant mosaic camera in 1998 and entered routine operations in 2000. It has progressed through several phases, SDSS-I (2000–2005), SDSS-II (2005–2008), SDSS-III (2008–2014), and currently SDSS-IV, which has started in 2014.

The data used in this work were collected during the SDSS-III phase, using the Sloan Foundation 2.5-meter Telescope at Apache Point Observatory in New Mexico

[1]Faint Images of the Radio Sky at Twenty-Centimeters (FIRST): `http://sundog.stsci.edu/`

(Gunn et al., 2006). The telescope is a modified two-corrector Ritchey-Chrétien design with a 2.5m, f/2.25 primary and a 1.08m secondary; it has a Gascoigne astigmatism corrector, and one of a pair of interchangeable highly aspheric correctors near the focal plane: one for imaging and the other for spectroscopy. The final focal ratio is f/5. The telescope is instrumented by a wide-area, multiband Charge-Coupled Device (CCD) camera and a pair of fiber-fed double spectrographs. One of the features of the telescope is that it has excellent image quality and small geometric distortions over a wide wavelength range (3000-10,600 Å) in the imaging mode, and good image quality combined with very small lateral and longitudinal color errors in the spectroscopic one.

In this work, the optical data were retrieved thanks to the SDSS's Data Release 12 (DR12) (Alam et al., 2015). The images were collected during 2002–2014 by the following surveys:

SEGUE and SEGUE-2 (Yanny et al., 2009)

The Sloan Extension for Galactic Understanding and Exploration (SEGUE), whose characteristics are reported in Tab.3.1, has collected spectra of nearly 230,000 stars of several Spectral Types (TSps) to investigate the MW structure. Building on this success, SEGUE-2 spectroscopically observed around 119,000 unique stars, focusing on the in situ stellar halo of the Galaxy, from distances of 10 to 60 kpc. Both surveys used the two SDSS fiber spectrographs. For a SEGUE line-of-sight, each of these spectrographs had acquired data for 320 of the 640 fibers over a field of 7°× 7°. The fibers were plugged into aluminum plates mounted in the telescope focal plane; each set of 640 spectra in a single field is referred to as a *plate*. The spectrograph resolution is 2Å at 5000Å.

eBOSS (Dawson et al., 2013)

SDSS-III's Extended Baryon Oscillation Spectroscopic Survey (eBOSS) was built to map the spatial distribution of Luminous Red Galaxies (LRGs) and quasars to detect the characteristic scale imprinted by baryon acoustic oscillations in the early universe. By using the baryon acoustic oscillation scale as a physically calibrated ruler, BOSS will determine the absolute cosmic distance scale with precision of 1.0% at $z = 0.35$, 1.1% at $z = 0.6$, and 1.5% at $z = 2.5$, z being the redshift (3.4.3), achieving tight constraints on the equation of state of dark energy. In addition to constraining cosmological models, BOSS is delivering an outstanding sample of galaxies and quasars ideally suited to probing the formation and evolution of galaxies in the Universe. The sheer size of BOSS, coupled with the BOSS spectrograph resolution, will greatly enhance this area of science.

SEGUE	
CCDs	4, 2048 × 2048, SITe/Tektronix, 49.2mm^2
Channels	3800–6150 Å (blue), 5800–9200 Å (red)
Number of fibers	320 × 2
Fiber diameter	3″
Wavelength calibration	Hg, Cd, and Ne arc lamps, rms error of 0.07 pixels (10 km s^{-1})
Flat field	quartz lamps
Flux calibration	Standard stars in each field, tied to colors observed with the imaging camera
Pixel size	69 km s^{-1}
Pixel spacing	log-wavelength (10^{-4} dex)
Units	10^{-17}erg s^{-1}cm^{-2}Å^{-1}
Spectral resolution	ranges from 1850 to 2200
Integration time	Exposures are taken until the cumulative mean S/N per pixel exceeds 4 for a fiducial fiber magnitude of $g = 20.2$ and $i = 19.9$. Typically 3 exposures of 15 minutes each under good conditions.

BOSS	
Number of spectrographs	2
Spectral resolution	from 1560@3700 Å to 2270@6000 Å (blue channel), from 1850@6000 Å to 2650@9000 Å (red channel)
Wavelength coverage	3600–10,400 Å
Fiber diameter	2″
Pixel spacing	log-wavelength (10^{-4} dex)
Units	10^{-17}erg s^{-1}cm^{-2}Å^{-1}
CCDs	red side: 4000K × 4000K fully-depleted LBNL CCDs with 15 μm pixels blue side: blue-sensitive 4000K × 4000K e2V CCDs with 15 μm pixels
Collimator coating reflectivity	>95% from 420 nm to 1000 nm

Table 3.1: SDSS-I/-II SEGUE and BOSS Spectrographs' characteristics as published on the SDSS website.

3.1.2 ROSAT

The Röntgensatellit (ROSAT) was an X-ray observatory developed through a cooperative program between Germany, United States, and United Kingdom. The satellite was designed and operated by Germany, and was launched by the United States on June 1, 1990. ROSAT had a design life of 18 months but it was turned off only on February 12, 1999. Its launch into space marked the start of a mission that allowed researchers to perform for the first time an all-sky survey of X-ray sources with an imaging telescope.

The main assembly was a German-built imaging X-ray Telescope (XRT) with three focal plane instruments: two German Position Sensitive Proportional Counters (PSPCs) and the US-supplied High Resolution Imager (HRI). Their diameter fields in the focal plane where ∼2 degrees and ∼40 arcmins respectively. Coaligned to the XRT, having its own mirror system and star sensor, there was a British-supplied Extreme Ultraviolet (EUV) telescope, the Wide Field Camera (WFC).

A PSPC is a thin-window gas counter. In this instrument an incoming X-ray photon produces an electron cloud whose position and charge are detected using wire grids. The German PSPCs had an accuracy of about 120 μm for the position. The electron cloud's charge usually corresponds to the incoming photon's energy.

The X-ray mirror assembly was a grazing incidence four-fold nested Wolter I telescope with an 84cm diameter aperture and 240cm focal length. The angular resolution was less than 5″ at Half Energy Width (HEW). The HRI was composed

by two cascaded Microchannel Plates (MCPs) with a crossed grid position readout system. It had negligible energy resolution but provided a relative time one down to 61 μs. The XRT assembly was sensitive to X-rays between 0.1 to 2 keV.

The WFC was an EUV telescope with a 0.525 m focal-length mirror assembly consisting of 3 nested Wolter-Schwarzschild mirrors (Chase and van Speybroeck, 1973), leading to a 5° field-of-view with spatial resolution 2.3 arcmin HEW. The focal plane instrumentation consisted of a curved MCP with a carousel containing 8 filters, of which 6 were science filters.

The ROSAT mission was divided into two phases. After a two-month on-orbit calibration and verification period, an all-sky survey was performed for six months using the PSPC in the focus of XRT, and in two EUV bands using the WFC. The survey was carried out in the scan mode. The second phase consisted of the remainder of the mission and was devoted to pointed observations of selected astrophysical sources. In ROSAT's pointed phase, observing time was allocated to Guest Investigators from all three participating countries through peer review of submitted proposals.

During the mission, ∼120,000 sources were found in the ROSAT All-Sky Survey (RASS), and about 220,000 more were discovered in pointed ROSAT observations.

3.1.3 NVSS and FIRST

NVSS

The NRAO VLA Sky Survey (NVSS) is a 1.4 GHz continuum survey covering the entire sky north of ∼-40° declination, making use of the Karl G. Jansky Very Large Array (VLA), which is a component of the National Radio Astronomy Observatory (NRAO).

The VLA is a radio astronomy observatory located on the Plains of San Agustin, New Mexico. It comprises, in an Y-shaped array of 25-meter radio telescopes, a total of 27 units, and has all the equipment, instrumentation, and computing power to function as an interferometer. Each of the massive telescopes is mounted on double parallel railroad tracks, so the radius and density of the array can be transformed to focus on particular wavelength bands. The VLA can vary its resolution over a range exceeding a factor of ∼50 through movement of its component antennas. There are four basic antenna arrangements, called configurations, whose scales vary by the ratios 1 : 3.28 : 10.8 : 35.5 from smallest to largest. These configurations are denoted D, C, B, and A, respectively. In addition, there are 3 "hybrid" configurations labelled DnC, CnB, and BnA, in which the North arm antennas are deployed in the next larger configuration than the South East (SE) and South West (SW) arm antennas.

Date	Frequencies	Bandpass	Integration
Before 2011	1365, 1435 MHz	2×7 3-MHz channels	180 seconds
After 2011	1335, 1730 MHz	2×64 2-MHz channels	60 seconds

Table 3.2: Specifications of the bandpasses used by FIRST during the years

All VLA antennas are outfitted with eight receivers providing continuous frequency coverage from 1 to 50 GHz. These receivers cover the frequency ranges of 1–2 GHz, 2–4 GHz, 4–8 GHz, 8–12 GHz, 12–18 GHz, 18–26.5 GHz, 26.5–40 GHz, and 40–50 GHz. In addition, all antennas of the VLA have receivers for lower frequencies, enabling observations at P-band (230–470 MHz). These low frequency receivers also work at 4-band (54 to 86 MHz), and new feeds have been deployed on a small number of VLA antennas to observe at this frequency range.

Astronomers using the VLA have made key observations of BHs and protoplanetary disks around YSOs, discovered magnetic filaments and traced complex gas motions at the MW's center, probed the Universe's cosmological parameters, and provided new knowledge about the physical mechanisms that produce radio emission.

FIRST

FIRST is a project designed to produce the radio equivalent of the First Palomar Sky Survey (POSS-I)[2] over 10,000 square degrees of the North and South Galactic Caps. The data are edited, self-calibrated, mapped, and "cleaned" using an automated pipeline based largely on routines in the Astronomical Image Processing System (AIPS). A final atlas of maps was produced by coadding the twelve images adjacent to each pointing center. These maps have 1.8″ pixels, a typical Root Mean Square (rms) of 0.15 mJy[3], and a resolution of 5″. The noise in the coadded maps varies by only 15% from the best to the worst places in the maps, except in the vicinity of bright sources ($>$ 100 mJy) where sidelobes can lead to an increased noise level. At the 1 mJy source detection threshold, there are ∼90 sources per square degree, ∼35% of which have resolved structure on scales from 2–30″.

A source catalog including peak and integrated flux densities and sizes derived from fitting a two-dimensional Gaussian to each source was generated from the coadded images. The astrometric reference frame of the maps is accurate to 0.05″, and individual sources have 90% confidence error circles of radius less than 0.5″

[2] POSS-I was carried out in the 1950's using the 48-inch Oschin Schmidt telescope at Mount Palomar in southern California. This survey was carried out using photographic plates.

[3] $1\text{Jy} = 10^{-23}\text{erg cm}^{-2}\text{s}^{-1}\text{Hz}^{-1}$

at the 3 mJy level and 1″ at the survey threshold. Approximately 15% of the sources have optical counterparts at the limit of the POSS-I plates (E[4]∼20.0); unambiguous optical identifications (<5% false rates) are achievable to m_v ∼24. The survey area has been chosen to coincide with that of the SDSS; at the m_v ∼23 limit of SDSS, ∼40% of the optical counterparts to FIRST sources are detected.

3.1.4 Fermi

The Fermi Gamma-ray Space Telescope, launched on 11 June 2008 and formerly called the Gamma-ray Large Area Space Telescope (GLAST), is a space observatory being used to perform γ-ray astronomy observations from low Earth orbit. Its main instrument is the Large Area Telescope (LAT), with which astronomers are performing an all-sky survey in order to study astrophysical and cosmological phenomena such as AGNs, pulsars, other HE sources and dark matter. Another instrument aboard Fermi, the Gamma-ray Burst Monitor (GBM), formerly named GLAST Burst Monitor, is being used to study γ-ray bursts. The mission is a joint venture of NASA, the United States Department of Energy, and government agencies in France, Germany, Italy, Japan, and Sweden.

The Fermi observatory operates primarily in an all-sky scanning survey mode that maximizes observing time while maintaining excellent uniformity. This means that the LAT rarely stares at a single point in the sky. Rather, the boresight of the LAT continuously scans it, alternating between the northern and southern hemispheres each orbit. This strategy makes the best use of the LAT's large 70° half-angle field of view, and provides 30 minutes of livetime on each point in the sky every two orbits.

The LAT is a wide-field γ-ray telescope (20 MeV–300 GeV). From the start of regular observations in August 2008 until December 2013 the LAT continuously scanned the sky, providing all-sky coverage every two orbits (approximately three hours). In December 2013 the LAT transited to a modified observing strategy that combines pointed observations – designed to increase coverage of the Galactic center – together with sky survey observations. LAT observations are interrupted by occasional additional pointed observations, including target of opportunity ones, and autonomous repointing of the observatory to follow Gamma-ray Bursts (GRBs) afterglows, and by regular passages through the South Atlantic Anomaly (a region of high particle backgrounds).

The LAT has four subsystems that work together to detect γ-rays and to reject signals from the intense bombardment of cosmic rays. For every γ-ray that enters the instrument, it will have to filter out ∼ 100,000–1,000,000 cosmic rays, charged

[4]Kodak 103a-E (Scott, 1986)

particles that resemble the ones produced by γ-rays. The four main subsystems are:

Tracker

It consists of a four-by-four array of tower modules. Each tower module consists of layers of silicon-strip particle tracking detectors interleaved with thin tungsten converter foils. The silicon-strip detectors precisely measure the paths of the electron and positron produced from the initial γ-ray. The pair-conversion signature is also used to help reject the much larger background of cosmic rays.

Calorimeter

The Calorimeter measures the energy of a particle when it is totally absorbed. It is made of a material called *cesium iodide* (CsI) that produces flashes of light whose intensity is proportional to the energies of the incoming particle. The Calorimeter also helps to reject cosmic rays, since their pattern of energy deposition is different from that of γ-rays.

Anticoincidence Detector (ACD)

The ACD is the first filter devoted to rejection of cosmic rays. It consists of specially formulated plastic tiles that produce flashes of light when hit by charged-particle cosmic rays (but not by γ-rays, which are electronically neutral). The ACD forms a "hat" that fits over the tracker.

Data Acquisition System (DAQ)

It collects information from the Tracker, the Calorimeter, and the ACD. It makes the initial distinction between unwanted signals from cosmic rays and real γ-ray signals, deciding which should be relayed to the ground. This system also does an on-board search for GRBs. The DAQ consists of specialized electronics and microprocessors.

The GBM is an all-sky monitor (10 keV–25 MeV) that detects transient events such as occultations and GRBs. It consists of 12 detectors made of *sodium iodide* (NaI) for catching X-rays and low-energy γ-rays plus two detectors made of bismuth germanate ($Bi_4Ge_3O_{12}$) for HE γ-rays. Together, they cover the detection from X-rays to γ-rays between 8 keV and 30 MeV, overlapping with the LAT's lower-energy limit, picking up about 200 GRBs per year, as well as solar flares and other transient events.

NASA designed the mission with a five-year lifetime, with a goal of ten years of operations: in August 2013 Fermi started its 5-year mission extension so it is still operating.

3.2 Survey Combination Procedures

The purpose of this study is to investigate the demographics of AGNs suspected to host a relativistic jet closely aligned to our line of sight. Some of these objects have already been identified and listed as known blazar sources, but many other blazar candidates, still lacking a firm classification, exist. Here we combine observations performed at multiple wavelengths in order to compare the properties of these objects with those of well established blazar sources, with the aim of understanding whether they are good candidates for the investigation of high energy jet physics.

The very first thing done was a search for a suitable catalog of known blazars in order to cross-match their coordinates with the ones of the cross-match of the sources detected by the surveys described above (Sec.3.1).

The choice was done in favour of the *BZCAT4* catalog (nowadays BZCAT5[5]), which will be briefly described in the following subsection.

3.2.1 The *Roma-BZCAT* catalog

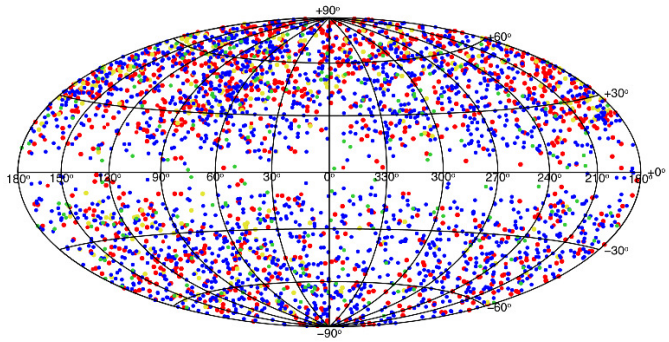

Figure 3.1: View of the sources present in the 5$^{\text{th}}$ edition of the Roma BZCAT.

The "BZ4" is a catalogue of blazars based on multifrequency surveys and on an extensive review of the literature. This catalogue was built as a tool useful for the identification of the extragalactic sources that lie within the detection limit of present and future experiments for X and γ-ray astronomy at the publishing time, like SWIFT, Astro-rivelatore Gamma a Immagini LEggero (AGILE), and GLAST.

The fourth edition of the "catalog of known Blazars" BZCAT4 (Massaro et al., 2009) was included in the latest 5$^{\text{th}}$ release simply by adding a "5" in front of the old code of every listed source (i.e. BZQJ0001+1914 $\longrightarrow$ 5BZQJ0001+1914). The codes are referred to as:

- BZB = BL Lac objects, used for AGNs with a featureless optical spectrum

[5] `http://www.asdc.asi.it/bzcat/`

or only with absorption lines of galactic origin and weak and narrow emission lines;

- BZ? = BL Lac candidates;
- BZQ = FSRQs, with an optical spectrum showing broad emission lines and dominant blazar characteristics;
- BZU = blazars of uncertain type, adopted for sources with peculiar characteristics but also showing blazar activity: for instance, occasional presence/absence of broad spectral lines or features, transition objects between a radio galaxy and a BL Lac, galaxies hosting a low luminosity blazar nucleus and so on.

3.2.2 Other Catalogs

The optical data were planned to be taken from the SDSS's site and this is the reason why, at first, other surveys have been taken in account for identifying sources of interest. Basically, the target was to retrieve a list of objects having been detected in X-rays and having a radio counterpart.

In order to achieve the target it was necessary to get access to a database capable to manage as many catalogs as possible; at the time of writing, the best available choice is the *VizieR*[6]. The VizieR Catalogue Service is an astronomical catalog service provided by Centre de données astronomiques de Strasbourg (France).

Taking advance of its capabilities three of the four catalogs chosen were easily downloaded:

- ROSAT All-Sky Survey Faint Source Catalog (RASSFSC) (Voges et al., 2000)
- 1.4GHz NVSS (Condon et al., 1998b)
- The FIRST Survey Catalog, Version 2014Dec17 (Helfand et al., 2015)

The last catalog of sources involved in this work is the *LAT 4-year Point Source Catalog (3FGL)*[7] which, at the time of writing, is not present in the VizieR's database but it is donwloadable in FITS file format[8].

[6] `http://vizier.u-strasbg.fr/viz-bin/VizieR-2`
[7] `http://fermi.gsfc.nasa.gov/ssc/data/access/lat/4yr_catalog/`
[8] `http://fermi.gsfc.nasa.gov/ssc/data/access/lat/4yr_catalog/gll_psc_v16.fit`

3.2.3 Sky area and cross-matches

As written in Sec.1.4 the VO has lots of advantages for end users in order to perform a research. In this case the webservices used in order to retrieve data and do the first basic analysis on them were basically three: the VizieR, *X-Match*[9], and SDSS's *CasJobs*[10] services. The last two have the capabilities to do cross-match jobs: the former using a GUI while the latter through the SQL language. In addition to this SDSS's CasJobs capability, registered users are permitted to store up to 500,000kB of data into a personal SQL databse, which can be used to "join" the survey's data releases.

Summary

The matches were done in an area of 3600 square degrees ($90° \times 40°$) located in between the following equatorial coordinates:

$$\begin{aligned} \alpha &= 09^{h}00^{m}00^{s}.0 - 15^{h}00^{m}00^{s}.0 \\ \delta &= 10°00'00''.0 - 50°00'00''.0 \end{aligned}$$

This region was selected because it is fully covered by the SDSS spectroscopic survey footprint, thus granting a very high chance to retrieve optical spectra for all the potentially interesting sources. Each of the catalogs was stored both into the *Centre de Données astronomiques de Strasbourg (CDS) Portal*[11] and the SDSS's *CasJobs*[12] services: in the latter case, instead of uploading the search's results directly into the storage area offered to registered users (up to 500MB), an American Standard Code for Information Interchange (ASCII) file was downloaded and manually converted to a Comma Separated Values (CSV) format uploadable to the personal SQL database as a table of its[13].

The double procedure described above, consisting in cross-matching the source coordinates two times using both the X-Match service and the SQL codes executable from the SDSS's site, was made in order to have a feedback on the goodness of the procedure.

Details

The first cross-match made was between the NVSS catalog and the RASSFSC whithin a searching radius of $30''$ around the X coordinates and its result was a table containing a sample of 772 sources. The output given by the X-Match routine

[9] `http://cdsxmatch.u-strasbg.fr/xmatch`
[10] `http://skyserver.sdss.org/casjobs/`
[11] `http://cdsportal.u-strasbg.fr/`
[12] `http://skyserver.sdss.org/casjobs/`
[13] This procedure was not applied for the sources belonging to the 3FGL catalog which were crossed with the use of the software *Topcat*.

was downloaded and manually edited with a text editor in order to be able to store it as a SQL table into the SDSS's CasJob service.

Another cross-match job was done: the coordinates of the 772 objects were crossed against the SDSS DR12 *specobj*'s *view*[14] ones, searching in an inner radius of 3″ around the radio coordinates in order to find optical specra retriavable from the DR12 Science Archive Server (SAS). The SQL code used is reported in appendix (listing 11).

As result there were 323 sources left: their optical coordinates were crossed against the BZCAT4's ones (492) in a searching radius of 3″ in order to know whether the identified sources were already known blazars or not (appendix, listing 12). Afterwards, a column containing this information was added to the SQL table of reference.

3.3 Selection of Optical Spectra

In order to estimate the AGNs' physical parameters needed, the availability of good quality spectra, with measurable continua and emission line widths, is required. This means that each spectrum should have, at least, a Signal to Noise Ratio (S/N) value of 3, with 10 being a good one. The S/N of the final sample, intended as the average of all the values of each single spectrum, is 12.79 (appendix, listing 13).

Some of the outputs of the CasJobs's SQL function *fGetNearestSpecObjEq* are fundamental in order to being able to retrieve the spectra of interest. Recalling how SDSS spectra are taken (3.1.1), anyone of them can be identified with three integer numbers:

Plate

It indicates which SDSS plug plate was used to collect the spectrum.

[14] In SQL, a view is a virtual table based on the result-set of an SQL statement. w3schools.com

MJD

It denotes the Modified Julian Date (MJD) of the night when the observation was carried out. Some plates were observed more than once; these different observations have different MJD values.

FiberId

It corresponds to the fiber number (1–640 for SDSS-I/II; 1–1000 for BOSS).

The SAS gives the opportunity to download data in many ways, starting from a simple search were the input is a set of coordinates to the download of the entire archive stored on the site. In this work's case it was decided to use the "bulk download"[15] feature for optical spectra downloads. Once having created a CSV file containing spectroscopic identifiers described above, it is possible to submit it to the SAS's webpage. As response, the page reloads and updates itself, adding the search results at bottom. By selecting all the spectra and asking for a Flexible Image Transport System (FITS) files bulk download, the system generates a list of Uniform Resource Locators (URLs), which can be used to download the spectra through standard file transfer managers, such as `wget`.

After reduction (Sec.3.4), the spectra were manually inspected using *IRAF*'s[16] *noao.onedspec.splot* task. This check permitted to exclude from the sample the remaining celestial objects, such as stars and normal galaxies, which are not in the focus of this study and could not be filtered out by the selection process. At that point, the number of selected sources became 125.

3.4 Reduction of Optical Spectra

3.4.1 Image Conversion

FITS is an open standard defining a digital file format useful for storage, transmission and processing of scientific and other images, and the most commonly used digital file format in astronomy. FITS is also often used to store non-image data, such as spectra, photon lists, data cubes, or even structured data such as multi-table databases. A FITS file may contain several extensions called Header Data Units (HDUs), and each of these may contain a data object. For example, it is possible to store X-ray and IR exposures in the same file.

SDSS's FITSs, until SDSS-II, were stored as *spPlate* files, each of them containing the combined spectra for all exposures of a given plate. Typically, there are

[15] `http://dr12.sdss3.org/bulkSpectra`
[16] `http://iraf.noao.edu/`

SDSS-II		
HDU0	NPIX × 640 float image	Flux in units of 10^{-17}erg s^{-1}cm^{-2}Å^{-1}
HDU1	NPIX × 640 float image	Inverse variance ($1/\sigma^2$) for HDU 0
HDU2	NPIX × 640 32-bit int image	AND mask
HDU3	NPIX × 640 32-bit int image	OR mask
HDU4	NPIX × 640 float image	Wavelength dispersion in pixels
HDU5 fields	binary table	Plug-map structure from plPlugMapM file
HDU6	NPIX × 640 float image	Average sky flux in units of 10^{-17}erg s^{-1}cm^{-2}Å^{-1}

Table 3.3: SDSS-II's HDUs contents.

SDSS-III		
HDU 0: Header keywords only		
HDU 1 (extname COADD): Coadded Spectrum from spPlate		
Name	**Type**	**Comment**
flux	float32	coadded calibratex flux [10^{-17}erg s^{-1}cm^{-2}Å^{-1}]
loglam	float32	log10 (wavelength [Å])
ivar	float32	inverse variance flux
AND mask	int32	AND mask
OR mask	int32	OR mask
wdisp	float32	wavelength dispersion in pixeld=d log λ units
sky	float32	subtracted sky flux [10^{-17}erg s^{-1}cm^{-2}Å^{-1}]
model	float32	pipeline best model used for classification and redshift

Table 3.4: SDSS-III's first two HDUs contents. There are, at least, other 3 HDUs containing other information or spectra.

three 900s exposures which may have been taken in a single night, or over multiple nights.

Starting from SDSS-III the file format has changed passing to a *spec* files one. The *spec-PLATE-MJD-FIBER.fits* files contain a repackaging of all spectral data for a given plugging (plate, mjd, fiber), including both the coadded spectrum and optionally the individual exposure frames, as well as many other useful information[17]. Basically, the HDUs of interest are HDU0 and HDU1, whose content is reported in Tab.3.4.

In order to obtain the information needed to plot a spectrum with IRAF's splot package it is necessary to extract and elaborate the information stored in HDU1 ([COADD]). Doing this kind of work using IRAF is possible, provided that

[17] `http://data.sdss3.org/datamodel/files/BOSS_SPECTRO_REDUX/RUN2D/spectra/PLATE4/spec.html`

the Space Telescope Science Data Analysis System (STSDAS)[18] external package – which includes the *TABLES* package – has previously been installed. The information stored in HDU1[COADD] has been unhidden using TABLES's *ttools* package capatibilities, executing the *tlcol* task:

```
tlcol spec-7419-56811-0620.fits[COADD]
# spec-7419-56811-0620.fits[COADD]
flux            R          %15.7g ""
loglam          R          %15.7g ""
ivar            R          %15.7g ""
and_mask        I            %11d ""
or_mask         I            %11d ""
wdisp           R          %15.7g ""
sky             R          %15.7g ""
model           R          %15.7g ""
```

Once having known which were the columns of interest (*flux*,*loglam*), the scheme adopted to extract the spectra can be summarized as follows:

1. **Get the columns data**:
   Taking again advantage of the STSDAS capabilities, the content of the two columns was printed to the terminal using the task *stsdas.tables.tdump*, redirecting the ASCII output to text files (appendix, listing 2).

2. **Interpolate the x,y pairs to produce a spectrum**:
   This step was done executing the task *noao.onedspec.sinterp* (appendix, listing 3). Two of the task's parameters which were set with different values are the first (x_1) and the last (x_2) points of the range where the curve has to be generated: for BOSS spectra $x_1 = 3.556302501$ and $x_2 = 4.017033339$ while for SEGUE $x_1 = 3.579783597$ and $x_2 = 3.963787827$. These values correspond to the logarithms of the extremes of detection of the two spectrographs (in Å, Tab.3.1).

3. **Edit the images' headers**:
   IRAF's task *images.imutil.hedit* (header edit) permitted to correctly set headers' field values to *DC-FLAG=1*, *WFITTYPE=LOG-LINEAR*, with the last one being set to *BUNIT*=10^{-17}erg s^{-1}cm^{-2}Å^{-1} (appendix, listing 4).

3.4.2 Reddening Correction

Reddening occurs because interstellar dust absorbs and scatters blue light waves more than red light waves, making astronomical sources appear redder than they

[18]STSDAS is a product of the Space Telescope Science Institute, which is operated by the Association of Universities for Research in Astronomy (AURA) for NASA.

are. This is similar to the effect seen when dust particles in the atmosphere of Earth contribute to red sunsets. The amount of extinction can be significantly smaller or higher in specific directions. The general shape of the UV through NIR extinction curve in our Galaxy is fairly well characterized by the single parameter $R(V)$ (which is different along different lines of sight through the galaxy). $R(V)$ is defined as:

$$\boxed{R\left(V\right) = \frac{A\left(V\right)}{E\left(B-V\right)}} \tag{3.1}$$

and measures the total $A(V)$ to selective $E(B-V) = A(B) - A(V)$ color excess, where $A(B)$ and $A(V)$ are the total extinction in the B and V filter bands expressed in magnitude. $R(V)$ is known to be correlated with the average size of the dust grains causing the extinction. For the MW the typical value for $R(V)$ is 3.1, but it is found to be between 2.5 and 6 for different lines of sight.

IRAF's *noao.onedspec.deredden* task is intended to be used to deredden the spectra. It asks, as input, the spectrum for which the dereddening has to be applied, the value of R, and the type of correction to be applied: $A(V)$ as the absolute extinction at the V band at 5550Å ($A(\lambda)/A(V)$) or the one of Eq.(3.1). The choice was made in favour of the latter type of computation.

For each one of the sources the values of $A(B)$, $A(V)$ were retrieved from the NASA/IPAC Extragalactic Database (NED), using the "Coordinate Transformation & Galactic Extinction Calculator"[19], storing the outputs on a CSV file in order to compute R. Finally, the correction was applied by invoking the `deredden` task through a Command Language (CL) script (appendix, listing 5).

3.4.3 Redshift Correction

The correction for redshift was done in two steps: acquiring the z values at first and applying the Doppler formula to the spectra at last. Using IRAF's splot task in concomitance with the SDSS's *quick look*[20], for each of them the most prominent emission lines (such as Hβ λ4861 or MgII λ2798, as well as the [OIII] λ4959 and [OIII] λ5007) were identified and their wavelengths measured.

After this preliminar sanity check, the z values were requested to the server using the CasJobs's SQL capabilities. *zWarning* values were requested too because spectra having this value equal to zero have no known problems. That was the case for the entire sample, resulting in a further test on the sample integrity.

IRAF's *noao.onedspec.dopcor* task permits to apply the Doppler correction giving as input the spectrum's filename, the desired output's one, and the z value. As

[19] `https://ned.ipac.caltech.edu/forms/calculator.html`

[20] `http://skyserver.sdss.org/dr12/en/tools/quicklook/quicksummary.aspx?id=0x112d06c1a0530139&spec=0x0a2878485f006800`

done before during the images conversions passages, a CL script was written and executed (appendix, listing 6).

3.5 Multiple frequency data

In addition to the optical spectra retrieved from the SAS, other data were needed in order to complete the study. Since AGNs emit broadly throughout the EM spectrum, every window of its gives hints on the different physical processes involved in the phenomenon. Taking in account the unified scheme presented previously (Sec.1.3) and the blazar model proposed in section 2.4, blazar candidates have to be radio-loud (Sec.4.5) and to emit in the HE and VHE windows through X-rays and γ-rays.

The radio data were retrieved from FIRST using the X-Match utility while the searching for γ-ray counterparts, as mentioned earlier, was done with Topcat. FIRST's sources were found in a radius $\lesssim 1''$ from their optical counterparts, with two exceptions (starred in Tab.3.5).

In order to cross-match the sample's sources with the 3FGL catalog it was necessary to withdraw to software installed locally: the X-Match service allows searching radii up to $120''$, which is less than the $5'$ needed. Once having downloaded the catalog in FITS format, Topcat was launched and the catalog's file opened, as well as the CSVs containing the sample's sources coordinates. Finally, using the first HDU of the 3FGL catalog, the cross-matches were done on a searching radius of $5'$ with the *sky* algoritmh. The resulting γ-ray counterpart to the sample sources were 12 (4.5).

The final sample, which will be described in Section 4.3, consists of the 84 sources that are listed in Tab.3.5.

Class	Subclass	α [hh mm ss] [J2000]	δ [deg] [J2000]	Simbad	BZCATALOG 4	SDSS (IAU)	NVSS	1RXS (ROSAT)	z
QSO	BROADLINE	10 23 10.57	+47 51 45.5	4C 48.29A		J102310.58+475145.5	102310+475146	J102308.0+475157	0.581
QSO	BROADLINE	09 41 28.81	+44 47 42.8	5C 5.94		J094128.82+444742.8	094128+444740	J094126.3+444748	0.800
QSO		14 19 46.36	+46 34 24.3	[VV2010c] J141946.3+463423		J141946.36+463424.3	141946+463426	J141946.5+463422	0.546
QSO	BROADLINE	14 23 45.33	+46 50 57.3	[VV2006] J142345.3+465057		J142345.33+465057.3	142345+465100	J142344.1+465108	0.553
QSO	BROADLINE	14 00 03.08	+39 10 55.2	[VV98] J140003.1+391056		J140003.07+391055.1	140003+391053	J140003.3+391042	0.802
QSO	BROADLINE	14 17 40.44	+38 18 21.1	[VV2000] J141740.4+381821	BZQJ1417+3818	J141740.44+381821.0	141740+381821	J141739.4+381825	0.449
QSO	BROADLINE	12 25 06.50	+48 34 35.2	[VV2006] J122506.5+483435	BZQJ1225+4834	J122506.50+483435.1	122506+483436	J122506.8+483435	0.646
QSO	BROADLINE	11 19 16.13	+11 01 07.2	2MASS J11191611+1101069		J111916.12+110107.1	111916+110106	J111916.6+110117	0.392
QSO	BROADLINE	11 21 29.76	+12 36 17.4	4C 12.40		J112129.75+123617.4	112129+123620	J112131.3+123613	0.682
QSO	BROADLINE	14 35 52.26	+47 24 06.8	[VV2010] J143552.2+472407		J143552.24+472406.7	143552+472406	J143553.4+472416	0.808
QSO	BROADLINE	14 43 18.56	+47 25 56.7	87GB 144132.7+473904		J144318.55+472556.7	144318+472556	J144319.8+472541	0.703
QSO	BROADLINE	11 11 18.54	+15 30 33.1	[VV2010] J111118.5+153033		J111118.52+153033.0	111118+153030	J111119.2+153050	0.525
QSO	BROADLINE	11 46 54.29	+32 36 52.3	[VV2010] J114654.3+323652		J114654.28+323652.3	114654+323652	J114654.0+323653	0.464
QSO	BROADLINE	11 57 00.59	+32 44 57.9	7C 1154+3301		J115700.60+324457.8	115700+324458	J115700.8+324517	0.486
QSO	BROADLINE	13 20 41.30	+35 16 09.5	SDSS J132041.30+351609.4		J132041.30+351609.4	132041+351609	J132041.0+351604	0.575
QSO	BROADLINE	10 36 32.98	+22 03 12.2	[VV96] J103633.0+220312	BZQJ1036+2203	J103632.97+220312.2	103633+220312	J103633.1+220316	0.595
QSO	BROADLINE	09 53 59.22	+17 20 56.6	87GB 095113.8+173522	BZQJ0953+1720	J095359.23+172056.6	095359+172057	J095358.8+172049	0.712
QSO	BROADLINE	12 43 57.65	+16 22 53.4	3C 275.1		J124357.64+162253.4	124357+162252	J124357.7+162253	0.555
QSO	BROADLINE	09 56 49.88	+25 15 16.0	ICRF J095649.8+251516	BZQJ0956+2515	J095649.87+251516.0	095649+251515	J095649.9+251508	0.707
QSO	BROADLINE	12 57 57.23	+32 29 29.3	5C 12.76	BZQJ1257+3229	J125757.23+322929.2	125757+322929	J125756.7+322947	0.805
QSO	BROADLINE	13 32 45.24	+47 22 22.7	[VV2006] J133245.3+472221	BZQJ1332+4722	J133245.24+472222.6	133245+472222	J133243.8+472213	0.668
QSO	BROADLINE	14 37 48.58	+24 39 05.9	4C 24.32B		J143748.57+243905.9	143748+243907	J143749.1+243910	1.001
QSO	BROADLINE	09 38 57.18	+42 48 29.3	QSO B0935+430		J093857.17+424829.3	093857+424830	J093858.3+424826	2.049
QSO	BROADLINE	14 19 46.61	+38 21 48.4	QSO B1417+385	BZQJ1419+3821	J141946.60+382148.4	141946+382148	J141946.2+382201	1.832
QSO	BROADLINE	11 18 57.30	+12 34 41.7	[V2003b] QSO J1118+1234 abs 1.9768	BZQJ1118+1234	J111857.30+123441.7	111857+123442	J111857.7+123433	2.125
QSO		14 01 50.38	+33 39 54.0	87GB 135942.7+335424		J140150.37+333954.0	140150+333953	J140150.5+334006	1.634
QSO	BROADLINE	12 51 02.67	+38 45 07.3	87GB 124842.1+390130		J125102.67+384507.3	125102+384506	J125102.5+384523	1.505
QSO	BROADLINE	12 28 47.43	+37 06 12.1	[VV98] J122847.5+370612	BZQJ1228+3706	J122847.42+370612.0	122847+370612	J122847.1+370615	1.516
QSO	BROADLINE	11 46 36.76	+32 00 04.1	87GB 114400.9+321630		J114636.75+320004.1	114636+320003	J114636.0+320000	1.757
QSO	BROADLINE	12 58 29.75	+35 28 43.6	5C 12.89		J125829.75+352843.6	125829+352841	J125828.3+352846	1.885
QSO	BROADLINE	11 30 53.28	+38 15 18.7	QSO J1130+3815	BZQJ1130+3815	J113053.28+381518.6	113053+381519	J113052.7+381530	1.740
QSO	BROADLINE	13 10 59.40	+32 33 34.4	[VV96] J131059.2+323336	BZQJ1310+3233	J131059.40+323334.3	131059+323334	J131059.8+323336	1.639
QSO	BROADLINE	12 06 37.05	+39 41 03.8	QSO B1204+399		J120637.04+394103.7	120637+394104	J120637.1+394118	1.517
QSO	BROADLINE	12 49 18.42	+28 17 43.6	[VV2000] J124918.4+281743		J124918.41+281743.6	124918+281744	J124917.6+281753	1.706
QSO	BROADLINE	10 35 16.52	+26 15 17.3	SDSS J103516.52+261517.3		J103516.52+261517.3	103516+261517	J103515.0+261529	1.607
QSO	BROADLINE	12 35 05.81	+36 21 19.3	[VV98] J123505.8+362119	BZQJ1235+3621	J123505.80+362119.3	123505+362120	J123506.3+362101	1.599
QSO	BROADLINE	13 25 47.68	+34 13 20.7	[VV2006] J132547.7+341321		J132547.67+341320.6	132547+341318	J132549.6+341324	1.938
QSO	BROADLINE	14 46 42.37	+14 28 01.4	SDSS J144642.37+142801.4		J144642.37+142801.4	144642+142801	J144641.3+142753	1.977
QSO	BROADLINE	09 03 03.99	+46 51 04.2	4C 47.29	BZQJ0903+4651	J090303.98+465104.1	090304+465104	J090304.4+465059	1.465
QSO	BROADLINE	13 47 23.49	+18 35 37.6	87GB 134500.4+185002	BZQJ1347+1835	J134723.49+183537.5	134723+183538	J134724.1+183556	2.178
QSO	BROADLINE	13 27 00.86	+22 10 50.2	QSO J1327+2210	BZQJ1327+2210	J132700.86+221050.1	132700+221050	J132700.4+221048	1.397
QSO	BROADLINE	12 07 27.90	+27 54 58.9	7C 1204+2811	BZQJ1207+2754	J120727.90+275458.8	120727+275459	J120728.3+275507	2.180
QSO	BROADLINE	13 38 57.16	+43 02 35.1	NVSS J133857+430235		J133857.15+430235.0	133857+430235	J133857.0+430243	1.576
QSO	BROADLINE	11 26 57.66	+45 16 06.3	[VV96] J112657.6+451605	BZQJ1126+4516	J112657.65+451606.3	112657+451607	J112656.3+451617	1.813
QSO	BROADLINE	10 04 12.86	+46 26 22.6	[VV2006] J100412.8+462622	BZQJ1004+4626	J100412.86+462622.6	100412+462622	J100414.4+462626	2.074
QSO	BROADLINE	10 27 13.08	+48 03 13.5	[VV2006] J102713.1+480313	BZQJ1027+4803	J102713.08+480313.5	102713+480313	J102713.4+480306	1.285
QSO	BROADLINE	10 08 21.58	+44 00 16.5	[VV2006] J100821.6+440016	BZQJ1008+4400	J100821.57+440016.5	100821+440016	J100822.3+440024	1.185
QSO		14 20 20.69	+46 24 40.9	[VV2006] J142020.7+462440	BZQJ1420+4624	J142020.68+462440.9	142020+462441	J142019.9+462443	1.246
QSO	BROADLINE	13 45 23.83	+41 25 41.6	[VV2006] J134523.8+412541	BZUJ1345+4125	J134523.83+412541.5	134523+412541	J134524.2+412539	0.916
QSO	BROADLINE	12 26 07.92	+47 37 00.6	[VV2006] J122607.9+473700		J122607.92+473700.5	122607+473700	J122608.9+473636	1.054
QSO		12 33 54.46	+48 20 50.0	[VV98] J123354.4+482050		J123354.45+482049.9	123354+482052	J123353.8+482104	0.996
QSO	BROADLINE	12 52 48.29	+47 40 43.7	[VV2006] J125248.3+474044		J125248.28+474043.7	125248+474042	J125247.3+474027	0.921
QSO	BROADLINE	12 54 36.96	+42 16 44.2	[VV2006] J125437.0+421643		J125436.96+421644.2	125436+421646	J125436.6+421635	0.913
QSO	BROADLINE	13 08 51.34	+47 29 55.0	[VV2006] J130851.3+472955	BZQJ1308+4729	J130851.33+472954.9	130851+472954	J130853.4+472942	0.885
QSO		13 17 06.02	+46 50 34.9	[VV2010] J131706.1+465035		J131706.02+465034.9	131706+465033	J131705.4+465019	1.022
QSO	BROADLINE	10 51 44.88	+12 58 28.9	[VV2010] J105144.9+125829		J105144.87+125828.9	105144+125829	J105145.2+125816	1.314
QSO	BROADLINE	13 00 20.93	+14 17 18.6	ICRF J130020.9+141718	BZQJ1300+1417	J130020.92+141718.5	130020+141717	J130022.3+141712	1.107
QSO	BROADLINE	10 06 07.70	+32 36 26.2	7C 1003+3251		J100607.70+323626.1	100607+323627	J100607.0+323632	1.025
QSO	BROADLINE	12 26 41.95	+40 26 33.2	[VV2010] J122641.9+402632		J122641.95+402633.2	122641+402634	J122641.6+402647	1.299
QSO	BROADLINE	12 39 15.00	+40 49 55.5	[VV2000] J123915.0+404955		J123915.00+404955.4	123915+404956	J123914.5+404956	1.314
QSO	BROADLINE	12 59 26.74	+33 33 39.4	[VV2010] J125926.8+333339		J125926.73+333339.3	125926+333337	J125927.6+333333	1.062
QSO	BROADLINE	13 42 54.38	+28 28 05.9	QSO B1340+2843		J134254.38+282805.8	134254+282808	J134255.8+282805	1.035
QSO	BROADLINE	12 40 21.14	+35 02 58.8	7C 1237+3519		J124021.14+350258.7	124021+350259	J124020.3+350303	1.198
QSO	BROADLINE	13 17 36.50	+34 25 15.9	7C 1315+3441	BZQJ1317+3425	J131736.50+342515.9	131736+342516	J131736.3+342519	1.054
QSO	BROADLINE	10 39 41.95	+24 22 40.8	7C 1036+2438		J103941.95+242240.8	103941+242239	J103940.5+242236	1.173
QSO	BROADLINE	10 51 48.79	+21 19 52.3	4C 21.28	BZQJ1051+2119	J105148.79+211952.3	105148+211952	J105148.3+211955	1.300
QSO	BROADLINE	09 51 45.70	+17 36 22.8	SDSS J095145.68+173622.7		J095145.69+173622.7	095145+173621	J095145.2+173612	0.895
QSO	BROADLINE	13 52 05.18	+18 53 35.5	2MASS J13520517+1853352		J135205.18+185335.4	135205+185335	J135204.9+185331	0.897
QSO	BROADLINE	14 46 35.35	+17 21 07.6	ICRF J144635.3+172107	BZQJ1446+1721	J144635.35+172107.5	144635+172107	J144633.9+172114	1.024
QSO	BROADLINE	09 45 38.11	+35 34 55.1	9C J0945+3534		J094538.11+353455.0	094538+353455	J094538.6+353502	1.127
QSO	BROADLINE	13 02 17.18	+48 19 17.6	[VV98] J130217.2+481918	BZQJ1302+4819	J130217.18+481917.5	130217+481917	J130217.5+481928	0.874
QSO	BROADLINE	10 18 10.97	+35 42 39.5	7C 1015+3557	BZQJ1018+3542	J101810.96+354239.4	101811+354240	J101810.5+354233	1.229
QSO	BROADLINE	09 25 51.84	+36 12 35.6	NVSS J092551+361235		J092551.84+361235.6	092551+361235	J092552.0+361241	0.998
QSO	BROADLINE	09 48 55.34	+40 39 44.6	4C 40.24	BZQJ0948+4039	J094855.34+403944.6	094855+403944	J094856.5+403959	1.250
QSO	BROADLINE	09 16 48.91	+38 54 28.2	4C 38.28	BZQJ0916+3854	J091648.91+385428.1	091648+385428	J091648.1+385456	1.267
QSO		10 24 59.86	+17 21 47.4	NVSS J102459+172145		J102459.85+172147.4	102459+172145	J102500.9+172145	0.926
QSO	BROADLINE	12 52 49.87	+11 29 33.1	2E 2881		J125249.87+112933.1	125249+112934	J125249.6+112915	0.874
QSO		09 30 40.06	+19 36 53.7	SDSS J093039.07+193652.5*		J093040.05+193653.7	093040+193652	J093038.9+193646	1.165
QSO		09 15 48.10	+25 08 59.0	RX J0915.8+2509		J091548.09+250858.9	091548+250858	J091547.9+250927	1.043
QSO	BROADLINE	12 15 03.98	+16 54 38.1	2FGL J1214.8+1653	BZQJ1215+1654	J121503.98+165438.0	121503+165438	J121504.1+165422	1.131
QSO	BROADLINE	13 42 08.38	+27 09 30.6	7C 1339+2724	BZQJ1342+2709	J134208.37+270930.5	134208+270930	J134208.5+270941	1.188
QSO	BROADLINE	13 36 02.83	+27 27 51.7	QSO B1333.7+2743		J133602.83+272751.6	133602+272752	J133601.8+272747	1.119
QSO	BROADLINE	11 53 18.07	+23 41 13.5	1RXS J115318.2+234121*		J115318.07+234113.5	115318+234112	J115318.2+234121	0.990
QSO	BROADLINE	12 46 00.00	+43 46 26.9	[VV2006] J124600.0+434626	BZQJ1245+4346	J124600.00+434626.9	124559+434627	J124601.9+434631	1.151

Table 3.5: List of sources present in the initial sample: Class, Subclass and z columns are assigned by the SDSS's team.

* These sources were detected at 13.93 and 8.22 arcsec, respectively from top to bottom

CHAPTER 4

RESULTS

In this study we aim at comparing the physical properties of known blazars with those of blazar candidates, selected from the comparison of radio and X-ray observations. We therefore need to estimate the power of the AGN central engines and to test whether confirmed blazars and blazar candidates are comparable.

In order to compute the accretion rates $\lambda_{\rm Edd}$ (Sec.2.1.1) it is necessary to own the values of $L_{\rm bol}$ and $L_{\rm Edd}$ (Eq.2.3). Both can be inferred from the optical spectra, the former needing measurements only on the continuum while the latter requiring them also from the emission lines.

4.1 Redshift Subdivision

Measuring the properties of AGN central engines relies on different techniques, depending on the spectral features that can be accessed with the observations. Since the observed spectral ranges are determined by the sources' redshifts, we had to subdivide our sample in several groups of spectra and to apply the proper approach for the measurements available in each set.

Using the relation $\lambda_{\rm observed} = \lambda_{\rm emitted}(1+z)$ the sample was divided into three groups based on the spectral range covered by the spectrographs, each of one containing the following emission lines in the laboratory rest frame:

1. Hβ and MgII (hereafter Hβ×MgII)
2. MgII (hereafter MgII)
3. MgII and CIV (hereafter MgII×CIV)

Beacuse the BOSS and SEGUE spectrographs cover the EM spectrum in the range $\sim$ 3000–10000Å the Hβ λ4861 and MgII λ2798 emission lines were observed for

$z \sim 0.4$–1.1, being the first value of z referred to the object closest to the laboratory frame. At higher redshifts the only line detected was MgII λ2798, up to $z \sim 1.3$ where the CIV λ1549 has began to be observed.

The redshift subdivision was done using the SQL language, asking for the list of the entire sample, and for a z ordering from lower to higher values (appendix, listing 14).

4.2 Luminosities

The first type of luminosity which has to be calculated is the monochromatic luminosity $L(\lambda) \equiv L_\lambda$, which will be used in order to compute both the bolometric luminosity and the BLR sizes. L_λ basically should be related to the flux density by the following equation:

$$L_\lambda = 4\pi d^2 F_\lambda \ \left[\ \mathrm{erg\ s^{-1} \AA^{-1}} \ \right] \tag{4.1}$$

This relation holds for objects which are not too far from the observer, at distances less than 4000 Mpc. For distant sources the metric of space-time is described by the solution of Einstein's field equations of general relativity, given by the so-called Robertson-Walker (RW) metric. In cosmology the luminosities are expressed as:

$$\boxed{L_\lambda = 4\pi d_L^2 F_\lambda} \tag{4.2}$$

where d_L is the *luminosity distance*. Following Peebles (1993), computing d_L requires to set the physical parameters governing the model of universe used. In this work we assume $\mathrm{H_0} = 70$ km $\mathrm{s^{-1} Mpc^{-1}}$, $\Omega_\mathrm{m} = 0.30$ and $\Omega_\Lambda = 0.70$.

The first step is to evaluate the total line-of-sight comoving distance

$$D_\mathrm{C} = D_\mathrm{H} \int_0^z \frac{\mathrm{d}z'}{E\left(z'\right)} \tag{4.3}$$

being $\mathrm{D_H} = c/\mathrm{H_0}$ the Hubble distance and

$$E\left(z'\right) = \sqrt{\Omega_\mathrm{m}\left(1+z\right)^3 + \Omega_\mathrm{R}\left(1+z\right)^2 + \Omega_\Lambda} \tag{4.4}$$

a predefined function with $\Omega_\mathrm{R} = 1 - \Omega_\mathrm{m} - \Omega_\Lambda$ a parameter setting the "curvature of space", equal to zero in this case. The second step is to evaluate the transverse comoving distance $\mathrm{D_M}$ which, if $\Omega_\mathrm{R} = 0$, becomes equal to $\mathrm{D_C}$. Finally, because

$d_{\mathrm{L}} = (1+z)\mathrm{D_M}$ and $\mathrm{D_M} \equiv \mathrm{D_C}$, the final formula is:

$$\begin{aligned} d_{\mathrm{L}} &= (1+z)\,\mathrm{D_H} \int_0^z \frac{\mathrm{d}z'}{E\,(z')} \\ \Rightarrow d_L &= (1+z)\,\mathrm{D_H} \int_0^z \frac{\mathrm{d}z'}{\sqrt{\Omega_{\mathrm{m}}\,(1+z)^3 + \Omega_\Lambda}} \end{aligned} \tag{4.5}$$

The luminosity distance d_{L} was evaluated with the use of a script (appendix, listing 7) pointing to a program written in the C++ language (appendix, listing 1).

F_λ, which is the other value that has to be obtained in order to evaluate L_λ, is the flux density, which was measured directly on the spectra.

The spectra were opened with IRAF's `splot` task, and depending on what group was involved, the flux densities evaluted at 5100Å and 3000Å for Hβ×MgII, at 3000Å for MgII, at 3000Å and 1450Å for MgII×CIV. The measurements were taken by evaluating the average flux density, the r.m.s. and the s/n ratio on 100Å wide continuum bands, centered on the chosen wavelength. Using IRAF's `splot` task, these values are written in an output file (splot.log), according to the format:

```
Jun 25 16:41 [0831-52294-0620dd.fits]:
avg:        4.28   rms:       0.2702   snr:      15.84
```

Having computed d_{L} and measured the F_λ, the luminosities were obtained using the following calculations:

$$\begin{aligned} \lambda L_\lambda &= \lambda 4\pi d_{\mathrm{L}}^2 F_\lambda \\ &= 4\pi \left(\underbrace{3.0857 \cdot 10^{24}}_{\text{Mpc} \longrightarrow \text{cm}} \right)^2 d_{\mathrm{L}}^2 \cdot \lambda \left(\underbrace{\underbrace{10^{-17}}_{\text{SDSS's } F_\lambda \text{ normalization}}} \right) F_\lambda \\ &= 4\pi \cdot \overbrace{3.0857^2 \cdot 10^{48}} \cdot 10^{-17} \cdot d_{\mathrm{L}}^2 \cdot \lambda F_\lambda \\ \Rightarrow \log_{10} \lambda L_\lambda &= 33.078 + 2 \cdot \log_{10} d_{\mathrm{L}} + \log_{10} \lambda + \log_{10} F_\lambda \end{aligned} \tag{4.6}$$

The errors were evaluated following the error propagation theory:

$$\sigma = \sqrt{\sum_i \left(\frac{\partial \mathrm{F}}{\partial x_i} \right)^2 \sigma_{x_i}^2} \tag{4.7}$$

This turns into:

$$\sigma_{\log_{10} \lambda L_\lambda} = \frac{1}{10 \ln F_\lambda} \sigma_{F_\lambda} \tag{4.8}$$

with σ_{F_λ} correspondig to the rms measured on the spectrum.

Å	$f(\lambda)$	$\sigma_{f(\lambda)}$
5100	8.1	0.4
3000	5.2	0.2
1450	4.2	0.1

Table 4.1: Correction factors based on Runnoe et al. (2012).

4.2.1 Bolometric Luminosities

The bolometric luminosity in the numerator of Eq.2.3 is the energy radiated by a source over the entire EM spectrum. The luminosities measured in Sec.4.2 belong to a little interval of the entire SED and so a correction must be applied in order to take in account the photons of all wavelengths:

$$L_{\rm bol} = f\left(\lambda\right) \lambda L_{\lambda} \ \left[\ {\rm erg \ s^{-1}} \ \right] \tag{4.9}$$

The most common values of $f(\lambda)$ are ∼10 for 5100 Å, ∼5 for 3000 Å and ∼4.4 for 1450 Å. Because of the sample's wide range of z (∼0.5–2.5) the λ at 5100Å was not always present in the optical spectra, shifting to longer wavelengths (IR) already in the Hβ×MgII sample, the closest to the laboratory rest frame. There were two possibilities: extrapolating L_{5100} by fitting the spectral continua with powerlaws or finding a good prescription for the bolometric corrections of all the L_{λ} in order to trust the one involving L_{3000}, which was present in the entire sample. At the beginning the first method was used, obtaining reasonable results where the luminosities were covering a range of $L_{\lambda} \sim 10^{44}$–10^{45} erg s^{-1}. The $L_{\rm bol}$ values were discording in the UV part of the spectra, where the ones inferred from L_{1450} or the extrapolated L_{5100} differed significantly from the ones computed with the use of the most common L_{3000} prescriptions. After various tests based on articles retrieved from literature (i.e. Nemmen and Brotherton, 2010), the bolometric correction factors that permitted to have the most homogeneus values of $L_{\rm bol}$ over the entire sample were the ones listed in table 4.1 (Runnoe et al., 2012).

The computations of the bolometric luminosities were done using Eq.4.6, while the errors were evaluated with Eq.4.7, executing the SQL code reported in appendix (listing 15). A linear regression was done too, using the Bivariate, Correlated Errors and intrinsic Scatter (BCES) method (Akritas and Bershady, 1996) and a Python script[1] (appendix, listing 9). Finally, the Pearson's R and the *2-tailed p-value* were calculated using Python's *scipy.stats.pearsonr* module. The comparison of the two methods is reported in table 4.2 and represented in Fig.4.1.

[1] `https://github.com/rsnemmen/BCES`

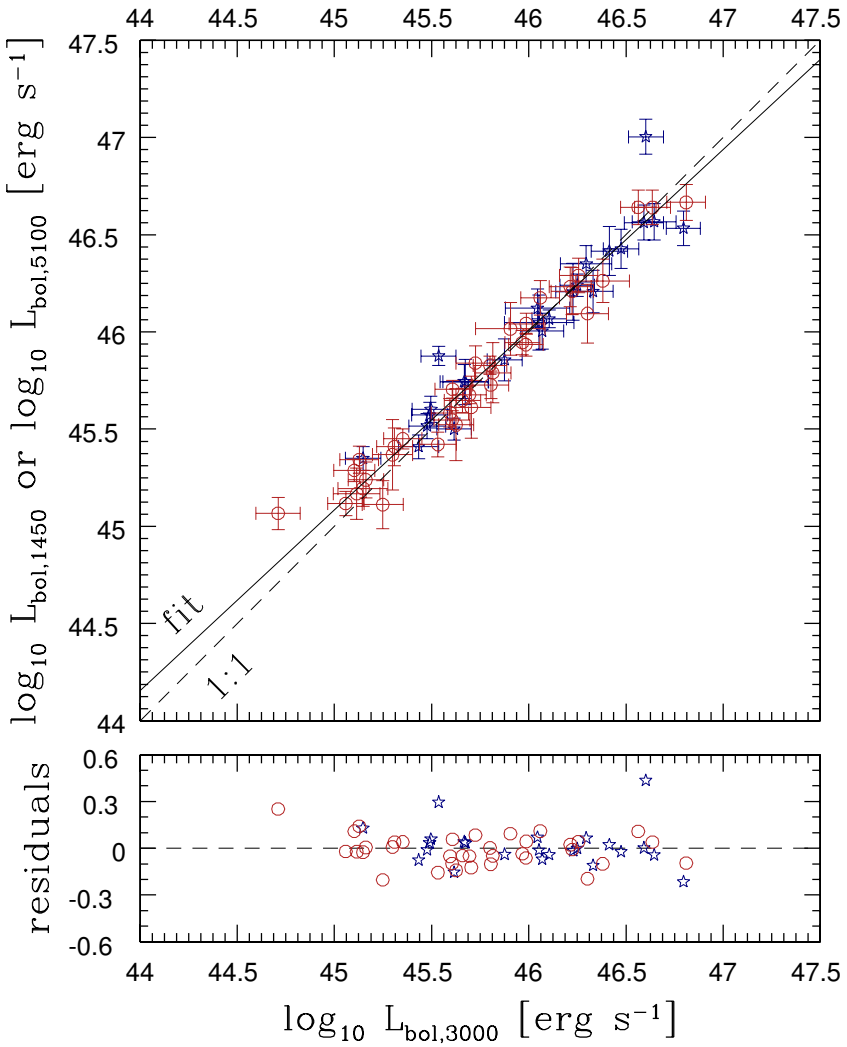

Figure 4.1: Linear fit of the bolometric luminosities evaluated from L_{5100},L_{3000}, and L_{1450}. The data points come from sources belonging to the Hβ×MgII and MgII×CIV groups. Blue stars correspond to BZQs while red circles to sources identified as QSOs by the SDSS team.

	slope	**intercept**
BCES Bisector	0.927 ± 0.047	3.362 ± 2.130
bootstrap	0.928 ± 0.043	3.331 ± 1.966
Pearson's R	0.970	
2-tailed p-value	$1.667 \cdot 10^{-37}$	

Table 4.2: BCES bisector values for λ5100 and λ1450 versus λ3000 bolometric corrections.

4.3 Masses

In AGNs the BH masses $M_\bullet$ can be estimated by *single-epoch* or *virial* methods. They rely on the results of reverberation-mapping (RM) experiments (Blandford and McKee, 1982; Peterson, 1993) which provide empirical relations between the emissivity-weighted radius of the BLR and the source luminosity L, as stated in Sec.1.2.3 also for the case of the NLR.

The $R_{\rm BLR}$–L relations are parametrized as $R_{\rm BLR} \propto (\lambda L_\lambda)^\alpha$. Assuming that the gas motion of the BLR is virialized, the single-epoch $M_\bullet$ estimators take the general form:

$$\boxed{M_\bullet = f G^{-1} (\lambda L_\lambda)^\alpha V_{\rm BLR}^2} \tag{4.10}$$

where $V_{\rm BLR}$ is a probe of the BLR velocity field and f is a factor that depends on the geometrical distribution of the observed BLR gas.

A common $M_\bullet$ estimator is the "Hβ method" where $R_{\rm BLR}$ is estimated from λL_λ at 5100Å while $V_{\rm BLR}$ from the FWHM of the Hβ emission line (Bentz et al., 2009; Kaspi et al., 2000). Another method is based on the MgII λ2798 line and L_{3000}. For this wavelength and emission line dedicated RM campaings were done (Clavel et al., 1991; Metzroth et al., 2006), followed by $R_{\rm BLR}$–L_{3000} calibrations (McLure and Dunlop, 2004). In the UV band it should be possible to use another estimator, the L_{1450} luminosity in combination with the CIV λ1549 emission line, having $R_{\rm BLR}$(CIV) been inferred from RM experiments (Kaspi et al., 2007). Several studies demonstrated that this estimator is affected by numerous biases. In particular, there is evidence of blue-shifts of the CIV emission line with respect to the rest frame of the AGN, and that the FWHM is often smaller than the Hβ's one, facts indicating that the dynamics of the CIV-emitting gas may be dominated by non-virial motion (Baskin and Laor, 2005).

The widths of the emission lines were measured starting from the closest group of spectra (Hβ×MgII) to the farthest (MgII×CIV). The FWHM measurements on the Hβ λ4861 were done in two steps: at first, the narrow components belonging to the NLR (such as [OIII] λλ4959,5007, and also a narrow component residing into the Hβ λ4861) were subtracted from the spectra. Finally, the FWHM were estimated both on the original spectra and on the narrow line-subtracted ones, comparing the two results with the widths of the MgII λ2798 in order to see if there were any correlations between the various values obtained.

In order to subtract the narrow components we performed Gaussian fits to the relevant lines. Since the narrow Hβ line component should originate in a similar region to the well isolated [O III] λλ4959,5007 emission lines, we used the latter to estimate the initial guess to the hidden profile of the former.

The fitting task used was STSDAS's *ngaussfit*, which permits to fit, in a row,

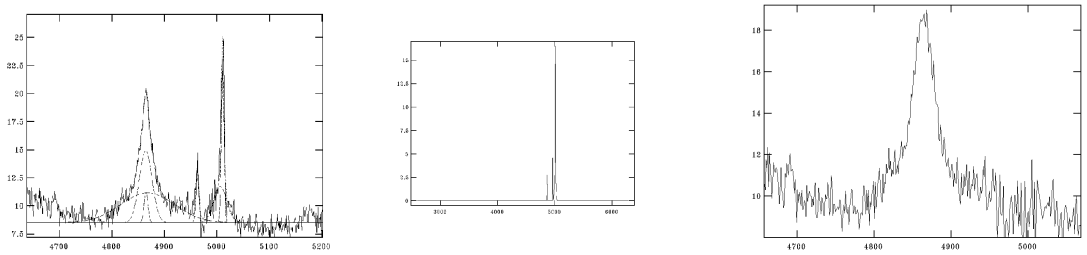

Figure 4.2: Hβ narrow component subtraction: Gaussian fitting procedure (*left*), artificial narrow emission lines spectrum (*center*) and the final spectrum without the narrow components (*right*).

many Gaussians on a spectrum. Its output file, which has a *.tab* extension, contains the values of the amplitude, the center and the width of every single Gaussian fitted. Moreover, the χ^2 residual value of the fit, in addition to the slope and the intensity of the continuum over the region where the sample points were chosen, is printed too.

The intention is, given a set of initial guesses for the slope and intercept of the local continuum laying under the wavelengths of interest, to start a procedure able to reproduce the profiles of the lines, minimizing the residuals given by the combination of the Gaussians fitted. This is done by subsequent iterations, at first interpolating the narrower ones and at last, after having parametrized them, by searching the best fitting values for the broader components minimizing the χ^2 on the spectral range under exam.

The fitting procedure, in most of the cases, started assuming that there were 6 Gaussians: two for [OIII] λ5007 (one broader and fainter than the prominent narrow line core), one for [OIII] λ4959 (narrow) and three for Hβ λ4861 (two broad components and a narrow one).

At the beginning the widths of the Gaussians belonging to the oxygen lines were set to low values ($\lesssim$5–10Å) while their intensity parameters were left variable, having fixed all values concerning the Gaussians on the Hβ line. As these lines became visually well fitted and centered on the correct wavelengths, the values of all Gaussians were fixed except for the intensities, and another fitting iteration was launched. At this point, the oxygen group was well fitted and all its parameters were fixed, focusing the fitting procedure on the Hβ group.

At first the narrow component was fixed in order to let the broad ones vary their widths, intensities and positions. Once having fast fitted the broad components the narrow one was set as variable, and the fitting procedure repeated on the Hβ group once more. A last fit was done leaving all the parameters free except for the components of the continuum.

Finally, when all the Gaussians were well fitting the emission lines, the pa-

rameters concerning the broad emission components were fixed to zero and the task quitted, producing an output file containing only the values of the narrow components that had to be subtracted. A typical result is illustrated in Fig.4.2.

The outputs had to be converted into FITS format in order to be readable from IRAF as spectra. This passage was done using STSDAS's *function* task, which requires as input the FITS file where the Gaussian interpolation was done, the name of the tab file generated by ngaussfit, and a filename for the output (the artificial spectrum, Fig.4.2). This step was done launching a CL script (appendix, listing 8).

The last step, which was done taking advantage of the splot task capabilities, was the subtraction of the artificial spectra from the original ones. Once having plotted an original FITS file, pressing the "f" key lets the user enter the function mode where it is possible to do arithmetics using other images. For each spectrum a subtraction was chosen by hitting the "-" key, and the artificial spectrum selected as image to be subtracted from the plotted one. Finally, a name for the output (FITS) file was given when asked to.

The FWHM were measured in two steps using the splot task: continuum subtraction and width measurement.

The first passage can be done pressing the "t" key and asking for a subtraction of the continuum (with the "-" key) when the menu prompts. Once in fitting mode it is possible to select which points are to be taken as sample for the operation to be done, as well as the order of the function used to reproduce the continuum. For those cases where a strong contamination from FeII multiplets or broad HeII emission led to an overestimate of the continuum, we excluded the corresponding spectral ranges from the calculations, keeping the continuum intensity as low as possible. When the fit was satisfying, the procedure was quitted hitting "q".

The FWHM measurements were taken converting the spectral ranges centered on each emission line in velocity scale. Here, by applying a Gaussian interpolation to the line profiles, we extracted the FWHM of the emission lines into plain text log files. They were reported to a CSV file which was uploaded to the CasJobs's SQL personal database afterwards. Each FWHM was measured three times in order to have a minimal sample capable to be used to calculate the measurement error on the values obtained. The errors on the FWHM were estimated as the semidifference between the higher and the lower values measured.

With the aim to test if there was any correlation between the FWHM of Hβ and MgII, and after having tested various prescriptions for the evaluation of the BRL size (Kaspi et al., 2005), a recent paper has been taken in account (Trakhtenbrot and Netzer, 2012). In this work it is stated that that for relatively narrow MgII lines (FWHM $\lesssim$ 4000 km s^{-1}), where the profile can be treated as a doublet, the

Hβ×MgII			MgII		MgII×CIV	
Hβ WHOLE [km s^{-1}]	Hβ DENARROWED [km s^{-1}]	MgII [km s^{-1}]	MgII [km s^{-1}]	MgII [km s^{-1}]	CIV [km s^{-1}]	
5457 ±1116	5699 ±553	5669 ±2503	8674±2779	8454±1285	7763±2207	6209±420
10902±2614	11736±2069	8713±1363	4102±1942	8106±1636	4217±615	4255±770
4256 ±2314	8310 ±778	4866 ±941	12981±1997	7690±1217	3229±385	5636±1464
6363 ±833	7100 ±1263	7932±1289	6110±1184	5014±1124	8444±1915	10305±2836
8529 ±1483	10257±1732	9970±1290	8918±1743	5564±2289	7279±2387	4462±955
4056 ±819	3448 ±490	5285 ±867	8613±1543	7442±1256	2034±357	3253±194
10773±2525	12408±746	9014 ±1874	7460±1668	3627±724	4201±1289	4111±267
6938 ±2261	6091 ±782	6232 ±1293	9831±1776	6205±2317	1101±2256	7216±690
6113 ±782	6610 ±1046	6571±1402	8604±1827	5860±1632	6715±1447	5999±563
6852 ±1299	7364 ±898	8458 ±1147	11161±1909	5777±960	4940±1712	4139±548
2738 ±656	2540 ±462	7897 ±1515	6582±1185	8284±1071	7278±3099	6128±594
4762 ±1018	3374 ±630	4424 ±635	3895±1422	6479±1274	5009±1403	7336±1407
2951 ±1063	3131 ±443	5538 ±4421	5334±1207	8016±1530	13214±3687	8276±1178
2962 ±862	3395 ±589	4146 ±980	8768±1407	9961±874	7702 ±2160	5759±774
4535 ±862	5492 ±812	5566 ±846	4809±1121	8013±1785	3453 ±1032	5162±413
6032 ±1712	5931 ±1020	4972±595	9507±1355	11287±931	9047 ±3083	8419±1798
2921 ±531	3610 ±696	4476 ±1261	5241±1016	9394±2415	6288 ±999	6855±467
4777 ±1239	7340 ±1602	5734±1048	5025±1607	9302±1162	3616 ±816	5637±703
4387 ±1320	5497 ±1338	7352±2103	4931±1446	4604±387	10722±5142	4521±944
3412 ±673	3299 ±480	3542 ±533	9434±1627		4433 ±546	5145±509
5386 ±759	5540 ±915	5429 ±678			7835 ±3919	5631±705
4126 ±1297	4459 ±783	4217 ±976			3331 ±673	6505±700
					7371 ±1113	7010±1028

Table 4.3: Values of the FWHM measured.

	Hβ×MgII (without prescription)		Hβ×MgII (Trakhtenbrot & Netzer)	
DENARROWED				
		Log space		
BCES Bisector	0.534 ± 0.151	1.760 ± 0.559	0.567 ± 0.157	1.638 ± 0.583
bootstrap	0.514 ± 0.155	1.837 ± 0.577	0.546 ± 0.157	1.714 ± 0.587
		Linear space		
BCES Bisector	0.510 ± 0.237	2927 ± 1303	0.523 ± 0.233	2822 ± 1285
bootstrap	0.491 ± 0.204	3010 ± 1152	0.500 ± 0.203	2935 ± 1169
Pearson's R	0.82		0.83	
2-tailed p-value	$2.31 \cdot 10^{-6}$		$2.30 \cdot 10^{-6}$	
WHOLE				
		Log space		
BCES Bisector	0.556 ± 0.249	1.718 ± 0.926	0.580 ± 0.263	1.626 ± 0.977
bootstrap	0.545 ± 0.284	1.757 ± 1.049	0.567 ± 0.289	1.673 ± 1.071
		Linear space		
BCES Bisector	0.523 ± 0.375	3349 ± 1979	0.528 ± 0.378	3308 ± 2003
bootstrap	0.493 ± 0.456	3462 ± 2274	0.500 ± 0.526	3415 ± 2488
Pearson's R	0.72		0.72	
2-tailed p-value	$1.53 \cdot 10^{-4}$		$1.60 \cdot 10^{-4}$	

Table 4.4: Results of the BCES bisector linear regressions done on the FWHM belonging to the Hβ×MgII group using both the denarrowed Hβ lines and the "whole" ones, as well as with or without the precsription suggested by Trakhtenbrot and Netzer (2012).

FWHM has to be evaluated as:

$$\mathrm{FWHM}\,(\mathrm{MgII}, \mathrm{single}) = 1.01 \times \mathrm{FWHM}\,(\mathrm{MgII}, \mathrm{total}) - 304 \ \left[\ \mathrm{km\ s^{-1}}\ \right] \quad (4.11)$$

The equation improves the Pearson's R of the data points as no other prescription did before.

With the same Python script used for fitting the bolometric luminosities in Sec.4.2, many linear fits were done, both in the linear and in the logarithmic spaces. The results are listed in table 4.4 and plotted in figures 4.3 and 4.4. The best agreement, based on the highest Pearson's R and the lowest *2-tailed p* values respectively, is the one which connects denarrowed Hβ lines to MgIIs for which the widths of the narrow components were computed using Eq.4.11.

The same tests were done also on the MgII×CIV group and the results are listed in table 4.5 and illustrated in Fig.4.5.

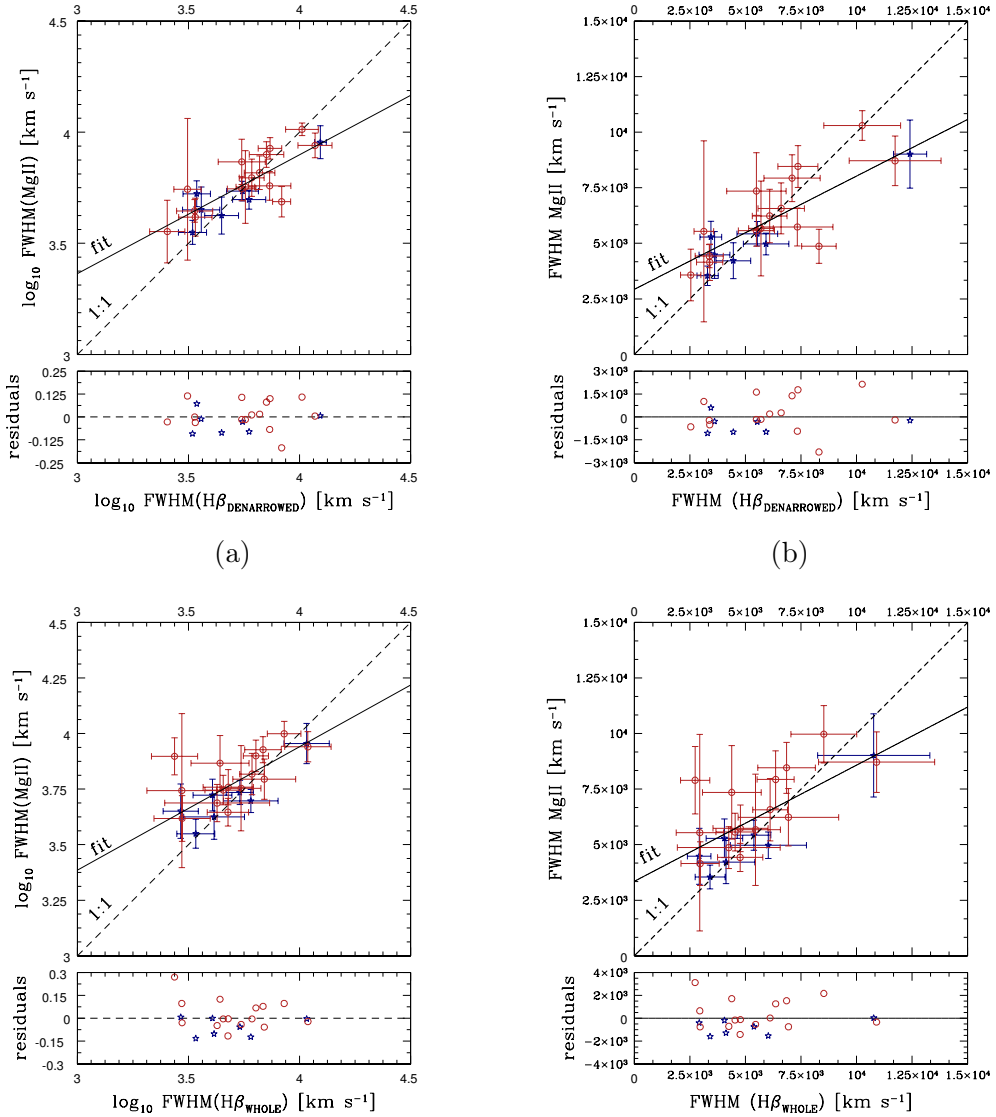

Figure 4.3: Plot of the linear BCES bisector fitting results (Tab.4.4) done on the Hβ×MgII emission lines without applying Trakhtenbrot's prescription. Blue stars correspond to known blazars while open red circles correspond to sources identified by the SDSS's team as as QSOs.

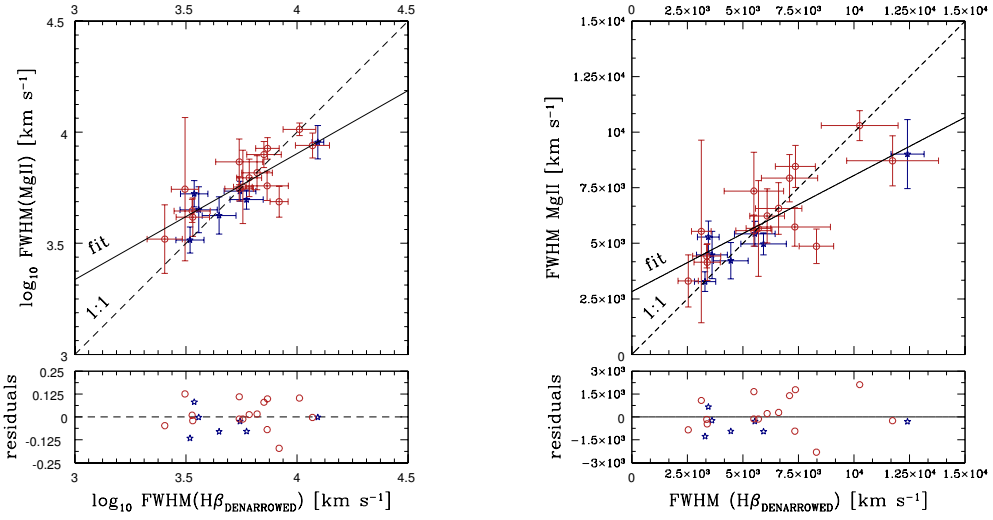

(a) (b)

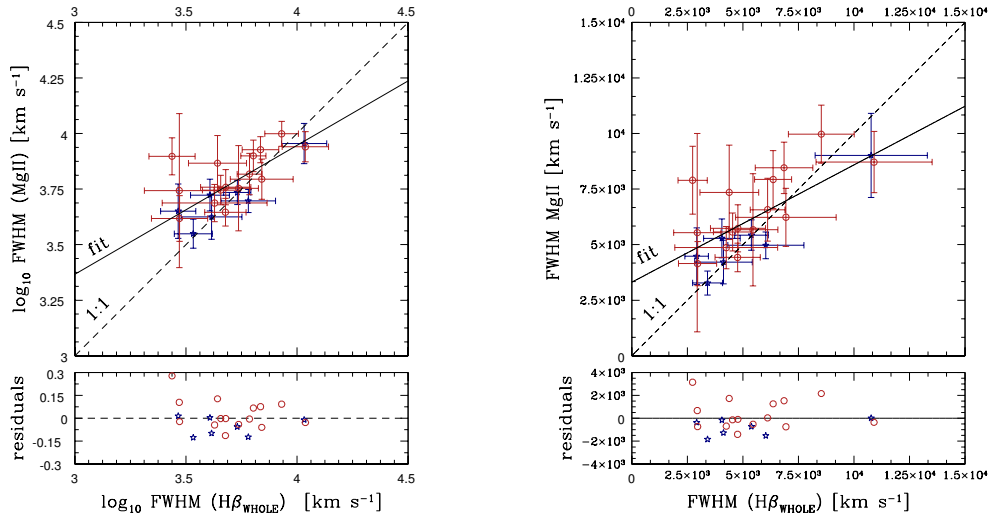

(c) (d)

Figure 4.4: Plot of the linear BCES bisector fitting results of Tab.4.4 done on the Hβ×MgII emission lines applying Trakhtenbrot's prescription. Blue stars correspond to known blazars while red circles correspond to sources identified by the SDSS's team as as QSOs.

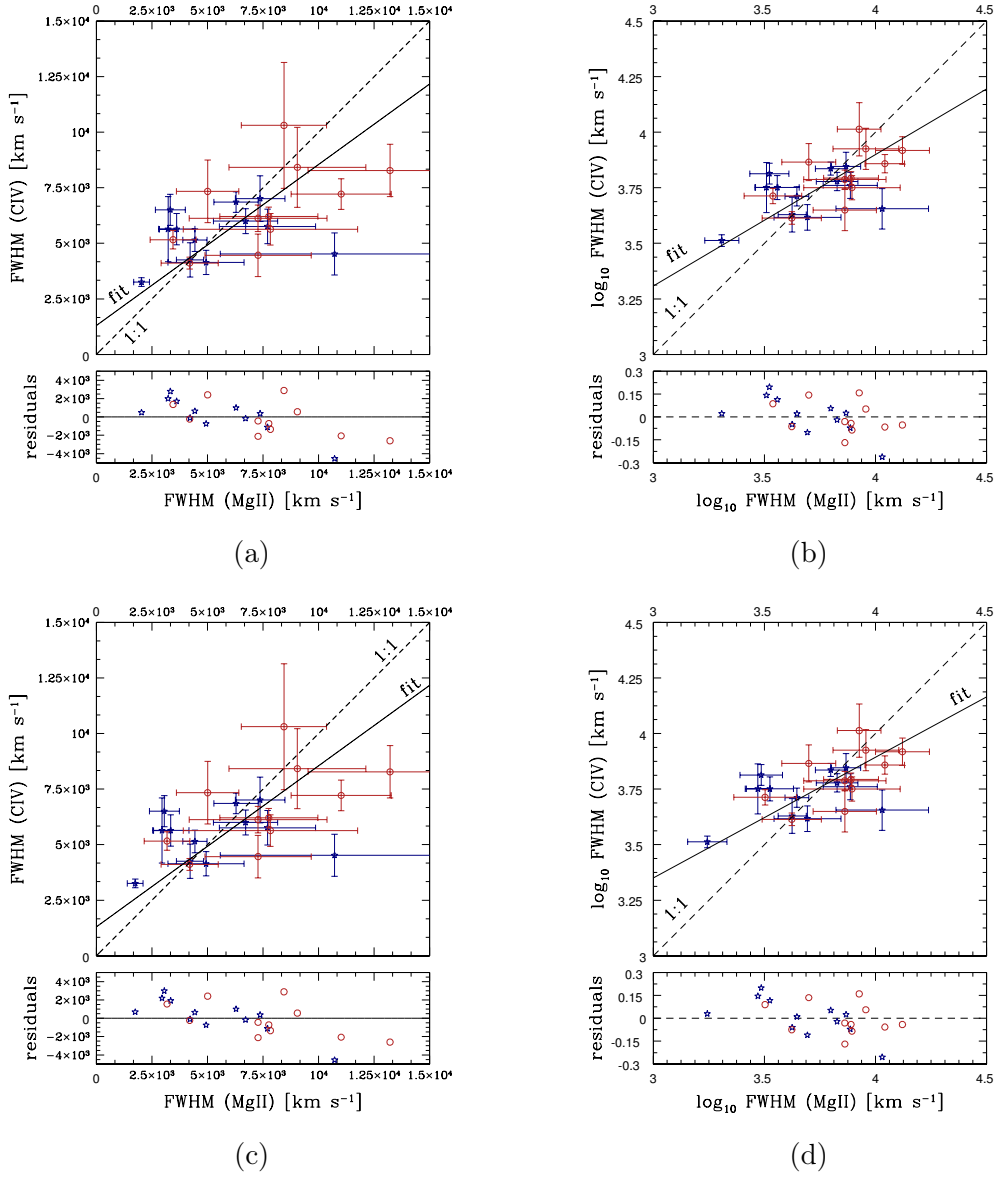

Figure 4.5: Plot of the linear BCES bisector fitting results of table 4.5 done on the MgII×CIV emission lines without applying Trakhtenbrot's prescription (*left*) or with (*right*). Blue stars correspond to known blazars while red circles correspond to sources identified by the SDSS's team as as QSOs.

MgII×CIV				
	NORMAL		NETZER'S WAY	
	Log space			
BCES Bisector	0.591 ± 0.199	1.536 ± 0.752	0.543 ± 0.202	1.723 ± 0.761
bootstrap	0.612 ± 0.176	1.454 ± 0.671	0.564 ± 0.164	1.641 ± 0.6259
	Linear space			
BCES Bisector	0.725 ± 0.483	1300 ± 3114	0.676 ± 0.466	1652 ± 2973
bootstrap	0.714 ± 0.455	1384 ± 3000	0.691 ± 0.414	1566e ± 2741
Pearson's R	0.53		0.53	
2-tailed p-value	0.01		0.01	

Table 4.5: Results of the BCES bisector linear regressions done on the FWHM belonging to the MgII×CIV group.

	$R_{\rm BLR}\,(\mathrm{H}\beta) \times R_{\rm BLR}\,(\mathrm{MgII})$		$R_{\rm BLR}\,(\mathrm{MgII}) \times R_{\rm BLR}\,(\mathrm{CIV})$	
BCES Bisector	1.14 ± 0.06	-0.28 ± 0.12	0.97 ± 0.17	1.28 ± 7.80
bootstrap	1.14 ± 0.07	-0.29 ± 0.14	0.98 ± 0.18	0.76 ± 8.46
Pearson's R	0.94		0.89	
2-tailed p-value	$2.76 \cdot 10^{-18}$		$2.04 \cdot 10^{-8}$	

Table 4.6: Results of the BCES bisector fitting on the BLR sizes.

In order to estimate the $R_{\rm BLR}$ sizes, the following relations, calibrated on a sample of 66653 SDSS AGN objets with $z \sim 0$–2 (Trakhtenbrot and Netzer, 2012), were tested:

$$R_{\rm BLR}\,(\mathrm{H}\beta) = 538.2 \left(\frac{L_{5100}}{10^{46}\ \mathrm{erg\ s^{-1}}} \right)^{0.65} \quad [\ \mathrm{lt\text{-}days}\ ] \tag{4.12a}$$

$$R_{\rm BLR}\,(\mathrm{MgII}) = 21.38 \left(\frac{L_{3000}}{10^{44}\ \mathrm{erg\ s^{-1}}} \right)^{0.62} \quad [\ \mathrm{lt\text{-}days}\ ] \tag{4.12b}$$

$$R_{\rm BLR}\,(\mathrm{CIV}) = 107.2 \left(\frac{L_{1450}}{10^{46}\ \mathrm{erg\ s^{-1}}} \right)^{0.55} \quad [\ \mathrm{lt\text{-}days}\ ] \tag{4.12c}$$

The comparisons were made between $R_{\rm BLR}(\mathrm{H}\beta)$ and $R_{\rm BLR}(\mathrm{MgII})$, and between $R_{\rm BLR}(\mathrm{MgII})$ and $R_{\rm BLR}(\mathrm{CIV})$, using the BCES method as it was already done earlier in other tests.

Because of the poor correlation between the FWHM values of the MgII and CIV emission lines (R=0.53, p=0.01) with respect to the ones of the Hβ×MgII group (R=0.83, p $\sim 10^{-4}$–10^{-6}), it was decided not to use CIV virial estimates to infer BH masses. Moreover, the prescription which permits to estimate the BLR sizes does not give the same result for different lines which are observable at the

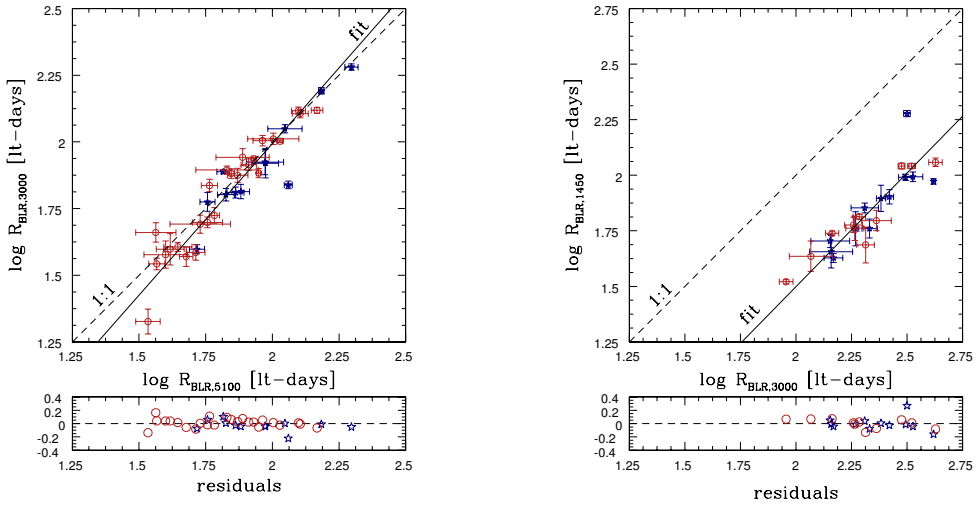

(a) (b)

Figure 4.6: BLR sizes computed with equations (4.12a) and (4.12b) for the Hβ×MgII group (a) and with equations (4.12b) and (4.12c) for the MgII×CIV one (b). As can be seen the results are not in agreement at higher redshifts when the luminosities must be taken in the far UV region of the EM spectrum.

higher redshifts ($z \gtrsim 1.3$), giving another argument against the use of this carbon emission line. Finally, because the BLR sizes on the Hβ×MgII group were in good agreement among them, as well as the FWHM, it was chosen to use $R_{\rm BLR}$(MgII) as proxy for the evaluation of the $M_\bullet$ over the entire sample, since this line is present in all groups.

4.4 Accretion Rates

The estimation of the Eddingon ratio $\lambda_{\rm Edd}$ can be done recalling Eq.2.2 of Sec.2.1.1. The luminosity was computed using Eq.4.6 while the masses through this formula:

$$
\begin{aligned}
M_\bullet &= G^{-1} \cdot \left[\ \mathrm{cm}^{-3}\mathrm{g\ s}^2\right] \cdot R_{\rm BLR}\,[\ \text{light-days}\ ] \cdot V^2\left[\ \mathrm{km}^2\ \mathrm{s}^{-2}\right] \\
\text{with } M_\odot &= 1.989 \cdot 10^{33}\,[\ \mathrm{g}\ ] \text{ we have for the BH masses:} \\
\Rightarrow M_\bullet &= \frac{2.590 \cdot 10^{15} \cdot 10^{10}}{6.672 \cdot 10^{-8} 1.989 \cdot 10^{33}} \cdot R_{\rm BLR} \cdot V^2 \\
&= 0.195 \cdot R_{\rm BLR} \cdot V^2 \ \ [\ M_\odot\ ] \\
\Rightarrow \log_{10} M_\bullet &= \log_{10}(0.195) + \log_{10} R_{\rm BLR} + 2 \cdot \log_{10} V\,[\ M_\odot\ ]
\end{aligned}
\tag{4.13}
$$

The first result which has been visually noticed is that the accretion rates should be closely linked to the BH masses: less massive compact objects are typically powered by higher accretion rates (Fig.4.7).

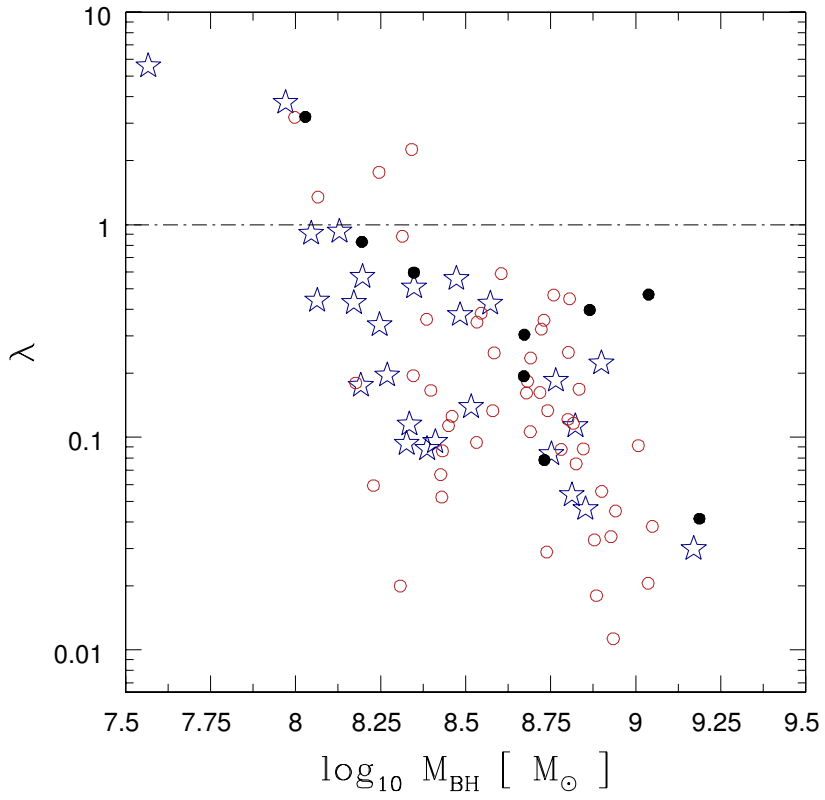

Figure 4.7: View of the trend of Eddington ratios as a function of the masses of the accreting objects: blue stars correspond to known blazars while red circles to object classified by the SDSS's team as QSOs.

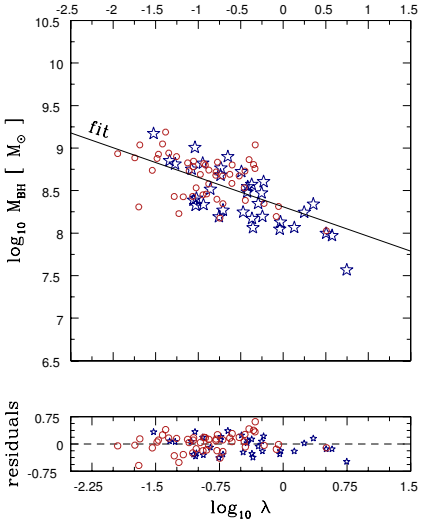

Figure 4.8: BCES bisector fitting results on $\log_{10} M_\bullet$ versus $\log_{10} \lambda_{\rm Edd}$.

In order to find if there were any correlations between $\lambda_{\rm Edd}$ and $M_\bullet$, a linear fit on their logarithmic values was computed with the Python script reported in appendix (listing 10). The results are listed in table 4.7 and illustrated in Fig.4.8.

$\log_{10} M_\bullet$ versus $\log_{10} \lambda_{\rm Edd}$		
	slope	intercept
BCES Bisector	-0.318 ± 0.172	8.309 ± 1.243
bootstrap	-0.338 ± 0.068	8.317 ± 0.057
Pearson's R	-0.66	
2-tailed p-value	$1.04 \cdot 10^{-11}$	

Table 4.7: Values of the BCES bisector fitting on $\log_{10} M_\bullet$ versus $\log_{10} \lambda_{\rm Edd}$.

It has often been reported in the literature that AGNs powered by BHs with lower masses are generally accreting at higher rates. Taking in account the values of the slope and of the Pearson's R, our sample confirms a tight anticorrelation between the accretion rate and the mass of the BH.

4.5 Radio Loudness

The first definition of Radio-Loudness (R) was given in the 80's (Kellermann et al., 1989) and states that:

$$\boxed{R = \frac{f_{5\mathrm{GHZ}}}{f_{\mathrm{B}}}} \tag{4.14}$$

being $f_{5\mathrm{GHz}}$ and f_{B} the monochromatic luminosities at 5GHz and 4400Å at rest frame. This paramater has been used in order to distinguish between radio-loud and radio-quiet objects, with a dividing line where the objects which have $R > 10$ are defined as radio-loud. Usually this value is found in the range $1 < R < 1000$ but for powerful emitting sources it can reach orders of $10^4 - 10^5$ (Ghisellini et al.; table 1). In this work R was evaluated measuring both $f_{5\mathrm{GHz}}$ and f_B from the available data and, finally, using Eq.4.14.

$f_{5\mathrm{GHz}}$ was evaluated taking advantage of the spectral indexes provided by the *SPECFIND 2.0* catalog found in VizieR (Vollmer et al., 2010). This catalog, based on data found in literature, contains 107,488 cross-identified objects with at least three radio sources observed at three independent frequencies. The number of catalogs that were combined together, extracting also the data from the first release, which is also included in the most recent one, is 104. Moreover, it contains both the slope and the intercept of the powerlaw which fits the data points. This was only possible by the development of new tools at the CDS, which use the standards and infrastructure of the VO (Sec.1.4).

The two parameters retrievable from the catalog can be used to interpolate flux density values in the desired frequency through this formula:

$$S(\nu) = A \cdot \log_{10}(\nu) + B \tag{4.15}$$

where $S(\nu)$ in measured in mJy while ν in MHz.

Taking in account that f_{R} should be measured at 5GHz in the rest frame and that this frequency is shifted to lower ones because of Hubble's expansion, a visual inspection of the observed data points of each single source was done in order to test whether the observations were covering the relevant frequencies to perform an interpolation with SPECFIND 2.0. Once having found that they were taken inside the desired frequencies, the computation of f_{R} was done through the SQL language (appendix, listing 16).

The optical fluxes at 4400Å were extrapolated: following the procedure adopted in Sec.4.2 in order to compute the BLR sizes, measurements of the density fluxes at 2500Å were taken on the spectra. The 4400Å flux density values were evaluated assuming an optical spectral index of $\alpha = -0.5$ on the entire sample.

Finally, the computation was done using the SQL language (appendix, listing

	$\log_{10}\lambda_{\rm Edd}$ versus $\log_{10} R$		$\log_{10} {\rm M}_\bullet$ versus $\log_{10} R$	
		Entire sample		
	slope	intercept	slope	intercept
BCES Bisector	1.040 ± 0.045	4.193 ± 0.091	-1.44±0.14	15.79±1.21
bootstrap	0.872 ± 0.562	4.081 ± 0.386	-1.43±0.29	15.70±2.43
Pearson's R	0.18		-0.31	
2-tailed p-value	0.15		0.01	
		QSOs		
	slope	intercept	slope	intercept
BCES Bisector	-1.180 ± 0.113	2.292 ± 0.119	-1.19±0.39	13.54±3.424
bootstrap	-1.112 ± 0.370	2.335 ± 0.327	-0.60±1.32	8.41±11.34
Pearson's R	-0.40		-0.10	
2-tailed p-value	0.03		0.61	
		BLAZARS		
	slope	intercept	slope	intercept
BCES Bisector	0.951 ± 0.086	4.228 ± 0.118	-1.24±0.14	14.20±1.15
bootstrap	0.940 ± 0.213	4.226 ± 0.149	-1.14±0.53	13.41±4.42
Pearson's R	0.37		-0.26	
2-tailed p-value	0.03		0.13	

Table 4.8: Values of the BCES bisector linear fitting on $\log_{10}\lambda_{\rm Edd}$ and $\log_{10}{\rm M}\bullet$ versus R on the entire sample and on two subsamples, each one containing only known blazars or SDSS's team sources defined as QSOs.

17). The values inferred for R are reported in tables 4.10, 4.11 and 4.12 in Sec.4.7, where all the physical parameters computed are stored at the end. As illustrated in Fig.4.9a there is a general trend for QSOs to have lower values of R with increasing $\lambda_{\rm Edd}$: the BCES bisector linear fitting done on these two parameters suggests an output slope of value $a = -1.180$. On the opposite, blazars are fitted with a positive result of $a = 0.951$, as well as the entire sample ($a = 1.040$). The fact that considering the two groups as an unique AGN population increases the 2-Tailed p-value decreasing the Pearson's R both by one order of magnitude, can be interpreted as a warning against the blending of multiple type of sources at a time when trying to find any correlation between radio-loudness and accretion rates. Another argument in favour to this behaviour is given by the plot on the $\log_{10} L_{4400}/L_{\rm Edd}$–$\log_{10} L_R/L_{\rm Edd}$ plane (Fig.4.9b), inspired by Sikora et al. (2008). They divided their sample by AGN populations and found that the same types of sources where located in different areas of the graph, with radio-quiet AGNs with $\lambda_{\rm Edd} < 10^{-2}$ on the bottom left while radio-loud ones ($\lambda_{\rm Edd} < 10^{-1}$, $R > 10^3$) on top right.

BH masses, in respect to R, seem to be distribuited in such a way that the less

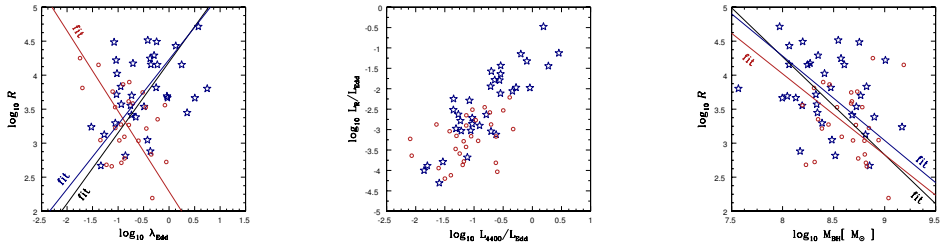

(a) (b) (c)

Figure 4.9: In all figures red circles represent QSOs while blue stars known blazars, which have L_R values up to two orders of magnitude higher than the former. The QSOs in (b) are found in the same area of the ones detected by Sikora et al. (2008), while blazars have also higher values both for $\log_{10} L_{4400}/L_{\rm Edd}$ and $\log_{10} L_R/L_{\rm Edd}$.

massive objects do have the higher R values. In order to verify if this trend is real three linear fits on these parameters were done, at first on the entire sample and at last on the subsamples (blazars or QSOs). The results are reported in table 4.8. The best values are found by considering the entire sample, indicating that the possible connection between $M_\bullet$ and radio loudness can be better appreciated as a general trend, rather than as a specific property of different populations.

4.6 Jet Powers

Two years after the work of Bîrzan et al. (2008), where a prescription for esimating the jet powers from flux densities at 1.4GHz and 327MHz was published, an improved one was developed by Cavagnolo et al. (2010), who expanded the sample to lower radio powers in order to determine if the $P_{\rm JET}$–$P_{\rm radio}$ scaling relations were continuous in form and scatter from giant elliptical galaxies (gEs) up to brightest cluster galaxies (BCGs). They found a mean scaling relation of $P_{\rm JET} \approx 5.8 \cdot 10^{43} (P_{\rm RADIO}/10^{40})^{0.70}$ [erg s^{-1}], continuous over $\sim$ 6–8 decades in $P_{\rm JET}$ and $P_{\rm RADIO}$. The prescription states:

$$\log P_{\rm JET} = 0.75\,(\pm 0.14)\ \cdot\ \log P_{1.4} + 1.91\,(\pm 0.18) \tag{4.16}$$

where $P_{\rm JET}$ is in units of 10^{42}erg s^{-1} while $P_{1.4}$ is in units of 10^{40}erg s^{-1}. The jet powers where computed through the SQL language (appendix, listing 18), the values are reported in tables 4.10, 4.11 and 4.12. As was done with the other estimates, BCES bisector fits were computed, leading to an estimate of the correlations between $P_{\rm JET}$ and the other sources' properties.

The first relation taken in consideration was $\lambda_{\rm Edd}$–$P_{\rm JET}$, whose results are re-

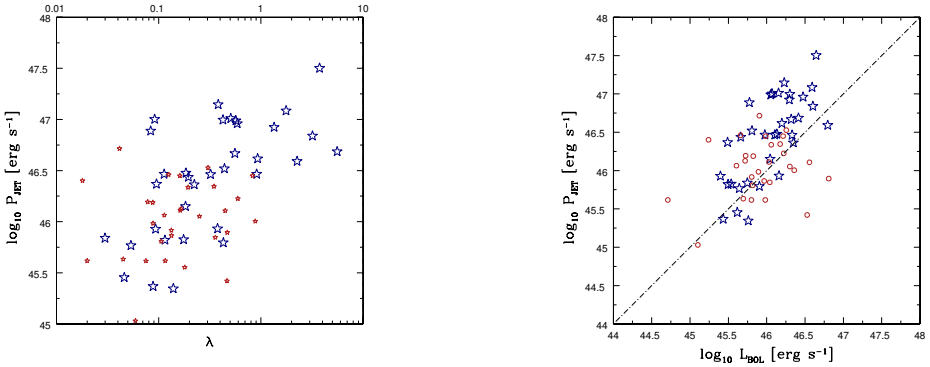

(a) (b)

Figure 4.10: Distribution of the entire sample of sources along the $\lambda_{\rm Edd}$–$\log_{10} P_{\rm JET}$ and $\log_{10} L_{\rm BOL}$–$\log_{10} P_{\rm JET}$ planes: blue stars correspond to known blazars while red circles correspond to sources classified by the SDSS's team as QSOs.

ported in table 4.9 and illustrated in Fig.4.11. The best agreement between $\log \lambda_{\rm Edd}$ and $\log P_{\rm JET}$ was found for the entire sample, whose correlation is stronger than the one observed in blazars, in spite of the apparently uncorrelated properties of QSOs.

BH masses, even if they seem to be well distribuited (Fig.4.12a), are less correlated than accretion rates, suggesting that maybe is $\log_{10} L_{\rm BOL}$ that plays a major role in this relation and, thus, the parameter which should be taken more in account. The Pearson's R (table 4.9) indicates a tight correlation with the accretion rate, which is improved considering only the blazar sample.

Quite obviously, the parameter that best correlates with the jet powers is the radio-loudness, whose Pearson's R scales to higher values when considering only the blazars, having anyway at least a value of 0.71 considering both populations. This relation suggests that, as shown in Fig.2.8, the synchrotron emission of relativistic particles plays a crucial role in determinig the power of the emitted jets: the unified scheme for AGNs (Sec.1.3) is in agreement with this behaviour, in which blazars should emit powerfully in the radio band having therefore higher values for R and $\log_{10} P_{\rm JET}$. In fact, as can be seen in Fig.4.10b, QSO radio luminosities typically do not exceed $5 \cdot 10^{46}$ erg s^{-1} while blazars are also found above, ranging values up to $\sim 10^{46}$ erg s^{-1}.

Summarizing, $\lambda_{\rm Edd}$, R, and $L_{\rm BOL}$ seem to have a good corerelation with $P_{\rm JET}$, while $M_\bullet$ does not. The fact that only the blazars hosting massive BHs are able to emit strongly in the radio band suggests that maybe there are other parameters to take in account, such as the ones pointed out in the literature, like the BH spin (Maraschi et al., 2012).

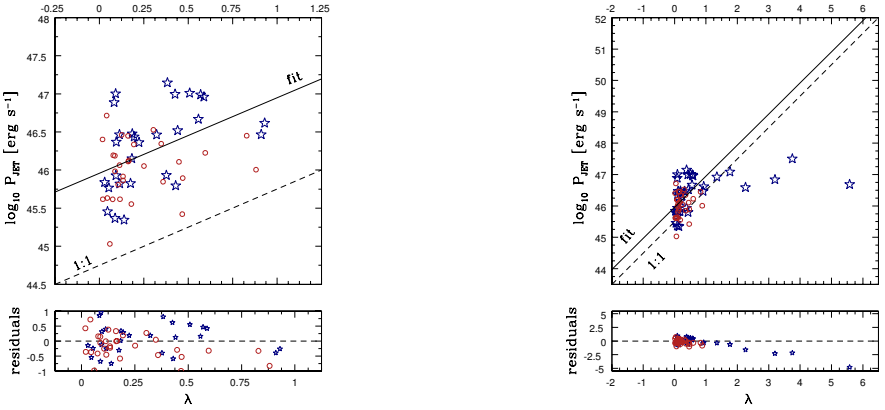

(a) (b)

Figure 4.11: BCES bisector linear fitting for the $\log_{10} P_{\rm JET}$–$\log_{10} \lambda_{\rm Edd}$ relation: the points are assigned in the same manner as in Fig.4.10. Panel (a) represents only the sources which do not radiate at supereddington regimes, while panel (b) shows the entire sample, featuring a break in the jet power at very high accretion rates.

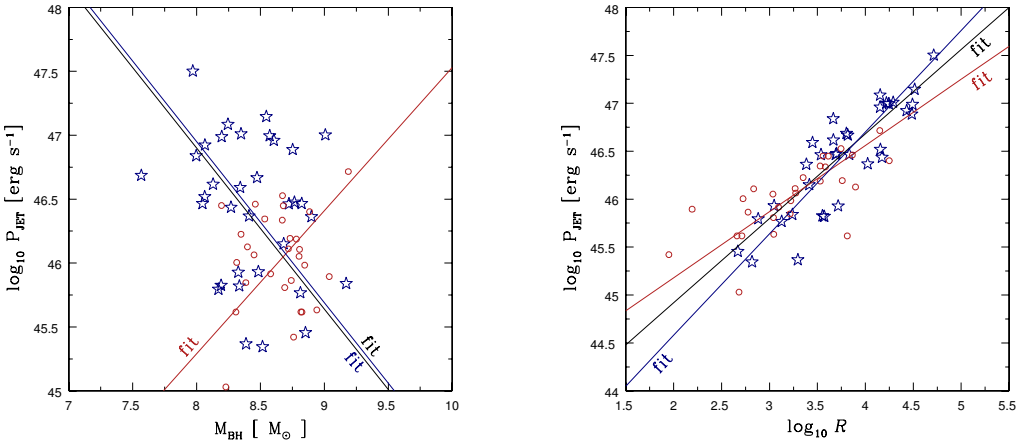

(a) (b)

Figure 4.12: BCES fits for $P_{\rm JET}$ against $\log_{10} \mathrm{M}_\bullet$ and $\log_{10} R$: red circles are referred to QSOs while blue stars to known blazars. The straight lines are combined in colours with the sources involved in the fit. the black one is the straight line fitting the entire sample.

$\log_{10}\lambda_{\rm Edd}$, $\log_{10}{\rm M}_\bullet$, R, and $\log_{10}L_{\rm BOL}$ versus $\log_{10}P_{\rm JET}$								
	$\log_{10}\lambda_{\rm Edd}$ versus $\log_{10}P_{\rm JET}$		$\log_{10}{\rm M}_\bullet$ versus $\log_{10}P_{\rm JET}$		R versus $\log_{10}P_{\rm JET}$		$\log_{10}L_{\rm BOL}$ versus $\log_{10}P_{\rm JET}$	
	slope	intercept	slope	intercept	slope	intercept	slope	intercept
	entire sample							
BCES Bisector	0.97 ± 0.08	4.87 ± 0.08	-1.26 ± 0.11	56.98 ± 0.91	0.88 ± 0.08	43.16 ± 0.29	1.22 ± 0.09	-9.72 ± 4.32
bootstrap	0.98 ± 0.08	4.69 ± 0.08	-1.20 ± 0.41	56.45 ± 3.51	0.88 ± 0.07	43.15 ± 0.27	1.22 ± 0.12	-1.00 ± 5.39
Pearson's R	0.53		-0.25		0.83		0.51	
2-tailed p-value	$5.4 \cdot 10^{-6}$		0.05		$4.7 \cdot 10^{-17}$		$1.6 \cdot 10^{-5}$	
	QSOs							
BCES Bisector	0.96 ± 0.07	4.68 ± 0.19	1.12 ± 0.20	36.33 ± 1.73	0.69 ± 0.15	43.80 ± 0.50	0.94 ± 0.09	3.01 ± 4.29
bootstrap	0.53 ± 0.79	4.64 ± 0.64	0.49 ± 1.10	41.80 ± 9.52	0.69 ± 0.11	43.78 ± 0.37	0.60 ± 0.74	18.58 ± 33.94
Pearson's R	0.15		0.14		0.71		0.23	
2-tailed p-value	0.43		0.47		$1.19 \cdot 10^{-5}$		0.23	
	BLAZARS							
BCES Bisector	0.98 ± 0.11	4.69 ± 0.10	-1.26 ± 0.13	57.03 ± 1.13	1.06 ± 0.07	42.46 ± 0.28	1.43 ± 0.11	-19.43 ± 5.05
bootstrap	0.99 ± 0.12	4.69 ± 0.11	-1.14 ± 0.58	56.01 ± 4.86	1.06 ± 0.07	42.44 ± 0.32	1.06 ± 0.07	-19.72 ± 7.47
Pearson's R	0.62		-0.25		0.87		0.70	
2-tailed p-value	$8.93 \cdot 10^{-5}$		0.16		$1.63 \cdot 10^{-11}$		$3.28 \cdot 10^{-6}$	

Table 4.9: Results of the BCES bisector linear fitting for $\log_{10}\lambda_{\rm Edd}$, $\log_{10}{\rm M}_\bullet$, R, and $\log_{10}L_{\rm BOL}$ versus $\log_{10}P_{\rm JET}$.

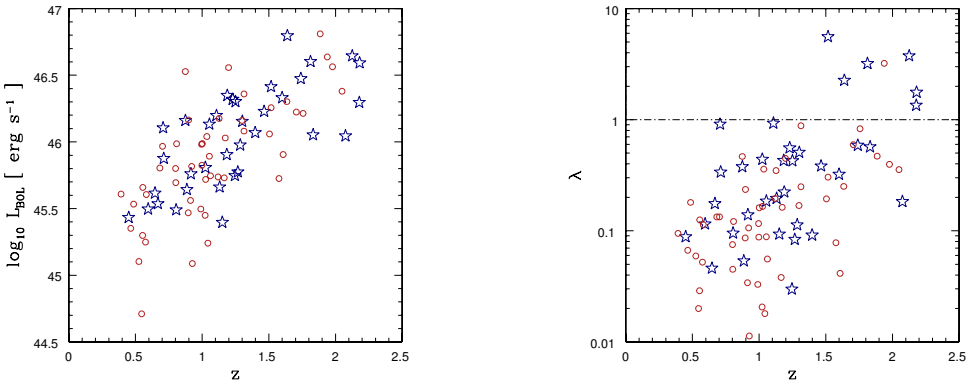

(a) (b)

Figure 4.13: $\log_{10} L_{\rm BOL}$ (*left*) and $\lambda_{\rm Edd}$ (*right*) versus z: blue stars correspond to known blazars while red circles to sources identified as QSOs by the SDSS's team.

4.7 Redshift Distribution

As shown in Fig.4.13a there is a correlation between the z value and the bolometric luminosity: at high redshift only the intrinsically brightest objects can be seen. This happens due to selection effects. Because of this behaviuor, it is also necessary to take in consideration the fact that $\lambda_{\rm Edd}$ (Eq.2.3) scales linearly with the luminosity, thus, also the accretion rates have high values when the distance from the observing point increases, as can be seen in Fig.4.13b.

The distribution of masses, illustrated in Fig.4.14, on the other hand, shows an interesting trend: the data points seem to scale from lower to higher values starting from $z \simeq 0$ to $z \simeq 1.5$, where the trend starts to be inverted with the masses being lower as the redshift increases. This can be interpreted as a $M_\bullet$ growing with cosmic time: starting from the early epochs of the Universe, some of the best accreting SMBHs, hosted by young galaxies, reached values in the range of $\sim 10^8$–10^9 $M_\odot$. This trend is confirmed in literature (Trakhtenbrot and Netzer, 2012) and the position of the maximum depends obviously on the adoptded parameters for governing the cosmological model.

We present in tables 4.10, 4.11, and 4.12 our estimates of the most important physical properties of our sample of AGNs. Details on the discussion of the results of this work will be given in the conclusions (chapter 5).

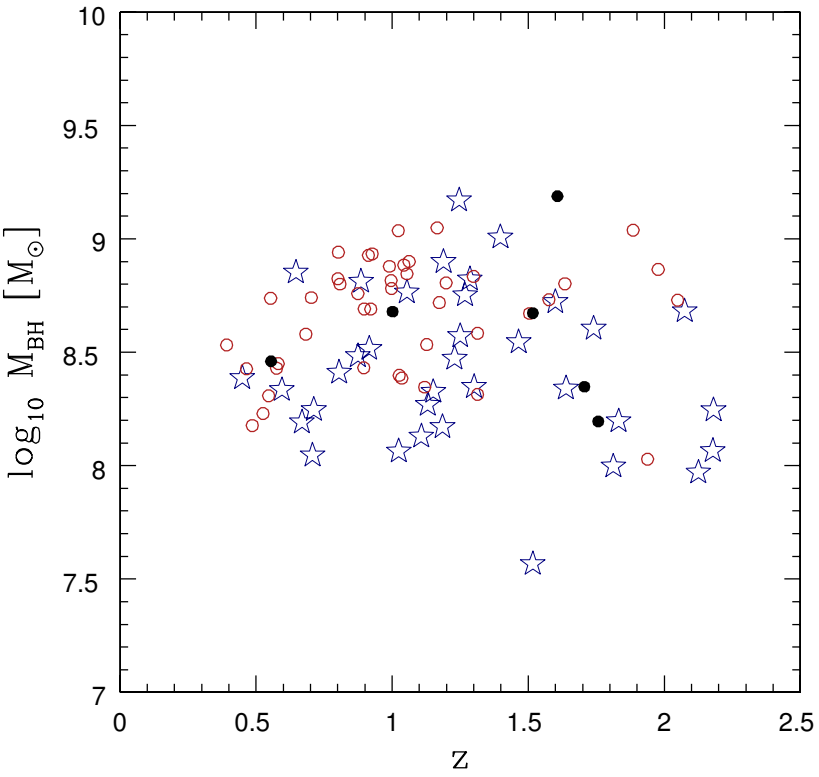

Figure 4.14: Distribution of the SMBH masses as a function of z: blue stars correspond to known blazars while red circles to sources identified as QSOs by the SDSS's team. Black filled circles have the same meaning as in Fig.5.1.

									Hβ×MgII							
plate	mjd	fiberid	SDSS	bz4	α [deg] [J2000]	δ [deg] [J2000]	z	d_L [Mpc]	$\log_{10} L_{3000}$ [erg s^{-1}]	$\log_{10} L_{bol}$ [erg s^{-1}]	$\log_{10} R_{\rm BLR}$ [lt-days]	$\log_{10}$ M$_\bullet$ [M$_\odot$]	$\lambda_{\rm Edd}$	$\log_{10} R$	$\log_{10} P_{\rm JET}$ [erg s^{-1}]
873	52674	154	J102310.58+475145.5		155.7941	47.8626	0.581	3396.5	44.89±0.03	45.61±0.09	1.88±0.02	8.45±0.39	0.113±0.058	3.27	46.06±0.42
1202	52672	177	J094128.82+444742.8		145.3701	44.7952	0.801	5025.4	45.08±0.01	45.80±0.08	2.00±0.01	8.82±0.20	0.075±0.011	2.66	45.62±0.31
1287	52728	420	J141946.36+463424.3		214.9432	46.5734	0.546	3153.6	43.99±0.07	44.71±0.11	1.33±0.05	8.31±0.20	0.020±0.011	3.81	45.62±0.35
1287	52728	565	J142345.33+465057.3		215.9389	46.8492	0.554	3202.4	44.58±0.05	45.30±0.10	1.69±0.03	8.74±0.24	0.029±0.017	-	-
1378	53061	62	J140003.07+391055.1		210.0128	39.1820	0.803	5038.7	44.98±0.01	45.69±0.09	1.94±0.01	8.94±0.19	0.045±0.009	3.04	45.63±0.31
1380	53084	155	J141740.44+381821.0	BZQJ1417+3818	214.4185	38.3058	0.449	2492.5	44.71±0.06	45.43±0.10	1.77±0.04	8.39±0.19	0.088±0.048	3.29	45.37±0.33
1453	53084	327	J122506.50+483435.1	BZQJ1225+4834	186.2771	48.5764	0.647	3867.2	44.90±0.01	45.62±0.09	1.89±0.01	8.85±0.19	0.046±0.007	2.66	45.46±0.30
1605	53062	125	J111916.12+110107.1		169.8172	11.0186	0.392	2122.3	44.89±0.03	45.61±0.09	1.88±0.02	8.53±0.21	0.095±0.030	-	-
1605	53062	508	J112129.75+123617.4		170.3740	12.6048	0.683	4132.9	45.09±0.03	45.80±0.09	2.00±0.02	8.58±0.23	0.133±0.029	3.09	45.92±0.37
1674	53464	428	J143552.24+472406.7		218.9677	47.4018	0.809	5084.4	45.27±0.02	45.99±0.09	2.12±0.01	8.80±0.16	0.122±0.017	-	-
1674	53464	581	J144318.55+472556.7		220.8273	47.4324	0.703	4283.5	45.25±0.03	45.70±0.09	2.11±0.02	8.74±0.23	0.134±0.074	2.77	45.86±0.36
1752	53379	322	J111118.52+153033.0		167.8272	15.5091	0.526	3010.8	44.39±0.06	45.10±0.10	1.57±0.04	8.23±0.21	0.059±0.049	2.68	45.03±0.26
1991	53446	343	J114654.28+323652.3		176.7262	32.6145	0.465	2597.2	44.64±0.05	45.35±0.10	1.72±0.03	8.43±0.71	0.067±0.281	-	-
1991	53446	604	J115700.60+324457.8		179.2525	32.7494	0.486	2740.1	44.82±0.04	45.53±0.09	1.84±0.02	8.18±0.26	0.180±0.080	-	-
2023	53851	515	J132041.30+351609.4		200.1721	35.2692	0.576	3357.0	44.53±0.06	45.25±0.11	1.66±0.04	8.43±0.20	0.052±0.025	-	-
2367	53763	77	J103632.97+220312.2	BZQJ1036+2203	159.1374	22.0534	0.595	3495.2	44.78±0.04	45.50±0.10	1.81±0.03	8.33±0.19	0.115±0.032	3.57	45.82±0.37
2583	54095	414	J095359.23+172056.6	BZQJ0953+1720	148.4968	17.3490	0.712	4351.6	45.16±0.02	45.88±0.09	2.05±0.02	8.25±0.30	0.338±0.120	-	-
2600	54243	55	J124357.64+162253.4		190.9902	16.3815	0.555	3214.2	44.94±0.04	45.66±0.09	1.91±0.02	8.46±0.25	0.126±0.028	3.86	46.46±0.49
6017	56075	51	J143748.57+243905.9		219.4524	24.6516	1.002	6621.4	45.27±0.02	45.99±0.09	2.12±0.01	8.68±0.33	0.161±0.054	3.61	46.45±0.42
6467	56270	466	J095649.87+251516.0	BZQJ0956+2515	149.2078	25.2544	0.708	4317.0	45.39±0.02	46.11±0.09	2.19±0.01	8.05±0.18	0.911±0.109	3.69	46.47±0.46
6488	56364	486	J125757.23+322929.2	BZQJ1257+3229	194.4885	32.4914	0.805	5058.0	44.77±0.03	45.49±0.09	1.81±0.02	8.41±0.19	0.095±0.028	4.02	46.37±0.43
7406	56805	234	J133245.24+472222.6	BZQJ1332+4722	203.1885	47.3729	0.669	4028.9	44.82±0.02	45.54±0.09	1.84±0.01	8.19±0.25	0.176±0.077	3.55	45.83±0.36

Table 4.10: Hβ×MgII physical parameters.

					MgII								
plate	mjd	fiberid	SDSS	bz4	α [deg] [J2000]	δ [deg] [J2000]	z	d_L [Mpc]	$\log_{10} L_{3000}$ [erg s^{-1}]	$\log_{10} L_{bol}$ [erg s^{-1}]	$\log_{10} R_{\rm BLR}$ [lt-days]	$\log_{10}$ M$_\bullet$ [M$_\odot$]	$\lambda_{\rm Edd}$	$\log_{10} R$	$\log_{10} P_{\rm JET}$ [erg s^{-1}]
874	52338	125	J102713.08+480313.5	BZQJ1027+4803	156.8045	48.0537	1.285	9018.2	45.26±0.10	45.97±0.13	2.11±0.06	8.82±0.28	0.113±0.021	3.83	46.47±0.39
943	52376	135	J100821.57+440016.5	BZQJ1008+4400	152.0899	44.0045	1.185	8154.2	45.18±0.11	45.90±0.14	2.06±0.07	8.17±0.41	0.430±0.122	2.88	45.80±0.29
1287	52728	435	J142020.68+462440.9	BZQJ1420+4624	215.0862	46.4113	1.246	8677.5	45.03±0.12	45.74±0.14	1.96±0.07	9.17±0.15	0.030±0.005	3.23	45.84±0.29
1377	53050	443	J134523.83+412541.5	BZUJ1345+4125	206.3493	41.4282	0.916	5929.8	45.04±0.10	45.76±0.13	1.97±0.06	8.51±0.18	0.139±0.025	2.81	45.35±0.25
1453	53084	391	J122607.92+473700.5		186.5330	47.6168	1.054	7055.2	45.17±0.11	45.89±0.14	2.05±0.07	8.84±0.18	0.088±0.013	3.22	45.98±0.33
1453	53084	572	J123354.45+482049.9		188.4769	48.3472	0.996	6578.4	45.26±0.08	45.98±0.12	2.11±0.05	8.81±0.16	0.116±0.014	2.71	45.62±0.28
1457	53116	403	J125248.28+474043.7		193.2012	47.6788	0.921	5974.5	45.10±0.09	45.81±0.12	2.01±0.05	8.69±0.20	0.106±0.019	3.04	45.81±0.32
1458	53119	331	J125436.96+421644.2		193.6540	42.2789	0.913	5905.8	44.84±0.15	45.56±0.17	1.85±0.09	8.92±0.18	0.034±0.009	-	-
1459	53117	594	J130851.33+472954.9	BZQJ1308+4729	197.2139	47.4986	0.885	5688.5	44.92±0.12	45.64±0.14	1.90±0.07	8.81±0.19	0.053±0.012	3.12	45.77±0.32
1461	53062	464	J131706.02+465034.9		199.2751	46.8430	1.022	6791.9	44.73±0.16	45.44±0.19	1.78±0.10	9.03±0.18	0.020±0.007	-	-
1749	53357	18	J105144.87+125828.9		162.9370	12.9747	1.314	9266.8	45.36±0.08	46.08±0.11	2.17±0.05	8.58±0.16	0.249±0.025	-	-
1771	53498	142	J130020.92+141718.5	BZQJ1300+1417	195.0872	14.2884	1.107	7494.7	45.48±0.08	46.19±0.11	2.24±0.05	8.12±0.32	0.930±0.136	3.66	46.62±0.43
1952	53378	164	J100607.70+323626.1		151.5321	32.6072	1.025	6819.2	45.00±0.10	45.71±0.13	1.95±0.06	8.39±0.20	0.166±0.034	3.89	46.13±0.36
1984	53433	356	J122641.95+402633.2		186.6748	40.4425	1.299	9135.3	45.44±0.06	46.16±0.11	2.22±0.04	8.83±0.14	0.168±0.014	-	-
1985	53431	348	J123915.00+404955.4		189.8125	40.8320	1.314	9265.1	45.64±0.05	46.35±0.10	2.34±0.03	8.31±0.20	0.881±0.068	2.72	46.00±0.31
2006	53476	192	J125926.73+333339.3		194.8614	33.5609	1.062	7122.1	45.02±0.11	45.74±0.14	1.96±0.07	8.89±0.14	0.055±0.009	-	-
2017	53474	172	J134254.38+282805.8		205.7266	28.4683	1.035	6898.1	45.32±0.06	46.04±0.11	2.15±0.04	8.38±0.17	0.358±0.039	3.21	45.85±0.31
2020	53431	459	J124021.14+350258.7		190.0881	35.0496	1.198	8269.2	45.84±0.03	46.55±0.09	2.47±0.02	8.80±0.13	0.448±0.019	2.83	46.11±0.34
2023	53851	137	J131736.50+342515.9	BZQJ1317+3425	199.4021	34.4210	1.054	7053.5	45.41±0.06	46.13±0.10	2.20±0.04	8.76±0.18	0.185±0.018	3.70	46.48±0.41
2352	53770	19	J103941.95+242240.8		159.9248	24.3780	1.173	8057.3	45.31±0.08	46.02±0.11	2.14±0.05	8.71±0.14	0.162±0.017	3.26	46.11±0.34
2484	54144	431	J105148.79+211952.3	BZQJ1051+2119	162.9533	21.3312	1.300	9150.3	45.43±0.07	46.15±0.11	2.22±0.04	8.34±0.19	0.507±0.053	4.29	47.01±0.48
2583	54095	373	J095145.69+173622.7		147.9404	17.6063	0.895	5769.6	44.75±0.15	45.46±0.17	1.79±0.09	8.43±0.37	0.086±0.042	-	-
2755	54507	597	J135205.18+185335.4		208.0216	18.8931	0.897	5785.4	45.44±0.04	46.16±0.09	2.22±0.02	8.69±0.14	0.235±0.019	-	-
2763	54507	363	J144635.35+172107.5	BZQJ1446+1721	221.6473	17.3521	1.024	6806.9	45.09±0.05	45.80±0.10	2.00±0.03	8.06±0.17	0.440±0.067	4.15	46.52±0.42
3223	54865	2	J094538.11+353455.0		146.4088	35.5819	1.127	7665.0	45.45±0.03	46.17±0.09	2.23±0.02	8.53±0.32	0.348±0.052	3.52	46.35±0.38
3367	54998	614	J130217.18+481917.5	BZQJ1302+4819	195.5716	48.3215	0.874	5597.8	45.44±0.06	46.16±0.10	2.22±0.03	8.48±0.24	0.377±0.045	3.04	45.93±0.35
4568	55600	112	J101810.96+354239.4	BZQJ1018+3542	154.5457	35.7109	1.229	8532.9	45.60±0.05	46.31±0.10	2.32±0.03	8.47±0.14	0.557±0.037	3.81	46.67±0.43
4576	55592	440	J092551.84+361235.6		141.4660	36.2099	0.998	6593.1	45.10±0.09	45.82±0.12	2.01±0.05	8.78±0.12	0.087±0.011	3.52	46.19±0.37
4636	55945	400	J094855.34+403944.6	BZQJ0948+4039	147.2306	40.6624	1.250	8711.2	45.58±0.04	46.30±0.09	2.31±0.02	8.57±0.17	0.426±0.031	4.24	47.00±0.48
4643	55946	942	J091648.91+385428.1	BZQJ0916+3854	139.2038	38.9078	1.267	8862.4	45.05±0.07	45.77±0.11	1.98±0.04	8.75±0.17	0.083±0.013	4.48	46.89±0.46
5337	55987	962	J102459.85+172147.4		156.2494	17.3631	0.926	6016.8	44.37±0.21	45.08±0.23	1.56±0.13	8.93±0.15	0.011±0.006	-	-
5412	55981	176	J125249.87+112933.1		193.2078	11.4925	0.874	5597.0	45.81±0.02	46.52±0.09	2.45±0.01	8.75±0.19	0.466±0.027	1.95	45.42±0.27
5766	56248	532	J093040.05+193653.7		142.6669	19.6149	1.165	7986.8	45.01±0.09	45.73±0.12	1.95±0.05	9.04±0.09	0.038±0.005	-	-
5777	56280	302	J091548.09+250858.9		138.9504	25.1497	1.043	6963.1	44.52±0.18	45.24±0.20	1.65±0.11	8.88±0.25	0.018±0.009	4.24	46.40±0.40
5849	56033	376	J121503.98+165438.0	BZQJ1215+1654	183.7666	16.9105	1.131	7696.1	44.94±0.10	45.66±0.13	1.91±0.06	8.26±0.09	0.195±0.029	4.17	46.44±0.40
6003	56311	96	J134208.37+270930.5	BZQJ1342+2709	205.5349	27.1584	1.188	8184.9	45.63±0.02	46.34±0.08	2.34±0.01	8.89±0.15	0.223±0.013	3.38	46.36±0.38
6003	56311	432	J133602.83+272751.6		204.0118	27.4643	1.119	7600.5	45.02±0.07	45.73±0.11	1.96±0.04	8.34±0.28	0.195±0.049	-	-
6404	56330	375	J115318.07+234113.5		178.3253	23.6870	0.990	6527.6	44.78±0.15	45.49±0.17	1.81±0.09	8.87±0.14	0.032±0.009	-	-
6617	56365	896	J124600.00+434626.9	BZQJ1245+4346	191.5000	43.7741	1.151	7865.9	44.68±0.11	45.39±0.14	1.75±0.07	8.32±0.26	0.093±0.037	3.71	45.93±0.31

Table 4.11: MgII physical parameters.

					MgII×CIV									
plate	mjd	fiberid	SDSS	bz4	α [deg] [J2000]	δ [deg] [J2000]	z	d_L [Mpc]	$\log_{10} L_{3000}$ [erg s^{-1}]	$\log_{10} L_{bol}$ [erg s^{-1}]	$\log_{10} R_{\rm BLR}$ [lt-days]	$\log_{10} M_\bullet$ [$M_\odot$]	$\lambda_{\rm Edd}$	$\log_{10} R$	$\log_{10} P_{\rm JET}$ [erg s^{-1}]
940	52670	457	J093857.17+424829.3		144.7382	42.80815	2.0492	16009.6	45.67±0.11	46.38±0.14	2.36±0.07	8.73±0.27	0.355±0.072	-	-
1380	53084	107	J141946.60+382148.4	BZQJ1419+3821	214.9442	38.36345	1.8323	13958.5	45.34±0.16	46.05±0.18	2.16±0.10	8.20±0.23	0.570±0.106	4.49	46.99±0.43
1605	53062	434	J111857.30+123411.7	BZQJ1118+1234	169.7388	12.57825	2.1252	16738.5	45.93±0.07	46.65±0.11	2.53±0.04	7.97±0.25	3.753±0.196	4.71	47.50±0.51
1838	53467	46	J140150.37+333954.0		210.4599	33.66501	1.6349	12133.0	45.59±0.06	46.30±0.11	2.31±0.04	8.80±0.32	0.251±0.031	3.03	46.05±0.29
1989	53772	482	J125102.67+384507.3		192.7611	38.75204	1.5054	10959.3	45.34±0.05	46.06±0.10	2.16±0.03	8.67±0.34	0.194±0.091	3.58	46.34±0.35
1992	53466	219	J122847.42+370612.0	BZQJ1228+3706	187.1976	37.10336	1.5167	11060.9	45.70±0.03	46.41±0.09	2.38±0.02	7.57±0.17	5.580±0.240	3.80	46.69±0.41
2008	53473	565	J114636.75+320004.1		176.6532	32.00114	1.7574	13261.1	45.50±0.06	46.21±0.11	2.26±0.04	8.20±0.28	0.829±0.145	3.55	46.45±0.35
2031	53848	108	J125829.75+352843.6		194.6240	35.47879	1.8855	14457.5	46.09±0.05	46.81±0.10	2.63±0.03	9.04±0.20	0.469±0.054	2.19	45.89±0.26
2036	53446	468	J113053.28+381518.6	BZQJ1130+3815	172.7220	38.25518	1.7404	13103.4	45.76±0.03	46.47±0.09	2.42±0.02	8.60±0.21	0.588±0.066	4.15	46.96±0.44
2093	53818	298	J131059.40+323334.3	BZQJ1310+3233	197.7475	32.55956	1.6391	12171.1	46.08±0.01	46.80±0.09	2.62±0.01	8.34±0.32	2.261±0.268	3.44	46.59±0.38
2108	53473	533	J120637.04+394103.7		181.6544	39.68438	1.5172	11065.0	45.54±0.05	46.26±0.10	2.29±0.03	8.67±0.38	0.304±0.087	3.74	46.53±0.38
2238	54205	608	J124918.41+281743.6		192.3267	28.29546	1.7064	12789.2	45.51±0.07	46.22±0.11	2.27±0.04	8.35±0.30	0.596±0.056	3.35	46.23±0.32
2352	53770	409	J103516.52+261517.3		158.8188	26.25482	1.6076	11883.6	45.20±0.16	45.91±0.18	2.07±0.10	9.19±0.29	0.041±0.025	4.15	46.72±0.40
3395	55004	444	J123505.80+362119.3	BZQJ1235+3621	188.7742	36.35537	1.5998	11812.9	45.62±0.06	46.33±0.10	2.33±0.03	8.72±0.27	0.322±0.071	3.53	46.46±0.36
3982	55332	280	J132547.67+341320.6		201.4487	34.22241	1.9388	14960.2	45.92±0.03	46.64±0.09	2.52±0.02	8.03±0.27	3.218±0.144	-	-
5473	56033	742	J144642.37+142801.4		221.6765	14.46707	1.9776	15327.8	45.85±0.03	46.56±0.09	2.48±0.02	8.86±0.35	0.397±0.054	-	-
5736	55984	564	J090303.98+465104.1	BZQJ0903+4651	135.7666	46.85115	1.4651	10598.1	45.51±0.02	46.23±0.09	2.27±0.02	8.55±0.16	0.383±0.040	4.51	47.15±0.49
5858	56063	188	J134723.49+183537.5	BZQJ1347+1835	206.8479	18.59376	2.1785	17252.0	45.58±0.10	46.30±0.13	2.31±0.06	8.07±0.23	1.348±0.091	4.43	46.92±0.40
5995	56093	326	J132700.86+221050.1	BZQJ1327+2210	201.7536	22.18061	1.3978	10000.0	45.35±0.07	46.07±0.11	2.17±0.04	9.01±0.46	0.092±0.114	4.22	47.00±0.47
6475	56337	180	J120727.90+275458.8	BZQJ1207+2754	181.8663	27.91635	2.1809	17275.3	45.88±0.05	46.59±0.10	2.49±0.03	8.25±0.14	1.765±0.085	4.15	47.09±0.43
6626	56330	647	J133857.15+430235.0		204.7382	43.04308	1.5760	11596.4	45.01±0.05	45.73±0.10	1.96±0.03	8.73±0.45	0.078±0.067	3.75	46.19±0.32
6648	56383	996	J112657.65+451606.3	BZQJ1126+4516	171.7402	45.26843	1.8131	13779.1	45.89±0.02	46.60±0.09	2.50±0.01	8.00±0.20	3.199±0.092	3.66	46.84±0.41
6663	56338	262	J100412.86+462622.6	BZQJ1004+4626	151.0536	46.43961	2.0748	16254.7	45.33±0.14	46.05±0.17	2.15±0.09	8.68±0.20	0.183±0.036	3.41	46.15±0.28

Table 4.12: MgII×CIV physical parameters.

CHAPTER 5

CONCLUSIONS

The first result that has to be pointed out is that the accretion rates are strongly linked both with the jet powers (Fig.4.10a) and, as a consequence, to the source radio-loudness (Fig.4.12b). Moreover, there is a general trend in $\lambda_{\rm Edd}$ to grow up with z, fact due to both selection effects – which do not permit to observe faint sources at high distances – and to the increasing mass observed for SMBHs in the close Universe, with respect to earlier cosmological epochs, leading to generally smaller Eddington ratios, according to Eq.2.3.

In addition, the BH mass distribution along the redshift axis manifests itself as an inverted bell with a peak at $z \sim 1.5$, fact that is in agreement with the "black holes growth" paradigm (Trakhtenbrot and Netzer, 2012), which predicts that a peak in the AGN growth in earlier cosmological times would result in the formation of very massive objects that could still be active at intermediate redshifts, peak being determined probably by the choice of different parameters used for the cosmology.

Another point of interest comes from the comparison of the BLR sizes estimated through the Hβ and MgII methods (Eq.4.12), which are in fairly good agreement, while the CIV prescription leads to one order of magnitude lower estimates for $R_{\rm BLR}$ evaluated in light-days (Eq.4.6b).

We note that the sources detected by Fermi-LAT are mostly the ones which have the highest values of R and $P_{\rm JET}$, indicating that they are detected mostly when the source emits powerfully in the radio and γ bands due to SSC (Sec.2.2.3). One of the objects shown in Fig.5.1 was not present in the 2FGL catalog. This suggests that the detection of sources at γ-rays is still affected by sensitivity issues, which require ongoing observations or new generation instruments, and that probably the algorithm for the evaluation of the γ background needs improvements because a

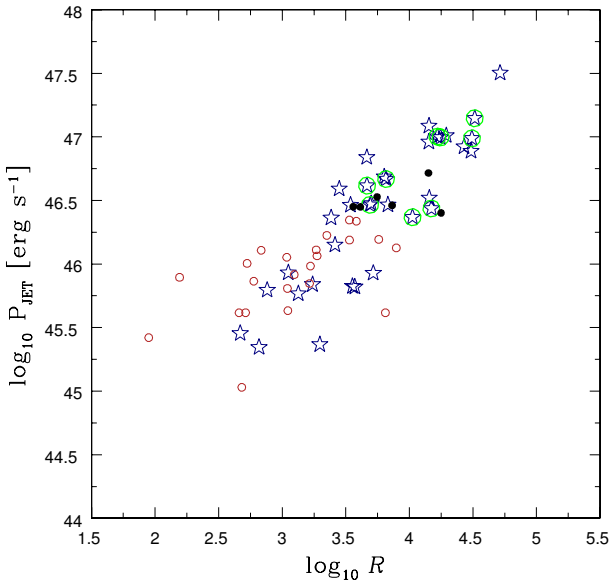

Figure 5.1: Blazars detected by Fermi: red circles correspond to sources identified as QSOs by the SDSS's team, while stars to known blazars. The nine stars highlighted with green circles are sources listed in the 3FGL catalog, while while black filled circles are blazar candidates drawn from the SDSS QSO sample.

little change in the code leads to the loss of sources, which are mistakely interpreted as noise. This behaviour makes us suppose that the 6 sources marked with filled black circles (Fig.5.1) and listed in Tab.5.1, which have $P_{\rm JET} \gtrsim 10^{46.4}$ erg s^{-1} and belong to groups Hβ×MgII and MgII×CIV, are indeed still undetected blazars which should have their HE peaks detectable by Fermi-LAT. The results of our study suggest that the population of radio-loud AGNs, identified by matching radio and X-ray observations is generally consistent with the properties of known blazars. These objects are probably hosting powerful relativistic jets and they are likely good candidates for future detections in the high energy regime.

Identifier (IAU)	plate	mjd	fiberid
SDSS J114636.76+320004.1	2008	53473	565
SDSS J120637.05+394103.7	2108	53473	533
SDSS J103516.51+261517.3	2352	53770	409
SDSS J124918.40+281743.6	2238	54205	608
SDSS J143748.57+243905.9	6017	56075	51
SDSS J124357.64+162253.4	2600	54243	55

Table 5.1: Identifiers of the blazar candidates.

ACRONYMS

R Radio-Loudness. 73

3C Third Cambridge Survey. 5

3FGL LAT 4-year Point Source Catalog. 48

ACD Anticoincidence Detector. 45

ADAF Advection Dominated Accretion Flow. 23

AGILE Astro-rivelatore Gamma a Immagini LEggero. 47

AGN Active Galactic Nucleus. 1

AIPS Astronomical Image Processing System. 43

ASCII American Standard Code for Information Interchange. 48

AU Astronomical Unit. 19

AURA Association of Universities for Research in Astronomy. 51

BB Black Body. 21

BBB Big Blue Bump. 1

BCES Bivariate, Correlated Errors and intrinsic Scatter. 60

BCG brightest cluster galaxy. 76

BeppoSAX The BeppoSAX Mission. 6

BH Black Hole. 2

BLR Broad Line Region. 2, 9

BLRG Broad Line Radio Galaxy. 13

CCD Charge-Coupled Device. 40

CDS Centre de Données astronomiques de Strasbourg. 48

CfA Harvard-Smithsonian Center for Astrophysics. 18

CHANDRA Chandra X-ray observatory. 6

CL Command Language. 53

CLI Command Line Interface. 16

CSV Comma Separated Values. 48

CXC Chandra X-Ray Observatory. 18

DAQ Data Acquisition System. 45

DR12 Data Release 12. 40

eBOSS Extended Baryon Oscillation Spectroscopic Survey. 40

EC External Compton. 36

EM Electromagnetic. 5

ESA European Space Agency. 7

EUV Extreme Ultraviolet. 41

eV elettronvolt. 11

EW Equivalent Width. 35

FIR Far Infrared. 2

FIRST Faint Images of the Radio Sky at Twenty-Centimeters. 39

FITS Flexible Image Transport System. 50

FSRQ Flat Spectrum Radio Quasar. 14

FWHM Full Width Half Maximum. 9, 10

GBM Gamma-ray Burst Monitor. 44

gE giant elliptical galaxy. 76

GLAST Gamma-ray Large Area Space Telescope. 44

GRB Gamma-ray Burst. 44

GUI Grafical User Interface. 16

H hydrogen. 4

HBL High Frequeny Peaked BL Lac Object. 36

HDU Header Data Unit. 50

HE High Energy. 18

HEW Half Energy Width. 42

HPQ Highly Polarized Quasar. 35

HRI High Resolution Imager. 41

HSP High-Synhrotron-Peaked. 36

HST Hubble Space Telescope. 7

IBL Intermediate BL Lac Object. 36

IC Inverse Compton. 11, 17

IDV Intraday Variability. 35

INTEGRAL The INTErnational Gamma-Ray Astrophysics Laboratory. 6

IR infrared. 12

ISP Intermediate Synchrotron Peaked. 36

IUE International Ultraviolet Explorer. 15

LAT Large Area Telescope. 44

LBL Low Frequeny Peaked BL Lac Object. 35

LRG Luminous Red Galaxy. 40

LSP Low Synhrotron Peaked. 35

MCP Microchannel Plate. 42

MHD Magnetohydrodynamic. 24

MIR mid-infrared. 12

MJD Modified Julian Date. 50

MRN Median Ratio Normalization. 13

MW Milky Way. 4

NASA National Aeronautics and Space Administration. 5, 7

NED NASA/IPAC Extragalactic Database. 53

NLR Narrow Line Region. 2, 10

NLRG Narrow Line Radio Galaxy. 13

NRAO National Radio Astronomy Observatory. 42

NVSS NRAO VLA Sky Survey. 42

OVV Optically Violent Variable. 35

PC Personal Computer. 15

pc parsec. 9

POSS-I First Palomar Sky Survey. 43

PSPC Position Sensitive Proportional Counter. 41

RASS ROSAT All-Sky Survey. 42

RASSFSC ROSAT All-Sky Survey Faint Source Catalog. 47

RM reverberation-mapping. 61

rms Root Mean Square. 43

ROSAT Röntgensatellit. 6, 41

RW Robertson-Walker. 58

S/N Signal to Noise Ratio. 49

SAS DR12 Science Archive Server. 49

SDSS Sloan Digital Sky Survey. 39

SE South East. 43

SED Spectral Energy Distribution. 2

SEGUE Sloan Extension for Galactic Understanding and Exploration. 40

SMBH Super Massive Black Hole. 2

SQL Structure Query Language. 16

SSC synchrotron self-Compton. 34

STSCI Space Telescope Science Institute. 15

STSDAS Space Telescope Science Data Analysis System. 51

SW South West. 43

SWIFT The Swift Gamma-Ray Burst Mission. 6

TSp Spectral Type. 40

URL Uniform Resource Locator. 50

UV Ultra Violet. 1

VHE Very High Energy. 35

VLA Karl G. Jansky Very Large Array. 42

VLBI Very Long Baseline Interferometry. 17

VO Virtual Observatory. 16

VT Virial Theorem. 21

WFC Wide Field Camera. 41

WFPC2 Wide Field and Planetary Camera 2. 7

WWW World Wide Web. 15

XMM-Newton X-ray Multi-Mirror Mission. 6

XRT X-ray Telescope. 41

YSO Young Stellar Object. 17

APPENDIX

C++ codes

Listing 1: Computing the luminosity distance.

```
#include<cstdio>
#include<cmath>

int main(int argc, char** argv)
{
  const double H0 = 70;
  const double OmegaM = 0.3, OmegaL = 0.7;
  const double DH = 299792 / H0;
  double distance = 0, z, scale;
  double DC = 0;
  int i = 0;
  //z = StrToDouble(argv[1]);
  sscanf(argv[1], "%lf", &z);

  for (double zi = 0; zi <= z; zi += 0.0001)
    {
      DC += (0.0001 / sqrt((OmegaM * (1 + zi) * (1 + zi) * (1
          + zi)) + OmegaL));
    }
  DC *= DH;
  distance = DC * (1 + z);
  printf("\nLa distanza corrispondente al redshift z = %.3lf
     vale D = %.1lf Mpc.", z, distance);
  scale = distance * 4.848;
  printf("\nLa scala associata vale %lf pc / \".\n", scale);
  return 0;
}
```

CL scripts

Listing 2: Extracting column values with STSDAS's *tables.tdump* task.

```
tdump spec-0765-52254-0019.fits[1][c:loglam,FLUX] > tdspec
   -0765-52254-0019.txt
...
...
tdump spec-7416-56810-0975.fits[1][c:loglam,FLUX] > tdspec
   -7416-56810-0975.txt
```

Listing 3: Building a spectrum with noao's *onedspec.sinterp* task.

```
#PARAMETERS  (BOSS)
  PACKAGE = onedspec
   TASK = sinterp

tbl_file=                       File containing table of x-y
   pairs
input   =                 STDIN  input for x-interpolant
   values
image   =                        Image name to create
(order  =                     1) Order of fit
x1      =           3.556302501) First point in range of
   generated curve
(x2     =           4.017033393) Last point in range of
   generated curve
(dx     =   1.0000000000000E-4) Interval between generated
   points
(npts   =                  3837) Number of points to generate
(curve_g=                   yes) Generate a curve between
   specified limits
(make_im=                   yes) Create IRAF spectral image
(tbl_siz=                  5000) Maximum space to allocate for
    table
(interp_=                  line) By (line|curve|legen|cheby|
   spline3|spline1)
(mode   =                    al)
#USAGE
sinterp tbl_file="tdspec-0765-52254-0019.txt" input="STDIN"
   image="yspec-0765-52254-0019.fits" order=1 x1=3.5804 x2
   =3.9640 dx=1.E-4 npts=3837 curve_g=yes make_im=yes
   interp_mode="linear"
```

```
20 ...
21 ...
22 sinterp tbl_file="tdspec-7416-56810-0975.txt" input="STDIN"
      image="yspec-7416-56810-0975.fits" order=1 x1=3.5804 x2
      =3.9640 dx=1.E-4 npts=3837 curve_g=yes make_im=yes
      interp_mode="linear"
```

Listing 4: Editing the images' headers.

```
1 #DC-FLAG
2 hedit images="yspec-0765-52254-0019.fits[1]" fields="DC-FLAG"
      =1 add=yes verify=no show=no update=yes
3 ...
4 ...
5 #WFITTYPE
6 hedit images="yspec-0765-52254-0019.fits[1]" fields="WFITTYPE
      " value="LOG-LINEAR" add=yes verify=no show=no update=yes
7 ...
8 ...
9 #BUNIT
10 hedit images="yspec-0765-52254-0019.fits[1]" fields="BUNIT"
      value=1E-17erg/cm^2/s/Ang add=yes verify=no show=no update
      =yes
11 ...
12 ...
```

Listing 5: Correcting the spectra for interstellar absorption.

```
1 deredden 0874-52338-0125.fits 0874-52338-0125dd.fits 0.023
      type=A R=2.875
2 ...
3 ...
4 deredden 6617-56365-0896.fits 6617-56365-0896dd.fits 0.056
      type=A R=3.111
```

Listing 6: Doppler correction.

```
1 dopcor 0874-52338-0125dd.fits 0874-52338-0125dddd.fits
      1.285767
2 ...
3 ...
4 dopcor 6617-56365-0896dd.fits 6617-56365-0896dddd.fits
      1.151289
```

Listing 7: Syntax of the script used for the calculation of the various d_L.

```
./redshift 0.7003859 >> distanze
...
...
./redshift 0.3730658 >> distanze
```

Listing 8: Syntax of the script used to build the artificial spectra containing only the narrow emission lines.

```
function 0873-52674-0154r.fits 0873-52674-0154narrows.tab
   0873-52674-0154narrows.fits
...
...
function 7419-56811-0620r.fits 7419-56811-0620narrows.tab
   7419-56811-0620narrows.fits
```

Python

Listing 9: BCES Python code.

```
SELECT
#!/usr/bin/env python
# -*- coding: utf-8 -*-

"""
Various␣linear␣regression␣techniques

"""
import pylab
import numpy

def bces(x1, x2, x1err=[], x2err=[], cerr=[], logify=True,
   model='yx', \
         bootstrap=5000, verbose='normal', full_output=True):
    """
␣␣␣␣Bivariate,␣Correlated␣Errors␣and␣intrinsic␣Scatter␣(BCES)
␣␣␣␣translated␣from␣the␣FORTRAN␣code␣by␣Christina␣Bird␣and␣
   Matthew␣Bershady
␣␣␣␣(Akritas␣&␣Bershady,␣1996)

␣␣␣␣Linear␣regression␣in␣the␣presence␣of␣heteroscedastic␣
   errors␣on␣both
```

```
    variables and intrinsic scatter

    Parameters
    ----------
    x1          : array of floats
                  Independent variable, or observable
    x2          : array of floats
                  Dependent variable
    x1err       : array of floats (optional)
                  Uncertainties on the independent variable
    x2err       : array of floats (optional)
                  Uncertainties on the dependent variable
    cerr        : array of floats (optional)
                  Covariances of the uncertainties in the
                  dependent and
                  independent variables
    logify      : bool (default True)
                  Whether to take the log of the measurements
                  in order to
                  estimate the best-fit power law instead of
                  linear relation
    model       : {'yx', 'xy', 'bi', 'orth'}
                  BCES model with which to calculate
                  regression. See Notes
                  below for details.
    bootstrap   : False or int (default 5000)
                  get the errors from bootstrap resampling
                  instead of the
                  analytical prescription? if bootstrap is an
                  int, it is the
                  number of bootstrap resamplings
    verbose     : str (default 'normal')
                  Verbose level. Options are {'quiet', '
                  normal', 'debug'}
    full_output : bool (default True)
                  If True, return also the covariance between
                  the
                  normalization and slope of the regression.

    Returns
    -------
    a           : tuple of length 2
```

```
␣␣␣␣␣␣␣␣␣␣␣␣␣␣␣␣␣␣␣␣Best-fit␣normalization␣and␣its␣uncertainty␣(a,␣da)
␣␣␣␣␣␣b␣␣␣␣␣␣␣␣␣␣:␣tuple␣of␣length␣2
␣␣␣␣␣␣␣␣␣␣␣␣␣␣␣␣␣␣␣␣Best-fit␣slope␣and␣its␣uncertainty␣(b,␣db)

␣␣␣␣Optional␣outputs
␣␣␣␣----------------
␣␣␣␣␣␣cov_ab␣␣␣␣␣:␣2x2␣array␣of␣floats
␣␣␣␣␣␣␣␣␣␣␣␣␣␣␣␣␣␣␣␣covariance␣between␣a␣and␣b.␣Returned␣if␣full_output␣is␣set␣to
␣␣␣␣␣␣␣␣␣␣␣␣␣␣␣␣␣␣␣␣True.

␣␣␣␣Notes
␣␣␣␣-----
␣␣␣␣␣␣If␣verbose␣is␣normal␣or␣debug,␣the␣results␣from␣all␣the␣BCES␣models␣will
␣␣␣␣␣␣be␣printed␣(still,␣only␣the␣one␣selected␣in␣*model*␣will␣be␣returned).

␣␣␣␣␣␣the␣*model*␣parameter:
␣␣␣␣␣␣␣␣-'yx'␣stands␣for␣BCES(Y|X)
␣␣␣␣␣␣␣␣-'xy'␣stands␣for␣BCES(X|Y)
␣␣␣␣␣␣␣␣-'bi'␣stands␣for␣BCES␣Bisector
␣␣␣␣␣␣␣␣-'orth'␣stands␣for␣BCES␣Orthogonal

␣␣␣␣"""

    def _bess_bootstrap(npts, x1, x2, x1err, x2err, cerr,nsim):
        ##added by Gerrit, July 2014
        ##Unfortunately I needed a copy of the _bess function for bootstrapping.
        #Would be nicer if those two could be combined
        """
␣␣␣␣␣␣␣␣Do␣the␣entire␣regression␣calculation␣for␣4␣slopes:
␣␣␣␣␣␣␣␣OLS(Y|X),␣OLS(X|Y),␣bisector,␣orthogonal
␣␣␣␣␣␣␣␣"""
        #calculate sigma's for datapoints using length of confidence intervals
        sig11var = np.sum(x1err ** 2,axis=1,keepdims=True) / npts
        sig22var = np.sum(x2err ** 2,axis=1,keepdims=True) /
```

```
            npts
88          sig12var = np.sum(cerr,axis=1,keepdims=True) / npts
89
90          # calculate means and variances
91          x1av = np.mean(x1,axis=1,keepdims=True)
92          x1var = x1.var(axis=1,keepdims=True)
93          x2av = np.mean(x2,axis=1,keepdims=True)
94          x2var = x2.var(axis=1,keepdims=True)
95          covar_x1x2 = np.mean((x1-np.mean(x1,axis=1,keepdims=
               True)) * \
96                               (x2-np.mean(x2,axis=1,keepdims=
                                  True)),
97                               axis=1,keepdims=True)
98
99          # compute the regression slopes for OLS(X2|X1), OLS(
               X1|X2),
100         # bisector and orthogonal
101         if model == 'yx':
102             modelint = 1
103         else:
104             modelint = 4
105         b = np.zeros((modelint,nsim))
106         b[0] = ((covar_x1x2 - sig12var) / (x1var - sig11var))
               .flatten()
107         if model != 'yx':
108             b[1] = ((x2var - sig22var) / (covar_x1x2 -
                   sig12var)).flatten()
109             b[2] = ((b[0] * b[1] - 1 + np.sqrt((1 + b[0] **
                   2) * \
110                      (1 + b[1] ** 2))) / (b[0] + b[1])).flatten
                           ()
111             b[3] = 0.5 * ((b[1] - 1 / b[0]) + np.sign(
                   covar_x1x2).flatten()* \
112                      np.sqrt(4 + (b[1] - 1 / b[0]) ** 2))
113
114         # compute intercepts for above 4 cases:
115         a = x2av.flatten() - b * x1av.flatten()
116
117         # set up variables to calculate standard deviations
               of slope and
118         # intercept
119         xi = []
```

```
120         xi.append(((x1 - x1av) * (x2 - b[0].reshape(nsim,1) *
                x1 - \
121                                   a[0].reshape(nsim,1)) + \
122                     b[0].reshape(nsim,1) * x1err ** 2) / \
123                    (x1var - sig11var))
124         if model != 'yx':
125             xi.append(((x2 - x2av) * (x2 - b[1].reshape(nsim
                    ,1) * x1 - \
126                                         a[1].reshape(nsim,1)) +
                                             x2err ** 2) / \
127                        covar_x1x2)
128             xi.append((xi[0] * (1 + b[1].reshape(nsim,1) **
                    2) + \
129                        xi[1] * (1 + b[0].reshape(nsim,1) **
                           2)) / \
130                        ((b[0].reshape(nsim,1) + \
131                         b[1].reshape(nsim,1)) * \
132                         np.sqrt((1 + b[0].reshape(nsim,1) **
                            2) * \
133                                 (1 + b[1].reshape(nsim,1) **
                                    2))))
134             xi.append((xi[0] / b[0].reshape(nsim,1) ** 2 + xi
                    [1]) * \
135                        b[3].reshape(nsim,1) / \
136                        np.sqrt(4 + (b[1].reshape(nsim,1) - \
137                                1 / b[0].reshape(nsim,1)) ** 2)
                                   )
138         zeta = []
139         for i in xrange(modelint):
140             zeta.append(x2 - b[i].reshape(nsim,1) * x1 - x1av
                    * xi[i])
141
142         # calculate  variance for all a and b
143         bvar = np.zeros((4,nsim))
144         avar = np.zeros((4,nsim))
145         for i in xrange(modelint):
146             bvar[i] = xi[i].var(axis=1,keepdims=False)/ npts
147             avar[i] = zeta[i].var(axis=1,keepdims=False) /
                    npts
148         return a, b, avar, bvar, xi, zeta
149
150     def _bess(npts, x1, x2, x1err, x2err, cerr):
```

```
151         """
152 ␣␣␣␣␣␣␣␣Do␣the␣entire␣regression␣calculation␣for␣4␣slopes:
153 ␣␣␣␣␣␣␣␣␣␣OLS(Y|X),␣OLS(X|Y),␣bisector,␣orthogonal
154 ␣␣␣␣␣␣␣␣"""
155         # calculate sigma's for datapoints using length of
              confidence
156         # intervals
157         sig11var = sum(x1err ** 2) / npts
158         sig22var = sum(x2err ** 2) / npts
159         sig12var = sum(cerr) / npts
160         # calculate means and variances
161         x1av = numpy.average(x1)
162         x1var = numpy.std(x1) ** 2
163         x2av = numpy.average(x2)
164         x2var = numpy.std(x2) ** 2
165         covar_x1x2 = sum((x1 - x1av) * (x2 - x2av)) / npts
166         # compute the regression slopes for OLS(X2|X1), OLS(
              X1|X2),
167         # bisector and orthogonal
168         b = numpy.zeros(4)
169         b[0] = (covar_x1x2 - sig12var) / (x1var - sig11var)
170         b[1] = (x2var - sig22var) / (covar_x1x2 - sig12var)
171         b[2] = (b[0] * b[1] - 1 + numpy.sqrt((1 + b[0] ** 2)
              * \
172                 (1 + b[1] ** 2))) / (b[0] + b[1])
173         b[3] = 0.5 * ((b[1] - 1 / b[0]) + numpy.sign(
              covar_x1x2) * \
174                 numpy.sqrt(4 + (b[1] - 1 / b[0]) ** 2))
175         # compute intercepts for above 4 cases:
176         a = x2av - b * x1av
177         # set up variables to calculate standard deviations
              of slope
178         # and intercept
179         xi = []
180         xi.append(((x1 - x1av) * \
181                    (x2 - b[0] * x1 - a[0]) + b[0] * x1err **
                       2) / \
182                   (x1var - sig11var))
183         xi.append(((x2 - x2av) * (x2 - b[1] * x1 - a[1]) +
              x2err ** 2) / \
184                   covar_x1x2)
185         xi.append((xi[0] * (1 + b[1] ** 2) + xi[1] * (1 + b
```

```
            [0] ** 2)) / \
186                 ((b[0] + b[1]) * \
187                  numpy.sqrt((1 + b[0] ** 2) * (1 + b[1] **
                        2))))
188         xi.append((xi[0] / b[0] ** 2 + xi[1]) * b[3] / \
189                   numpy.sqrt(4 + (b[1] - 1 / b[0]) ** 2))
190         zeta = []
191         for i in xrange(4):
192             zeta.append(x2 - b[i]*x1 - x1av*xi[i])
193         # calculate  variance for all a and b
194         bvar = numpy.zeros(4)
195         avar = numpy.zeros(4)
196         for i in xrange(4):
197             bvar[i] = numpy.std(xi[i]) ** 2 / npts
198             avar[i] = numpy.std(zeta[i]) ** 2 / npts
199         return a, b, avar, bvar, xi, zeta
200
201     def _bootspbec(npts, x, y, xerr, yerr, cerr):
202         """
203 ␣␣␣␣␣␣␣␣Bootstrap␣samples
204 ␣␣␣␣␣␣␣␣"""
205         j = numpy.random.randint(npts, size = npts)
206         xboot = x[j]
207         xerrboot = xerr[j]
208         yboot = y[j]
209         yerrboot = yerr[j]
210         cerrboot = cerr[j]
211         return xboot, yboot, xerrboot, yerrboot, cerrboot
212
213     # ----  Main routine starts here  ---- #
214     # convert to numpy arrays just in case
215     x1 = numpy.array(x1)
216     x2 = numpy.array(x2)
217     x1err = numpy.array(x1err)
218     x2err = numpy.array(x2err)
219     if logify:
220         x1, x2, x1err, x2err = to_log(x1, x2, x1err, x2err)
221     cerr = numpy.array(cerr)
222     models = [['yx', 'xy', 'bi', 'orth'],
223               ['BCES(Y|X)', 'BCES(X|Y)', 'BCES␣Bisector', '
                     BCES␣Orthogonal']]
224     # which to return?
```

```
225     j = models[0].index(model)
226     npts = len(x1)
227     # are the errors defined?
228     if len(x1err) == 0:
229         x1err = numpy.zeros(npts)
230     if len(x2err) == 0:
231         x2err = numpy.zeros(npts)
232     if len(cerr) == 0:
233         cerr = numpy.zeros(npts)
234     if verbose == 'debug':
235         print 'x1 =', x1
236         print 'x1err =', x1err
237         print 'x2 =', x2
238         print 'x2err =', x2err
239         print 'cerr =', cerr
240         print '\n ** Returning values for', models[1][j], '**
                '
241         if bootstrap is not False:
242             print '     with errors from %d bootstrap
                    resamplings' %bootstrap
243         print ''
244 
245     # calculate nominal fits
246     bessresults = _bess(npts, x1, x2, x1err, x2err, cerr)
247     (a, b, avar, bvar, xi, zeta) = bessresults
248     # covariance between normalization and slope
249     if full_output:
250         covar_ab = numpy.cov(xi[j], zeta[j])
251 
252     if bootstrap is not False:
253         # make bootstrap simulated datasets, and compute
                averages and
254         # standard deviations of regression coefficients
255         asum = numpy.zeros(4)
256         assum = numpy.zeros(4)
257         bsum = numpy.zeros(4)
258         bssum = numpy.zeros(4)
259         sda = numpy.zeros(4)
260         sdb = numpy.zeros(4)
261         for i in xrange(bootstrap):
262             samples = _bootspbec(npts, x1, x2, x1err, x2err,
                    cerr)
```

```
263             (x1sim, x2sim, x1errsim, x2errsim, cerrsim) =
                    samples
264             besssim = _bess(npts, x1sim, x2sim, x1errsim,
                    x2errsim, cerrsim)
265             (asim, bsim, avarsim, bvarsim, xi, zeta) =
                    besssim
266             asum += asim
267             assum += asim ** 2
268             bsum += bsim
269             bssum += bsim ** 2
270
271         aavg = asum / bootstrap
272         bavg = bsum / bootstrap
273         for i in range(4):
274             sdtest = assum[i] - bootstrap * aavg[i] ** 2
275             if sdtest > 0:
276                 sda[i] = numpy.sqrt(sdtest / (bootstrap - 1))
277             sdtest = bssum[i] - bootstrap * bavg[i] ** 2
278             if sdtest > 0:
279                 sdb[i] = numpy.sqrt(sdtest / (bootstrap - 1))
280
281     if verbose in ('normal', 'debug'):
282         print '%s␣␣␣B␣␣␣␣␣␣␣␣␣␣err(B)' %('Fit'.ljust(19)),
283         print '␣␣␣␣␣␣␣␣␣␣A␣␣␣␣␣␣␣␣␣␣err(A)'
284         for i in range(4):
285             print '%s␣␣%9.2e␣+/-␣%8.2e␣␣␣␣%10.3e␣+/-␣%9.3e' \
286                   %(models[1][i].ljust(16), b[i],
287                     numpy.sqrt(bvar[i]), a[i], numpy.sqrt(
                            avar[i]))
288             if bootstrap is not False:
289                 print '%s␣␣%9.2e␣+/-␣%8.2e␣␣␣␣%10.3e␣+/-␣%9.3
                        e' \
290                       %('bootstrap'.ljust(16), bavg[i],
291                         sdb[i], aavg[i], sda[i])
292             print ''
293         if verbose == 'debug':
294             print 'cov[%s]␣=' %models[model]
295             print covar_ab
296
297     if bootstrap is not False:
298         if full_output:
299           return (a[j], sda[j]), (b[j], sdb[j]), covar_ab
```

```
300         else:
301           return (a[j], sda[j]), (b[j], sdb[j])
302     if full_output:
303         out = ((a[j], numpy.sqrt(avar[j])),
304                (b[j], numpy.sqrt(bvar[j])),
305                covar_ab)
306     else:
307         out = ((a[j], numpy.sqrt(avar[j])),
308                (b[j], numpy.sqrt(bvar[j])))
309     return out
310
311 def scatter(slope, zero, x1, x2, x1err=[], x2err=[]):
312     """
313 ␣␣␣␣Used␣mainly␣to␣measure␣scatter␣for␣the␣BCES␣best-fit
314
315 ␣␣␣␣"""
316     n = len(x1)
317     x2pred = zero + slope * x1
318     s = sum((x2 - x2pred) ** 2) / (n - 1)
319     if len(x2err) == n:
320         s_obs = sum((x2err / x2) ** 2) / n
321         s0 = s - s_obs
322     print numpy.sqrt(s), numpy.sqrt(s_obs), numpy.sqrt(s0)
323     return numpy.sqrt(s0)
324
325 def kelly(x1, x2, x1err=[], x2err=[], cerr=[], logify=True,
326           miniter=5000, maxiter=1e5, metro=True,
327           silent=True):
328     """
329 ␣␣␣␣Python␣wrapper␣for␣the␣linear␣regression␣MCMC␣of␣Kelly␣
    (2007).
330 ␣␣␣␣Requires␣pidly␣(http://astronomy.sussex.ac.uk/~anthonys/
    pidly/)␣and
331 ␣␣␣␣an␣IDL␣license.
332
333 ␣␣␣␣Parameters
334 ␣␣␣␣----------
335 ␣␣␣␣␣␣x1␣␣␣␣␣␣␣␣:␣array␣of␣floats
336 ␣␣␣␣␣␣␣␣␣␣␣␣␣␣␣␣␣␣Independent␣variable,␣or␣observable
337 ␣␣␣␣␣␣x2␣␣␣␣␣␣␣␣:␣array␣of␣floats
338 ␣␣␣␣␣␣␣␣␣␣␣␣␣␣␣␣␣␣Dependent␣variable
339 ␣␣␣␣␣␣x1err␣␣␣␣␣:␣array␣of␣floats␣(optional)
```

```
340 ␣␣␣␣␣␣␣␣␣␣␣␣␣␣␣␣␣␣Uncertainties␣on␣the␣independent␣variable
341 ␣␣␣␣␣␣x2err␣␣␣␣␣:␣array␣of␣floats␣(optional)
342 ␣␣␣␣␣␣␣␣␣␣␣␣␣␣␣␣␣␣Uncertainties␣on␣the␣dependent␣variable
343 ␣␣␣␣␣␣cerr␣␣␣␣␣␣:␣array␣of␣floats␣(optional)
344 ␣␣␣␣␣␣␣␣␣␣␣␣␣␣␣␣␣␣Covariances␣of␣the␣uncertainties␣in␣the␣
       dependent␣and
345 ␣␣␣␣␣␣␣␣␣␣␣␣␣␣␣␣␣␣independent␣variables
346 ␣␣␣␣"""
347     import pidly
348     n = len(x1)
349     if len(x2) != n:
350         raise ValueError('x1␣and␣x2␣must␣have␣same␣length')
351     if len(x1err) == 0:
352         x1err = numpy.zeros(n)
353     if len(x2err) == 0:
354         x2err = numpy.zeros(n)
355     if logify:
356         x1, x2, x1err, x2err = to_log(x1, x2, x1err, x2err)
357     idl = pidly.IDL()
358     idl('x1␣=␣%s' %list(x1))
359     idl('x2␣=␣%s' %list(x2))
360     cmd = 'linmix_err,␣x1,␣x2,␣fit'
361     if len(x1err) == n:
362         idl('x1err␣=␣%s' %list(x1err))
363         cmd += ',␣xsig=x1err'
364     if len(x2err) == n:
365         idl('x2err␣=␣%s' %list(x2err))
366         cmd += ',␣ysig=x2err'
367     if len(cerr) == n:
368         idl('cerr␣=␣%s' %list(cerr))
369         cmd += ',␣xycov=cerr'
370     cmd += ',␣miniter=%d,␣maxiter=%d' %(miniter, maxiter)
371     if metro:
372         cmd += ',␣/metro'
373     if silent:
374         cmd += ',␣/silent'
375     idl(cmd)
376     alpha = idl.ev('fit.alpha')
377     beta = idl.ev('fit.beta')
378     sigma = numpy.sqrt(idl.ev('fit.sigsqr'))
379     return alpha, beta, sigma
380
```

```
381 def mcmc(x1, x2, x1err=[], x2err=[], po=(1,1,0.5), logify=
        True,
382           nsteps=5000, nwalkers=100, nburn=500, output='full')
                 :
383     """
384 ␣␣␣␣Use␣emcee␣to␣find␣the␣best-fit␣linear␣relation␣or␣power␣
        law
385 ␣␣␣␣accounting␣for␣measurement␣uncertainties␣and␣intrinsic␣
        scatter
386
387 ␣␣␣␣Parameters
388 ␣␣␣␣----------
389 ␣␣␣␣␣␣␣x1␣␣␣␣␣␣␣␣␣:␣array␣of␣floats
390 ␣␣␣␣␣␣␣␣␣␣␣␣␣␣␣␣␣␣␣␣Independent␣variable,␣or␣observable
391 ␣␣␣␣␣␣␣x2␣␣␣␣␣␣␣␣␣:␣array␣of␣floats
392 ␣␣␣␣␣␣␣␣␣␣␣␣␣␣␣␣␣␣␣␣Dependent␣variable
393 ␣␣␣␣␣␣␣x1err␣␣␣␣␣␣:␣array␣of␣floats␣(optional)
394 ␣␣␣␣␣␣␣␣␣␣␣␣␣␣␣␣␣␣␣␣Uncertainties␣on␣the␣independent␣variable
395 ␣␣␣␣␣␣␣x2err␣␣␣␣␣␣:␣array␣of␣floats␣(optional)
396 ␣␣␣␣␣␣␣␣␣␣␣␣␣␣␣␣␣␣␣␣Uncertainties␣on␣the␣dependent␣variable
397 ␣␣␣␣␣␣␣po␣␣␣␣␣␣␣␣␣:␣tuple␣of␣3␣floats␣(optional)
398 ␣␣␣␣␣␣␣␣␣␣␣␣␣␣␣␣␣␣␣␣Initial␣guesses␣for␣zero␣point,␣slope,␣and␣
        intrinsic
399 ␣␣␣␣␣␣␣␣␣␣␣␣␣␣␣␣␣␣␣␣scatter.␣Results␣are␣not␣very␣sensitive␣to␣
        these␣values
400 ␣␣␣␣␣␣␣␣␣␣␣␣␣␣␣␣␣␣␣␣so␣they␣shouldn't␣matter␣a␣lot.
401 ␣␣␣␣␣␣␣logify␣␣␣␣␣:␣bool␣(default␣True)
402 ␣␣␣␣␣␣␣␣␣␣␣␣␣␣␣␣␣␣␣␣Whether␣to␣take␣the␣log␣of␣the␣measurements
        ␣in␣order␣to
403 ␣␣␣␣␣␣␣␣␣␣␣␣␣␣␣␣␣␣␣␣estimate␣the␣best-fit␣power␣law␣instead␣of␣
        linear␣relation
404 ␣␣␣␣␣␣␣nsteps␣␣␣␣␣:␣int␣(default␣5000)
405 ␣␣␣␣␣␣␣␣␣␣␣␣␣␣␣␣␣␣␣␣Number␣of␣steps␣each␣walker␣should␣take␣in␣
        the␣MCMC
406 ␣␣␣␣␣␣␣nwalkers␣␣␣:␣int␣(default␣100)
407 ␣␣␣␣␣␣␣␣␣␣␣␣␣␣␣␣␣␣␣␣Number␣of␣MCMC␣walkers
408 ␣␣␣␣␣␣␣nburn␣␣␣␣␣␣:␣int␣(default␣500)
409 ␣␣␣␣␣␣␣␣␣␣␣␣␣␣␣␣␣␣␣␣Number␣of␣samples␣to␣discard␣to␣give␣the␣
        MCMC␣enough␣time
410 ␣␣␣␣␣␣␣␣␣␣␣␣␣␣␣␣␣␣␣␣to␣converge.
411 ␣␣␣␣␣␣␣output␣␣␣␣␣:␣list␣of␣ints␣or␣'full'␣(default␣'full')
412 ␣␣␣␣␣␣␣␣␣␣␣␣␣␣␣␣␣␣␣␣If␣'full',␣then␣return␣the␣full␣samples␣(
```

```
    except␣for␣burn-in
␣␣␣␣␣␣␣␣␣␣␣␣␣␣␣␣␣␣␣␣section)␣for␣each␣parameter.␣Otherwise,␣
    each␣float
␣␣␣␣␣␣␣␣␣␣␣␣␣␣␣␣␣␣␣␣corresponds␣to␣a␣percentile␣that␣will␣be␣
    returned␣for
␣␣␣␣␣␣␣␣␣␣␣␣␣␣␣␣␣␣␣␣each␣parameter.

␣␣␣␣Returns
␣␣␣␣-------
␣␣␣␣␣␣See␣*output*␣argument␣above␣for␣return␣options.

␣␣␣␣"""
    import emcee
    if len(x1err) == 0:
        x1err = numpy.ones(len(x1))
    if len(x2err) == 0:
        x2err = numpy.ones(len(x1))
    def lnlike(theta, x, y, xerr, yerr):
        a, b, s = theta
        model = a + b*x
        sigma = numpy.sqrt((b*xerr)**2 + yerr*2 + s**2)
        lglk = 2 * sum(numpy.log(sigma)) + \
               sum(((y-model) / sigma) ** 2) + \
               numpy.log(len(x)) * numpy.sqrt(2*numpy.pi) / 2
        return -lglk
    def lnprior(theta):
        a, b, s = theta
        if s >= 0:
            return 0
        return -numpy.inf
    def lnprob(theta, x, y, xerr, yerr):
        lp = lnprior(theta)
        return lp + lnlike(theta, x, y, xerr, yerr)
    if logify:
        x1, x2, x1err, x2err = to_log(x1, x2, x1err, x2err)
    start = numpy.array(po)
    ndim = len(start)
    pos = [start + 1e-4*numpy.random.randn(ndim) for i in
       range(nwalkers)]
    sampler = emcee.EnsembleSampler(nwalkers, ndim, lnprob,
                                    args=(x1,x2,x1err,x2err))
    sampler.run_mcmc(pos, nsteps)
```

```
451     samples = numpy.array([sampler.chain[:,nburn:,i].reshape
            (-1) \
452                            for i in xrange(ndim)])
453     if logify:
454         samples[2] *= numpy.log(10)
455     if output == 'full':
456         return samples
457     else:
458         try:
459             values = [[numpy.percentile(s, o) for o in output
                    ]
460                       for s in samples]
461             return values
462         except TypeError:
463             msg = 'ERROR: wrong value for argument output in
                    mcmc().'
464             msg += ' Must be "full" or list of ints.'
465             print msg
466             exit()
467     return
468
469 def mle(x1, x2, x1err=[], x2err=[], cerr=[], s_int=True,
470         po=(1,0,0.1), verbose=False, logify=True, full_output
                =False):
471     """
472 ____Maximum Likelihood Estimation of best-fit parameters
473
474 ____Parameters
475 ____----------
476 _______x1, x2____: float arrays
477 ____________________the independent and dependent variables.
478 _______x1err, x2err : float arrays (optional)
479 ____________________measurement uncertainties on independent
        and dependent
480 ____________________variables. Any of the two, or both, can be
        supplied.
481 _______cerr_______: float array (same size as x1)
482 ____________________covariance on the measurement errors
483 _______s_int______: boolean (default True)
484 ____________________whether to include intrinsic scatter in the
        MLE.
485 _______po_________: tuple of floats
```

```
486 ␣␣␣␣␣␣␣␣␣␣␣␣␣␣␣␣␣␣␣␣initial␣guess␣for␣free␣parameters.␣If␣s_int
    ␣is␣True,␣then
487 ␣␣␣␣␣␣␣␣␣␣␣␣␣␣␣␣␣␣␣␣po␣must␣have␣3␣elements;␣otherwise␣it␣can␣
    have␣two␣(for␣the
488 ␣␣␣␣␣␣␣␣␣␣␣␣␣␣␣␣␣␣␣␣zero␣point␣and␣the␣slope)
489 ␣␣␣␣␣␣verbose␣␣␣␣:␣boolean␣(default␣False)
490 ␣␣␣␣␣␣␣␣␣␣␣␣␣␣␣␣␣␣␣␣verbose?
491 ␣␣␣␣␣␣logify␣␣␣␣␣:␣boolean␣(default␣True)
492 ␣␣␣␣␣␣␣␣␣␣␣␣␣␣␣␣␣␣␣␣whether␣to␣convert␣the␣values␣to␣log10's.␣
    This␣is␣to
493 ␣␣␣␣␣␣␣␣␣␣␣␣␣␣␣␣␣␣␣␣calculate␣the␣best-fit␣power␣law.␣Note␣that
    ␣the␣result␣is
494 ␣␣␣␣␣␣␣␣␣␣␣␣␣␣␣␣␣␣␣␣given␣for␣the␣equation␣log(y)=a+b*log(x)␣--
    ␣i.e.,␣the
495 ␣␣␣␣␣␣␣␣␣␣␣␣␣␣␣␣␣␣␣␣zero␣point␣must␣be␣converted␣to␣10**a␣if␣
    logify=True
496 ␣␣␣␣␣␣full_output␣:␣boolean␣(default␣False)
497 ␣␣␣␣␣␣␣␣␣␣␣␣␣␣␣␣␣␣␣␣numpy.optimize.fmin's␣full_output␣argument
498
499 ␣␣␣␣Returns
500 ␣␣␣␣-------
501 ␣␣␣␣␣␣a␣␣␣␣␣␣␣␣␣␣:␣float
502 ␣␣␣␣␣␣␣␣␣␣␣␣␣␣␣␣␣␣␣␣Maximum␣Likelihood␣Estimate␣of␣the␣zero␣
    point.␣Note␣that
503 ␣␣␣␣␣␣␣␣␣␣␣␣␣␣␣␣␣␣␣␣if␣logify=True,␣the␣power-law␣intercept␣is␣
    10**a
504 ␣␣␣␣␣␣b␣␣␣␣␣␣␣␣␣␣:␣float
505 ␣␣␣␣␣␣␣␣␣␣␣␣␣␣␣␣␣␣␣␣Maximum␣Likelihood␣Estimate␣of␣the␣slope
506 ␣␣␣␣␣␣s␣␣␣␣␣␣␣␣␣␣:␣float␣(optional,␣if␣s_int=True)
507 ␣␣␣␣␣␣␣␣␣␣␣␣␣␣␣␣␣␣␣␣Maximum␣Likelihood␣Estimate␣of␣the␣
    intrinsic␣scatter
508
509 ␣␣␣␣"""
510     from scipy import optimize
511     n = len(x1)
512     if len(x2) != n:
513         raise ValueError('x1␣and␣x2␣must␣have␣same␣length')
514     if len(x1err) == 0:
515         x1err = numpy.ones(n)
516     if len(x2err) == 0:
517         x2err = numpy.ones(n)
518     if logify:
```

```
519         x1, x2, x1err, x2err = to_log(x1, x2, x1err, x2err)
520
521     f = lambda a, b: a + b * x1
522     if s_int:
523         w = lambda b, s: numpy.sqrt(b**2 * x1err**2 + x2err
               **2 + s**2)
524         loglike = lambda p: 2 * sum(numpy.log(w(p[1],p[2])))
               + \
525                             sum(((x2 - f(p[0],p[1])) / w(p
                                [1],p[2])) ** 2) + \
526                             numpy.log(n * numpy.sqrt(2*numpy.
                                pi)) / 2
527     else:
528         w = lambda b: numpy.sqrt(b**2 * x1err**2 + x2err**2)
529         loglike = lambda p: sum(numpy.log(w(p[1]))) + \
530                             sum(((x2 - f(p[0],p[1])) / w(p
                                [1])) ** 2) / 2 + \
531                             numpy.log(n * numpy.sqrt(2*numpy.
                                pi)) / 2
532         po = po[:2]
533     out = optimize.fmin(loglike, po, disp=verbose,
           full_output=full_output)
534     return out
535
536 def to_log(x1, x2, x1err, x2err):
537     """
538 ␣␣␣␣Take␣linear␣measurements␣and␣uncertainties␣and␣transform␣
       to␣log␣values.
539
540 ␣␣␣␣"""
541     logx1 = numpy.log10(numpy.array(x1))
542     logx2 = numpy.log10(numpy.array(x2))
543     x1err = numpy.log10(numpy.array(x1)+numpy.array(x1err)) -
           logx1
544     x2err = numpy.log10(numpy.array(x2)+numpy.array(x2err)) -
           logx2
545     return logx1, logx2, x1err, x2err
```

Listing 10: Cross-Matching of NVSS+ROSAT versus SDSS

```
1 # -*- coding: utf-8 -*-
2 import pandas as pd
3 import lnr
```

```
import numpy as np
input = pd.read_csv('dati.txt', header=None, dtype='float' ,
    skiprows=1, delim_whitespace=True)
input = input.convert_objects(convert_numeric=True)
data = np.array(input)
lnr.bces(data[:,[6]], data[:,[4]], data[:,[7]], data[:,[5]],
    logify=False, model='bi', bootstrap=500000, verbose='
    normal', full_output=True)
```

SQL codes

Listing 11: Cross-Matching of NVSS+ROSAT versus SDSS

```
SELECT
s.class, s.subclass, s.ra, s.decl,
nr.NVSS, nr."1RXS", s.SpecObjID
FROM SpecObj AS s, MyDB.NVSSandROSAT  AS nr
WHERE s.SpecObjid=
dbo.fGetNearestSpecObjIdEq(nr.n_RAJ2000, nr.n_DEJ2000, 0.05)
```

Listing 12: Cross-Matching between BZ4CAT and SDSS

```
SELECT
s.class, s.subclass, s.SpecObjID, s.Plate, s.MJD,
s.FiberID, s.ra as raSDSS, s.decl as decSDSS, bz4.*
FROM SpecObj AS s, MyDB.bzcat4 AS bz4
WHERE s.SpecObjid=
dbo.fGetNearestSpecObjIdEq(bz4._RAJ2000,bz4._DEJ2000,0.05)
```

Listing 13: Sample's average S/N ratio computation

```
SELECT avg(s.snMedian)
FROM specobj AS s, mydb.new_HbMgII AS hb,
     mydb.new_MgII AS m, mydb.new_MgIICIV AS c
WHERE s.specobjid=hb.specobjid or
      s.specobjid=m.specobjid  or
      s.specobjid=c.specobjid
```

Listing 14: Sample's ordering based on the values of z

```
SELECT *
FROM mydb.sample
order by z
```

Listing 15: Computation of monochromatic and bolometric luminosities for λ5100 and λ3000, as well as their related errors.

```
SELECT
  CASE WHEN n.bz4 <>'NESSUNO' THEN 1
  ELSE 0
  END AS blazar,
  dbo.fIAUFromEq(n.ra, n.dec) AS SDSS,
  n.bz4, n.plate, n.mjd, n.fiberid,
  n.z, n."Distance(Mpc)",
  33.077910594 + 2 * log10(n."Distance(Mpc)") +
  log10(5100) + log10(n.flux_5100) AS L_5100,
  power( 10 * log(n.flux_5100) , -1 ) * n.rms_5100 AS eL5100,
  33.077910594 + 2 * log10(n."Distance(Mpc)") +
  log10(3000) + log10(n.flux_3000) AS L_3000,
  power( 10 * log(n.flux_3000) , -1 ) * n.rms_3000 AS eL3000,
  log10(8.1) +
  33.077910594 + 2 * log10(n."Distance(Mpc)") +
  log10(5100) + log10(n.flux_5100)
        AS LBOL5100,
  sqrt(
    power(  power( 10 * log(8.1) , -1  )        * 0.4 , 2 ) +
    power(  power( 10 * log(n.flux_5100) , -1 ) * n.rms_5100
       , 2 )
       ) AS eLBOL5100,
  log10(5.2) +
  33.077910594 + 2 * log10(n."Distance(Mpc)") +
  log10(3000) + log10(n.flux_3000)
        AS LBOL3000,
  sqrt(
    power( power( 10 * log(5.2) , -1 )         * 0.2 , 2 ) +
    power( power( 10 * log(n.flux_3000) , -1 ) * n.rms_3000 ,
        2 )
       ) AS eLBOL3000
FROM specobj AS s, mydb.new_HbMgII AS n
WHERE n.plate = s.plate and n.mjd = s.mjd and n.fiberid = s.
   fiberid
ORDER by blazar desc, n.plate, n.mjd, n.fiberid
```

Listing 16: Computation of the radio flux density.

```
SELECT
( f.a * ( 3 + log10(5/(1+t.z)) ) + f.b        -- flux at 5GHz
    with nu_observed=5GHz/(1+z), nu in MHz
   - 3  -23 )                                  -- mJy ---> Jy
      ---> erg/cm^2 s Hz
from TESI_HbMgII AS t, FIRST_new_HbMgII AS f
```

Listing 17: Radio-loudness computation.

```
( f.a * ( 3 + log10(5/(1+t.z)) ) + f.b        -- flux at 5GHz
    using SPECFIND 2.0, with \nu based on the redshift value:
    nu_observed=5GHz/(1+z), \nu in MHz units
- 3  -23 )                                    -- mJy --->  Jy
    ---> erg/cm^2 s Hz
-
( -17 +  log10( f.flux_2500 * power( 1.76 , -0.5 )  )
                -- SDSS normalization 10^-17 & f_4400 =
   f_2500 * (4400/2500)^alpha
+ log10(3.34)  - 19  + 2 * log10(4400) )
                              -- erg/cm^2 s A ---> erg/cm^2 s
    Hz   (3.34 * 10^-19 * lambda^2)
AS RL4400
from TESI_HbMgII AS t, FIRST_new_HbMgII AS f
```

Listing 18: Computation of the jet powers.

```
( 17 +                                        -- to add to the
   33.078 which contains the 10^-17 due to SDSS normalization
  33.078 + 2 * log10(t.d_L) +                 -- 4 * pi *
     luminosity distance
  ( - i.a - 1 ) * log10( 1 + t.z ) +          -- K-correction N.B
     . SPECFIND uses S=nu^(alpha) and not S=nu^(-alpha) => -
     i.a
  9 + log10(1.4)                              -- nu_0 ( GHz --->
     Hz )
  + log10(f.Fint)                             -- flux at 1.4GHz
  - 3 - 23                                    -- mJy --->  Jy
     ---> erg/cm^2 s^-1 Hz^-1
  - 40  )                                     -- P_1.4 in 10^40
     erg/s  units
  * 0.75                                      -- slope
  + 1.91                                      -- intercept
```

```
10    + 42                                          -- P_jet in 10^42
        erg/s units
11    from indexes_HbMgII i, TESI_HbMgII t, FIRST_new_HbMgII f
12  where i.plate=t.plate and i.mjd=t.mjd and i.fiberid=t.fiberid
13  and f.plate=t.plate and f.mjd=t.mjd and f.fiberid=t.fiberid
```

Listing 19: Computation of the jet powers errors.

```
1  select
2  t.plate, t.mjd, t.fiberid,
3  ROUND(jet_power,2),
4  ROUND(sqrt(
5  power(log10(f.Fint),2) * power(0.14,2) +
6  power(0.75,2) * power( power( log(10) * f.Fint,-1) * f.Rms ,
       2 ) +
7  power(0.18 , 2 )
8                ),2)
9  from mydb.TESI_MgIICIV t, mydb.FIRST_new_MgIICIV f
10 where
11 t.plate=f.plate and t.mjd=f.mjd and t.fiberid=f.fiberid
```

BIBLIOGRAPHY

Akritas M.G. and Bershady M.A. (1996). "Linear Regression for Astronomical Data with Measurement Errors and Intrinsic Scatter". *ApJ*, 470:706.
URL http://adsabs.harvard.edu/abs/1996ApJ...470..706A. 60

Alam S., Albareti F.D., Prieto C.A., Anders F., Anderson S.F., Anderton T., Andrews B.H., Armengaud E., Éric Aubourg, Bailey S., et al (2015). "The Eleventh and Twelfth Data Releases of the Sloan Digital Sky Survey: Final Data from SDSS-III". *The Astrophysical Journal Supplement Series*, 219(1):12.
URL http://stacks.iop.org/0067-0049/219/i=1/a=12. 39, 40

Antonucci R. (1993). "Unified models for active galactic nuclei and quasars". *ARA&A*, 31:473–521. 12

Atwood W.B., Abdo A.A., Ackermann M., Althouse W., Anderson B., Axelsson M., Baldini L., Ballet J., Band D.L., Barbiellini G., et al (2009). "The Large Area Telescope on the Fermi Gamma-Ray Space Telescope Mission". *The Astrophysical Journal*, 697(2):1071.
URL http://iopscience.iop.org/0004-637X/697/2/1071. 39

Baade W. and Minkowski R. (1954). "Identification of the Radio Sources in Cassiopeia, Cygnus A, and Puppis A.". *ApJ*, 119:206.
URL http://adsabs.harvard.edu/abs/1954ApJ...119..206B. 5

Baskin A. and Laor A. (2005). "What controls the CIV line profile in active galactic nuclei?". *MNRAS*, 356:1029–1044.
URL http://adsabs.harvard.edu/abs/2005MNRAS.356.1029B. 62

Becker R.H., White R.L. and Helfand D.J. (1995). "The FIRST Survey: Faint Images of the Radio Sky at Twenty Centimeters". *ApJ*, 450:559. 39

Beckmann V. and Shrader C. (2012). *"AGN Types and Unification"*, pages 89–140. Wiley-VCH Verlag GmbH & Co. KGaA.
URL http://dx.doi.org/10.1002/9783527666829.ch4. 14

Bentz M.C., Peterson B.M., Netzer H., Pogge R.W. and Vestergaard M. (2009). "The Radius-Luminosity Relationship for Active Galactic Nuclei: The Effect of Host-Galaxy Starlight on Luminosity Measurements. II. The Full Sample of Reverberation-Mapped AGNs". *ApJ*, 697:160–181.
URL http://adsabs.harvard.edu/abs/2009ApJ...697..160B. 62

Biretta J.A., Stern C.P. and Harris D.E. (1991). "The radio to X-ray spectrum of the M87 jet and nucleus". *AJ*, 101:1632–1646.
URL http://adsabs.harvard.edu/abs/1991AJ....101.1632B.

Bîrzan L., McNamara B.R., Nulsen P.E.J., Carilli C.L. and Wise M.W. (2008). "Radiative Efficiency and Content of Extragalactic Radio Sources: Toward a Universal Scaling Relation between Jet Power and Radio Power". *ApJ*, 686:859–880.
URL http://adsabs.harvard.edu/abs/2008ApJ...686..859B. 76

Blandford R.D. (1989). "Accretion Disk Magnetohydrodynamics and the Origin of Jets". In Meyer F., editor, *NATO Advanced Science Institutes (ASI) Series C*, volume 290 of *NATO Advanced Science Institutes (ASI) Series C*, page 35.
URL http://adsabs.harvard.edu/abs/1989ASIC..290...35B. 18

Blandford R.D. and McKee C.F. (1982). "Reverberation mapping of the emission line regions of Seyfert galaxies and quasars". *ApJ*, 255:419–439.
URL http://adsabs.harvard.edu/abs/1982ApJ...255..419B. 62

Blandford R.D. and Payne D.G. (1982). "Hydromagnetic flows from accretion discs and the production of radio jets". *MNRAS*, 199:883–903.
URL http://adsabs.harvard.edu/abs/1982MNRAS.199..883B. 24

Blandford R.D. and Znajek R.L. (1977). "Electromagnetic extraction of energy from Kerr black holes". *MNRAS*, 179:433–456.
URL http://adsabs.harvard.edu/abs/1977MNRAS.179..433B. 2, 24

Bolton C.T. (1972). "Identification of Cygnus X-1 with HDE 226868". *Nature*, 235:271–273.
URL http://adsabs.harvard.edu/abs/1972Natur.235..271B. 7

Bolton J.G. and Stanley G.J. (1948). "Variable Source of Radio Frequency Radiation in the Constellation of Cygnus". *Nature*, 161:312–313.
URL http://adsabs.harvard.edu/abs/1948Natur.161..312B. 5

Bondi H. (1952). "On spherically symmetrical accretion". *MNRAS*, 112:195.
URL http://adsabs.harvard.edu/abs/1952MNRAS.112..195B. 19

Cavagnolo K.W., McNamara B.R., Nulsen P.E.J., Carilli C.L., Jones C. and Bîrzan L. (2010). "A Relationship Between AGN Jet Power and Radio Power". *ApJ*, 720:1066–1072.
URL http://adsabs.harvard.edu/abs/2010ApJ...720.1066C. 76

Chase R.C. and van Speybroeck L.P. (1973). "Wolter-Schwarzschild telescopes for X-ray astronomy.". *Appl. Opt.*, 12:1042–1044.
URL http://adsabs.harvard.edu/abs/1973ApOpt..12.1042C. 42

Clavel J., Reichert G.A., Alloin D., Crenshaw D.M., Kriss G., Krolik J.H., Malkan M.A., Netzer H., Peterson B.M., Wamsteker W., et al (1991). "Steps toward determination of the size and structure of the broad-line region in active galactic nuclei. I - an 8 month campaign of monitoring NGC 5548 with IUE". *ApJ*, 366:64–81.
URL http://adsabs.harvard.edu/abs/1991ApJ...366...64C. 62

Condon J.J., Cotton W.D., Greisen E.W., Yin Q.F., Perley R.A., Taylor G.B. and Broderick J.J. (1998a). "The NRAO VLA Sky Survey". *The Astronomical Journal*, 115(5):1693.
URL http://stacks.iop.org/1538-3881/115/i=5/a=1693. 39

Condon J.J., Cotton W.D., Greisen E.W., Yin Q.F., Perley R.A., Taylor G.B. and Broderick J.J. (1998b). "The NRAO VLA Sky Survey". *AJ*, 115:1693–1716.
URL http://adsabs.harvard.edu/abs/1998AJ....115.1693C. 47

Dawson K.S., Schlegel D.J., Ahn C.P., Anderson S.F., Aubourg E., Bailey S., Barkhouser R.H., Bautista J.E., Beifiori A., Berlind A.A., et al (2013). "The Baryon Oscillation Spectroscopic Survey of SDSS-III". *AJ*, 145:10.
URL http://adsabs.harvard.edu/abs/2013AJ....145...10D. 40

Edge D.O., Shakeshaft J.R., McAdam W.B., Baldwin J.E. and Archer S. (1959). "A survey of radio sources at a frequency of 159 Mc/s". *MmRAS*, 68:37–60.
URL http://adsabs.harvard.edu/abs/1959MmRAS..68...37E. 5

Einstein A. (1916). "Die Grundlage der allgemeinen Relativitätstheorie". *Annalen der Physik*, 354(7):769–822.
URL http://dx.doi.org/10.1002/andp.19163540702. 7

Eisenstein D.J., Weinberg D.H., Agol E., Aihara H., Allende Prieto C., Anderson S.F., Arns J.A., Aubourg E., Bailey S., Balbinot E., et al (2011). "SDSS-III:

Massive Spectroscopic Surveys of the Distant Universe, the Milky Way, and Extra-Solar Planetary Systems". *AJ*, 142:72.
URL http://adsabs.harvard.edu/abs/2011AJ....142...72E.

Fath E.A. (1909). "the spectra of some spiral nebulae and globular star clusters". *Lick Observatory Bulletin*, 5:71–77.
URL http://adsabs.harvard.edu/abs/1909LicOB...5...71F. 3

Ford H., Tsvetanov Z., Hartig G., Kriss G., Harms R. and Dressel L. (1996). "HST FOS/COSTAR Small Aperture Spectroscopy of the Disk of Ionized Gas in M87". In Benvenuti P., Macchetto F.D. and Schreier E.J., editors, *Science with the Hubble Space Telescope - II*, page 192.
URL http://adsabs.harvard.edu/abs/1996swhs.conf..192F. 7

Fossati G., Maraschi L., Celotti A., Comastri A. and Ghisellini G. (1998). "A unifying view of the spectral energy distributions of blazars". *MNRAS*, 299:433–448.
URL http://adsabs.harvard.edu/abs/1998MNRAS.299..433F. 37

George I.M. and Fabian A.C. (1991). "X-ray reflection from cold matter in active galactic nuclei and X-ray binaries". *MNRAS*, 249:352–367.
URL http://adsabs.harvard.edu/abs/1991MNRAS.249..352G. 19

Ghisellini G., Haardt F., Ciardi B., Sbarrato T., Gallo E., Tavecchio F. and Celotti A. (2015). "CMB quenching of high-redshift radio-loud AGNs". *MNRAS*, 452:3457–3469.
URL http://adsabs.harvard.edu/abs/2015MNRAS.452.3457G. 74

Ghisellini G., Haardt F. and Matt G. (2004). "Aborted jets and the X-ray emission of radio-quiet AGNs". *A&A*, 413:535–545.
URL http://adsabs.harvard.edu/abs/2004A%26A...413..535G. 11

Ghisellini G., Padovani P., Celotti A. and Maraschi L. (1993). "Relativistic bulk motion in active galactic nuclei". *ApJ*, 407:65–82.
URL http://adsabs.harvard.edu/abs/1993ApJ...407...65G. 34

Ginzburg V.L. (1989). *"Applications of electrodynamics in theoretical physics and astrophysics."*.
URL http://adsabs.harvard.edu/abs/1989aetp.book.....G. 28

Greenstein J.L. and Schmidt M. (1964). "The Quasi-Stellar Radio Sources 3c 48 and 3c 273". *ApJ*, 140:1.
URL http://adsabs.harvard.edu/abs/1964ApJ...140....1G. 5

Guilbert P.W. and Rees M.J. (1988). "'Cold' material in non-thermal sources". *MNRAS*, 233:475–484.
URL http://adsabs.harvard.edu/abs/1988MNRAS.233..475G. 11

Gunn J.E., Siegmund W.A., Mannery E.J., Owen R.E., Hull C.L., Leger R.F., Carey L.N., Knapp G.R., York D.G., Boroski W.N., et al (2006). "The 2.5 m Telescope of the Sloan Digital Sky Survey". *AJ*, 131:2332–2359.
URL http://adsabs.harvard.edu/abs/2006AJ....131.2332G. 40

Hazard C., Mackey M.B. and Shimmins A.J. (1963). "Investigation of the Radio Source 3C 273 By The Method of Lunar Occultations". *Nature*, 197:1037–1039.
URL http://adsabs.harvard.edu/abs/1963Natur.197.1037H. 5

Helfand D.J., White R.L. and Becker R.H. (2015). "The Last of FIRST: The Final Catalog and Source Identifications". *The Astrophysical Journal*, 801(1):26.
URL http://stacks.iop.org/0004-637X/801/i=1/a=26. 47

Henri G. and Petrucci P.O. (1997). "Anisotropic illumination of AGN's accretion disk by a non thermal source. I. General theory and application to the Newtonian geometry". *A&A*, 326:87–98.
URL http://adsabs.harvard.edu/abs/1997A%26A...326...87H. 11

Hey J.S., Parsons S.J. and Phillips J.W. (1946). "Fluctuations in Cosmic Radiation at Radio-Frequencies". *Nature*, 158:234.
URL http://adsabs.harvard.edu/abs/1946Natur.158..234H. 5

Holt S.S., Neff S.G. and Urry C.M., editors (1992). *"Testing the AGN paradigm; Proceedings of the 2nd Annual Topical Astrophysics Conference, Univ. of Maryland, College Park, Oct. 14-16, 1991"*, volume 254 of *American Institute of Physics Conference Series*.
URL http://adsabs.harvard.edu/abs/1992AIPC..254.....H. 19

Hubble E. (1929). "A Relation between Distance and Radial Velocity among Extra-Galactic Nebulae". *Proceedings of the National Academy of Science*, 15:168–173.
URL http://adsabs.harvard.edu/abs/1929PNAS...15..168H.

Hubble E.P. (1926). "extragalactic nebulae". *ApJ*, 64:321–369.
URL http://adsabs.harvard.edu/abs/1926ApJ....64..321H. 4

Jansky K.G. (1933). "Electrical phenomena that apparently are of interstellar origin". *Popular Astronomy*, 41:548.
URL http://adsabs.harvard.edu/abs/1933PA.....41..548J. 4

Kaspi S., Brandt W.N., Maoz D., Netzer H., Schneider D.P. and Shemmer O. (2007). "Reverberation Mapping of High-Luminosity Quasars: First Results". *ApJ*, 659:997–1007.
URL `http://adsabs.harvard.edu/abs/2007ApJ...659..997K`. 62

Kaspi S., Maoz D., Netzer H., Peterson B.M., Vestergaard M. and Jannuzi B.T. (2005). "The Relationship between Luminosity and Broad-Line Region Size in Active Galactic Nuclei". *ApJ*, 629:61–71.
URL `http://adsabs.harvard.edu/abs/2005ApJ...629...61K`. 64

Kaspi S., Smith P.S., Netzer H., Maoz D., Jannuzi B.T. and Giveon U. (2000). "Reverberation Measurements for 17 Quasars and the Size-Mass-Luminosity Relations in Active Galactic Nuclei". *ApJ*, 533:631–649.
URL `http://adsabs.harvard.edu/abs/2000ApJ...533..631K`. 62

Kellermann K.I., Sramek R., Schmidt M., Shaffer D.B. and Green R. (1989). "VLA observations of objects in the Palomar Bright Quasar Survey". *AJ*, 98:1195–1207.
URL `http://adsabs.harvard.edu/abs/1989AJ.....98.1195K`. 74

Kerr R.P. (1963). "Gravitational Field of a Spinning Mass as an Example of Algebraically Special Metrics". *Phys. Rev. Lett.*, 11:237–238.
URL `http://link.aps.org/doi/10.1103/PhysRevLett.11.237`. 8

Lawrence A. and Elvis M. (1982). "Obscuration and the various kinds of Seyfert galaxies". *ApJ*, 256:410–426.
URL `http://adsabs.harvard.edu/abs/1982ApJ...256..410L`. 19

Lemaître G. (1927). "Un Univers homogène de masse constante et de rayon croissant rendant compte de la vitesse radiale des nébuleuses extra-galactiques". *Annales de la Société Scientifique de Bruxelles*, 47:49–59.
URL `http://adsabs.harvard.edu/abs/1927ASSB...47...49L`.

Lynden-Bell D. (1969). "Galactic Nuclei as Collapsed Old Quasars". *Nature*, 223:690–694.
URL `http://adsabs.harvard.edu/abs/1969Natur.223..690L`. 7

Lyutikov M. (2009). "Magnetocentrifugal launching of jets from discs around Kerr black holes". *Monthly Notices of the Royal Astronomical Society*, 396(3):1545–1552.
URL `http://dx.doi.org/10.1111/j.1365-2966.2009.14811.x`. 24

Maraschi L., Colpi M., Ghisellini G., Perego A. and Tavecchio F. (2012). "On the role of black hole spin and accretion in powering relativistic jets in AGN".

Journal of Physics Conference Series, 355(1):012016.
URL http://adsabs.harvard.edu/abs/2012JPhCS.355a2016M. 77

Marscher A.P. (1987). "Synchro-Compton emission from superluminal sources". In Zensus J.A. and Pearson T.J., editors, *Superluminal Radio Sources*, pages 280–300.
URL http://adsabs.harvard.edu/abs/1987slrs.work..280M. 30

Massaro E., Giommi P., Leto C., Marchegiani P., Maselli A., Perri M., Piranomonte S. and Sclavi S. (2009). "Roma-BZCAT: a multifrequency catalogue of blazars". *A&A*, 495(2):691–696.
URL http://dx.doi.org/10.1051/0004-6361:200810161. 46

McLure R.J. and Dunlop J.S. (2004). "The cosmological evolution of quasar black hole masses". *MNRAS*, 352:1390–1404.
URL http://adsabs.harvard.edu/abs/2004MNRAS.352.1390M. 62

Metzroth K.G., Onken C.A. and Peterson B.M. (2006). "The Mass of the Central Black Hole in the Seyfert Galaxy NGC 4151". *ApJ*, 647:901–909.
URL http://adsabs.harvard.edu/abs/2006ApJ...647..901M. 62

Minkowski H. (2007). "Source text 1908: Mechanics and the Relativity Postulate". In Renn J., Janssen M., Norton J.D., Sauer T., Stachel J., Divarci L., Schemmel M., Smeenk C. and Martin C., editors, *The Genesis of General Relativity*, page 273.
URL http://adsabs.harvard.edu/abs/2007ggr..conf..273M.

Narayan R. and Yi I. (1995). "Advection-dominated Accretion: Underfed Black Holes and Neutron Stars". *ApJ*, 452:710.
URL http://adsabs.harvard.edu/abs/1995ApJ...452..710N. 23

Nemmen R.S. and Brotherton M.S. (2010). "Quasar bolometric corrections: theoretical considerations". *MNRAS*, 408:1598–1605.
URL http://adsabs.harvard.edu/abs/2010MNRAS.408.1598N. 60

Nenkova M., Sirocky M.M., Željko Ivezić and Elitzur M. (2008). "AGN Dusty Tori. I. Handling of Clumpy Media". *The Astrophysical Journal*, 685(1):147.
URL http://stacks.iop.org/0004-637X/685/i=1/a=147. 13

Ochsenbein F., Bauer P. and Marcout J. (2000). "The VizieR database of astronomical catalogues". *A&AS*, 143:23–32.
URL http://adsabs.harvard.edu/abs/2000A%26AS..143...23O.

Peebles P.J.E. (1993). *"Principles of Physical Cosmology"*.
URL http://adsabs.harvard.edu/abs/1993ppc..book.....P. 58

Peterson B.M. (1993). "Reverberation mapping of active galactic nuclei". *PASP*, 105:247–268.
URL http://adsabs.harvard.edu/abs/1993PASP..105..247P. 62

Peterson B.M. (1997). *"An Introduction to Active Galactic Nuclei"*.
URL http://adsabs.harvard.edu/abs/1997iagn.book.....P. 3

Reber G. (1944). "Cosmic Static.". *ApJ*, 100:279.
URL http://adsabs.harvard.edu/abs/1944ApJ...100..279R. 4

Runnoe J.C., Brotherton M.S. and Shang Z. (2012). "Updating quasar bolometric luminosity corrections". *MNRAS*, 422:478–493.
URL http://adsabs.harvard.edu/abs/2012MNRAS.422..478R. 60

Rybicki G.B. and Lightman A.P. (1986). *"Radiative Processes in Astrophysics"*.
URL http://adsabs.harvard.edu/abs/1986rpa..book.....R. 26

Sandage A., Véron P. and Wyndham J.D. (1965). "Optical Identification of New Quasi-Stellar Radio Sources". *ApJ*, 142:1307–1311.
URL http://adsabs.harvard.edu/abs/1965ApJ...142.1307S. 6

Schmidt M. (1963). "3C 273 : A Star-Like Object with Large Red-Shift". *Nature*, 197:1040.
URL http://adsabs.harvard.edu/abs/1963Natur.197.1040S. 5

Schwarzschild K. (1916). "On the Gravitational Field of a Mass Point According to Einstein's Theory". *Abh. Konigl. Preuss. Akad. Wissenschaften Jahre 1906,92, Berlin,1907*, 1916:189–196.
URL http://esoads.eso.org/abs/1916AbhKP1916..189S. 8

Scott R.L. (1986). "Hypersensitizing Kodak emulsions, Type IIIa-F and 103a-E.". *AAS Photo Bulletin*, 42:8–10.
URL http://adsabs.harvard.edu/abs/1986AASPB..42....8S. 44

Seyfert C.K. (1943). "Nuclear Emission in Spiral Nebulae". *ApJ*, 97:28.
URL http://adsabs.harvard.edu/abs/1943ApJ....97...28S. 4

Shakura N.I. and Sunyaev R.A. (1973). "Black holes in binary systems. Observational appearance.". *A&A*, 24:337–355.
URL http://adsabs.harvard.edu/abs/1973A%26A....24..337S. 21

Shapiro S.L., Lightman A.P. and Eardley D.M. (1976). "A two-temperature accretion disk model for Cygnus X-1 - Structure and spectrum". *ApJ*, 204:187–199.
URL `http://adsabs.harvard.edu/abs/1976ApJ...204..187S`.

Sikora M., Stawarz Ł. and Lasota J.P. (2008). "Radio-loudness of active galaxies and the black hole evolution". *New A Rev.*, 51:891–897.
URL `http://adsabs.harvard.edu/abs/2008NewAR..51..891S`. 75, 76

Silva L., Granato G.L., Bressan A. and Danese L. (1998). "Modeling the Effects of Dust on Galactic Spectral Energy Distributions from the Ultraviolet to the Millimeter Band". *ApJ*, 509:103–117.
URL `http://adsabs.harvard.edu/abs/1998ApJ...509..103S`. 2

Slipher V.M. (1917). "the spectrum and velocity of the nebula n.g.c. 1068 (m 77)". *Lowell Observatory Bulletin*, 3:59–62.
URL `http://adsabs.harvard.edu/abs/1917LowOB...3...59S`. 4

Stawarz L., Sikora M. and Lasota J.P. (2008). "Radio Loudness of AGNs: Host Galaxy Morphology and the Spin Paradigm". In Rector T.A. and De Young D.S., editors, *Extragalactic Jets: Theory and Observation from Radio to Gamma Ray*, volume 386 of *Astronomical Society of the Pacific Conference Series*, page 169.
URL `http://adsabs.harvard.edu/abs/2008ASPC..386..169S`. 3

Sun W.H. and Malkan M.A. (1989). "Fitting improved accretion disk models to the multiwavelength continua of quasars and active galactic nuclei". *ApJ*, 346:68–100.
URL `http://adsabs.harvard.edu/abs/1989ApJ...346...68S`. 22

Trakhtenbrot B. and Netzer H. (2012). "Black hole growth to z = 2 - I. Improved virial methods for measuring M_{BH} and L/L_{Edd}". *MNRAS*, 427:3081–3102.
URL `http://adsabs.harvard.edu/abs/2012MNRAS.427.3081T`. 64, 66, 70, 80, 85

Truemper J. (1982). "The ROSAT mission". *Advances in Space Research*, 2:241–249.
URL `http://adsabs.harvard.edu/abs/1982AdSpR...2..241T`. 39

Venturi T., Readhead A.C.S., Marr J.M. and Backer D.C. (1993). "Subparsec-scale radio structure in NGC 1275 - Complex structure in the vicinity of the central engine". *ApJ*, 411:552–564.
URL `http://adsabs.harvard.edu/abs/1993ApJ...411..552V`. 17

Voges W., Aschenbach B., Boller T., Brauninger H., Briel U., Burkert W., Dennerl K., Englhauser J., Gruber R., Haberl F., et al (2000). "Vizier Online Data

Catalog: ROSAT All-Sky Survey Faint Source Catalog (Voges+ 2000)". *VizieR Online Data Catalog*, 9029:0.
URL http://adsabs.harvard.edu/abs/2000yCat.9029....0V. 47

Vollmer B., Gassmann B., Derrière S., Boch T., Louys M., Bonnarel F., Dubois P., Genova F. and Ochsenbein F. (2010). "The SPECFIND V2.0 catalogue of radio cross-identifications and spectra. SPECFIND meets the Virtual Observatory". *A&A*, 511:A53.
URL http://adsabs.harvard.edu/abs/2010A%26A...511A..53V. 74

Webster B.L. and Murdin P. (1972). "Cygnus X-1-a Spectroscopic Binary with a Heavy Companion ?". *Nature*, 235:37–38.
URL http://adsabs.harvard.edu/abs/1972Natur.235...37W. 7

Yanny B., Rockosi C., Newberg H.J., Knapp G.R., Adelman-McCarthy J.K., Alcorn B., Allam S., Allende Prieto C., An D., Anderson K.S.J., et al (2009). "SEGUE: A Spectroscopic Survey of 240,000 Stars with g = 14-20". *AJ*, 137:4377–4399.
URL http://adsabs.harvard.edu/abs/2009AJ....137.4377Y. 40

York D.G., Adelman J., Anderson, Jr. J.E., Anderson S.F., Annis J., Bahcall N.A., Bakken J.A., Barkhouser R., Bastian S., Berman E., et al (2000). "The Sloan Digital Sky Survey: Technical Summary". *AJ*, 120:1579–1587.
URL http://adsabs.harvard.edu/abs/2000AJ....120.1579Y.

Yusef-Zadeh F. and Morris M. (1988). "The northern extension of the radio arc near the Galactic center". *ApJ*, 329:729–738.
URL http://adsabs.harvard.edu/abs/1988ApJ...329..729Y. 25

Zasowski G., Johnson J.A., Frinchaboy P.M., Majewski S.R., Nidever D.L., Rocha Pinto H.J., Girardi L., Andrews B., Chojnowski S.D., Cudworth K.M., et al (2013). "Target Selection for the Apache Point Observatory Galactic Evolution Experiment (APOGEE)". *AJ*, 146:81.
URL http://adsabs.harvard.edu/abs/2013AJ....146...81Z.

ACKNOWLEDGEMENTS (ITALIAN)

"In caso di ritardo in arrivo dei treni Frecciarossa, Frecciargento e Frecciabianca, compreso tra i 30 e i 59 minuti, Trenitalia ti riconosce un bonus pari al 25% del prezzo del biglietto che potrà essere utilizzato entro 12 mesi per l'acquisto di un nuovo biglietto." Mà e pà: ora potete rivendere il carnét. Quindi, in primis e classicamente, si ringrazia lo sponsor principale, anche per tutto il tempo speso credendoci pure nei momenti in cui non lo stavo facendo io stesso. Vi voglio bene, ma proprio tanto.

Ringrazio anche gli zii tutti la cui stima da parte mia è aumentata esponenzialmente dal momento in cui hanno smesso di chiedermi "E con l'università come va?": grazie per essere stati omertosamente italiani dentro, ho sempre sospettato di avere radici calabresi.

Care anche alle nonne, avete tenuto duro abbastanza per essere qui. Ed ora, solo per voi, uno stress test. Rispondete alla seguente domanda: che giorno è oggi?

Ciao cuginetti! Sono contento che siate venuti a farvi un giro: questa è la compagnia di sbandati che frequento. Ora si spiegano molte cose, no?

Ovviamente i ringraziamenti vanno anche al Professor Rafanelli che mi ha permesso di intraprendere quest'avventura, nonché a Giovanni (alias "*like as*" e "*costant*": noi sappiamo) a cui devo molto, inclusa la promessa di prendere lezioni di inglese, dopo quelle di italiano ovviamente.

Un grazie speciale nella versione ufficiale va ad Ema che mi ha indicato pionierisitcamente la via ed incoraggiato sempre: tu però sai cosa vuol dire dare struttura, quindi è sempre stato un appoggio che va oltre al "dai studia"...

Un bacio enorme va a Simona, compagna che mi ha sostenuto in mille modi durante ques'ultimo anno e mezzo, e che ultimamente è ancora più fantastica.

Un saluto va agli amici tutti, sono contento che ci siate!

Ovviamente avrò avuto delle dimenticanze, comunque se qualcuno dovesse rivendicare un'assenza mi dica pure che a casa ho il backup, quindi al limite editiamo

il file e lo rimandiamo in stampa!

Siamo a 140 pagine, in copisteria si staranno già leccando i baffi, meglio chiudere qui.